UC Irvine
UC Irvine Electronic Theses and Dissertations

Title
Broadband Impedance Match to Monolayer Graphene in the Terahertz Domain

Permalink
https://escholarship.org/uc/item/54s6w2pr

Author
Pham, Phi

Publication Date
2018

Peer reviewed|Thesis/dissertation

UNIVERSITY OF CALIFORNIA,
IRVINE

Broadband Impedance Match to Monolayer Graphene in the Terahertz Domain

DISSERTATION

submitted in partial satisfaction of the requirements
for the degree of

DOCTOR OF PHILOSOPHY

in Material Science and Engineering

by

Phi Huy Quoc Pham

Dissertation Committee:
Professor Peter Burke, Chair
Associate Professor Regina Ragan
Associate Professor Alon Gorodetsky

2018

DEDICATION

To

Ông Bà Nội, Ông Bà Ngoại, my family, friends, and everyone along the way.

TABLE OF CONTENTS

LIST OF FIGURES

LIST OF TABLES

ACKNOWLEDGMENTS

I want to thank all my research mentors who helped paved the way for me to completing my Ph.D. Scott Bunch at the University of Colorado gave me the generous opportunity to work in his lab as a sophomore and this chance to conduct meaningful research continues to motivate me. Paul McEuen when I was at Cornell University was truly inspirational in his pursuit for knowledge, and his broad research interests is especially admirable. Arend van der Zande, Xinghui Liu, and Steven Koenig showed me first hand, how rewarding the graduate student life can be. I want to thank Peter Burke for allowing me to work in his lab. By permitting me pursue research under my own course pushed me to grow as a researcher and learner further than I thought was possible. Peter's approach to answering the questions he is interested in has shown me how the pursuit of knowledge can be a powerful lifelong experience.

The staff at the INRF provided resources that were crucial to my research and I could not have achieved my goals without Brittany Grey, Ryan Smith, Alana Valencia, Steven Martinez, Mo Kebaili, and Richard Chang. Jake Hes worked overtime to make sure my tools were up and running and our conversations about Kernville and the outdoors made the hours in the cleanroom pass by with ease. My collaborators deserve enormous praise and recognition especially Elliott Brown, and Weidong Zhang.

My lab mates in the Burke lab, including Ted Pham and Will Wang, provided immeasurable help, motivation, and often, a collective group to share complaints of grad life. Jinfeng Li taught me so much electronics and measurement. Weiwei Zhou was the best post doc a graduate student could learn from. My undergrads, especially Nhi Quach, devoted their free time to my project and deserve tremendous credit. My friends at UCI made life in Irvine a wonderful experience including late night pho runs, IM championships, camping in the desert, and adopting pet bunnies. I had extraordinary support from Chen Wang, from driving me to turn off the CVD furnace late at night, pushing me to get my papers written in a timely manner, and supporting me to pursue research in a way that helped my spirit flourish.

My family here in Southern California always accepted me to their families and provided a taste of home when I needed a break from grad school. My grandparents always motivate me to achieve the most I can in life and deserve praise and acknowledgement. Of course, I want to thank brother and sister, and especially my parents. They gave me the freedom to pursue my dreams, and always support me in my studies and ambitions.

Phi Huy Quoc Pham

2008 – 2011	Research Assistant, Scott Bunch Lab University of Colorado, Boulder
2009	Summer Research Assistant, Paul McEuen Lab Cornell University
2010	Summer Research Assistant, Rodney Ruoff Lab University of Texas, Austin
2011	B.A. in Physics University of Colorado, Boulder
2012 – 2018	Research Assistant, Peter Burke Lab University of California, Irvine
2013	M.S in Materials Science and Engineering University of California, Irvine
2018	Ph.D. in Materials Science and Engineering University of California, Irvine

ABSTRACT OF THE DISSERTATION

Broadband Impedance Match to Monolayer Graphene in the Terahertz Domain

By

Phi Huy Quoc Pham

Doctor of Philosophy in Material Science and Engineering

University of California, Irvine, 2018

Professor Peter J. Burke, Chair

The coupling of an electromagnetic plane wave to a thin conductor depends on the sheet conductance of the material. A poor conductor interacts weakly with the incoming light, allowing the majority of the radiation to pass. A good conductor does not absorb light and reflects the wave almost entirely. For suspended films, the transition from transmitter to reflector occurs when the sheet resistance is approximately the characteristic impedance of free-space ($Z_0 = 377\ \Omega$). Near this point, the interaction is maximized, and the conductor absorbs strongly. We show that monolayer graphene, a tunable conductor, can be electrically modified to reach this transition, thereby achieving the maximum absorptive coupling across a broad range of frequencies in terahertz (THz) band. This interaction with an electromagnetic wave, to be a transmitter or absorber, is based on tunable electronic properties (rather than geometric structure), and is realized by bottom-up engineering of large-area monolayer graphene devices.

Chemical vapor deposition is used to increase the graphene domain size and decrease grain boundaries. By using a fast two-step oxidized copper growth, individual graphene domains of 5-mm can be synthesized in less than 5-hours total growth duration.

Following CVD synthesis, graphene transfer is optimized by removing bubbles that adhere to the graphene surface, and are transferred onto substrates modified by self-assembled monolayers (SAM), leading to improvement of the device on/off ratio. The high mobility graphene devices fabricated demonstrate the largest transmittance depth-of-modulation of THz waves to date, and by impedance matching devices using chemical doping, near maximum absorption is achieved.

INTRODUCTION

Monolayer graphene was first isolated from bulk graphite in 2004[1]. Using mechanical exfoliation by a process called the "scotch-tape method", researchers were able to separate layers of bulk graphite by repeated peeling. This allows the multi-layer graphene to be thinned down, until only one monolayer exists, and subsequently, transferred onto a wafer for experiments. This form of graphene remains the "gold standard" in terms of quality, and lead to the preliminary studies that a legitimized graphene as a wonder material. Material characteristics such as 2.3% optical absorption[2], field-effect tunability with high carrier mobility[1], large conductivity[1], and record high young's modulus[3] are some of the breakthrough physical properties demonstrated from mechanically exfoliated samples. Although mechanical exfoliated graphene has proven to be the highest quality, the size scale of such samples remains limited (the scotch tape method seldom produced samples larger than 50-micron width). Hence, the desire to scale-up graphene has driven the development of large-area graphene synthesis methods.

Chemical vapor deposition (CVD) has showed to be one of the most promising methods to producing large-area graphene. CVD graphene growth on copper produces mostly monolayer graphene[4], and hence, allows the monolayer films sizes to be limited mainly by the size of the CVD furnace used. As early as 2010, Samsung demonstrated graphene films up to 30-inch diagonal[5]. Additionally, advances in single-crystal growth have further advanced the electronic quality of CVD grown graphene[6]. While CVD synthesis has made real progress in terms of large-area films and individual domain size, the quality of CVD grown graphene

remains inferior to that of mechanically exfoliated samples. This is due to the fact that CVD grown graphene requires transfer from the growth substrate in order to be used in graphene devices; this includes tunable graphene-terahertz modulators. Contamination and defects such as tears and wrinkles generated during transfer remain a challenge when transferring graphene[7], and improvements could lead to new high-performance graphene devices.

For this dissertation, the goal of fabricating a voltage-tunable graphene-THz device was approached using a "bottom-up" methodology. Specifically, the desirable properties of monolayer thickness, large-area, high mobility, and low sheet resistance was incorporated throughout the fabrication process; CVD graphene was optimized toward large domain sizes for high mobility and low sheet resistance, and chemical doping and substrate modification was used during transfer for impedance matching. By engineering our devices judiciously starting from a gaseous carbon feedstock, up to when a full graphene-THz device was fabricated, our approach successfully matches the impedance of a two-dimensional material to free-space across broadband frequencies in the terahertz range.

Chapter 1: Background

1.1 Graphene Structure

Monolayer graphene, is a honeycomb lattice of sp2 hybridized carbon atoms with a bong angle of 120, as shown in Fig. 1.1[8]. Because graphene is only one monolayer, the thickness is ~ 0.34 nm, with a bong length between neighboring carbon atoms ~ 0.142 nm. This bond length value lies between the carbon-carbon single bond (~ 0.147 nm) and carbon-carbon double bond (~0.135) length, and is a result of the sp2 hybridized structure of graphene. Three sp^2-hybridized orbitals oriented in the x-y plane form σ–bonds, while the unhybridized $2p_z$ orbital, perpendicular to the x-y plane, contribute to π–bonds[8,9]. Each carbon atom contributes one delocalized π electron, thus the π band is completely full, while the π∗ band is completely empty[8,9]. The two π bands meet at the Dirac point to form a region of linear dispersion, with massless Dirac fermion charge carriers traveling at the Fermi velocity $v_f \approx 10^6$ m/s[8,9]. Graphene is a zero-gap semiconductor, and for pristine, undoped graphene, the Fermi level is at the Dirac point, Fig. 1.1[8].
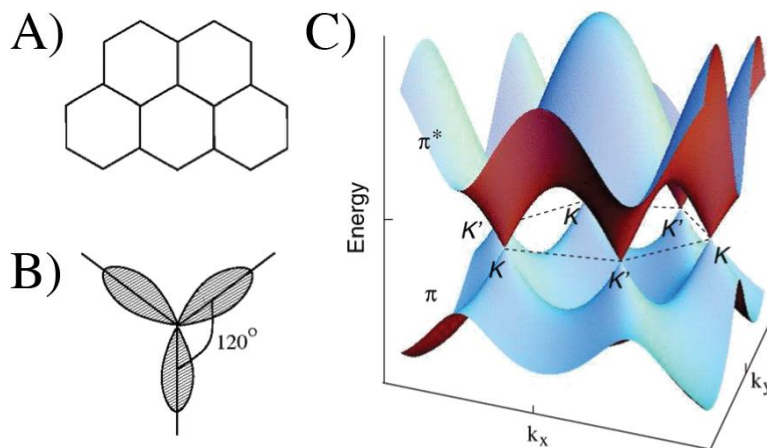
Figure 1.1: a) Honeycomb lattice structure of graphene b) sp2-hybridized orbitals with mutual 120 angles c) Band structure of graphene. At the K point, there is a zero-gap, linear dispersion[8].

The unique band structure of graphene explains some of the well-known properties such as the ambipolar electric field effect[1], optical transparency defined by the fine-structure constant[2], and room temperature quantum Hall effect[10]. Another unique aspect of high quality graphene is that the carrier mobility can be very large (> 100,000 cm^2/Vs) even at large carrier densities (10^{12} cm^{-2}). This enables graphene to have distinctive optoelectronic properties not found in metals or semiconductors.

1.2 Graphene AC Conductivity

The zero-gap band structure of graphene also leads to a non-trivial frequency-dependent AC conductance, which governs the absorption of incident electromagnetic (EM) radiation. Using the Kubo formula, we can arrive at the conductivity as[11–13],

$$\sigma(\omega) = \sigma_{inter}(\omega) + \sigma_{intra}(\omega)$$

$$= \frac{ie^2\omega}{\pi} \int_0^\infty \frac{f(\varepsilon - \varepsilon_F) - f(-\varepsilon - \varepsilon_F)}{(2\varepsilon)^2 - (\varepsilon + i\delta)^2} \, d\epsilon + \frac{ie^2\varepsilon_F}{\pi\hbar^2(\omega + \frac{i}{\tau_m})} \qquad (1)$$

Where e is electron charge, f(ε) is the Fermi-Dirac distribution, ε_F is the Fermi energy, $\hbar$ is the Planck constant, ω is the frequency, and δ is the broadening parameter. The two terms indicate the contribution of interband, and intraband transitions, respectively.

At optical frequencies the sheet conductance of graphene is dominated by interband transitions, and exhibits a universal value of $G_g = (\pi/4) \cdot G_0 = (e^2/4\hbar)$[14], where G_0 is the conductance quantum. This results in its low absorbance, approximated by the product of G_g and the characteristic impedance of free-space, $Z_0 = 377\,\Omega$. This product can be written $\pi \cdot (e^2/\hbar c) \equiv \pi \cdot \alpha$, where α is the fine

structure = 1/137. Thus, only ≈ 2.3% of the light is absorbed, and the majority of the light is transmitted.

In contrast, at frequencies lower than $\sim 2E_F/h$ (where E_F is the Fermi energy), as is the case in the THz range, the photon energy is too low to excite electron–hole pairs, and the electromagnetic sheet conductance is expected to follow the DC sheet conductance[13,15]. This should occur for frequencies up to $\sim 1/\tau$, where τ is the scattering time, at which point the conductance is expected to undergo a Drude-like roll-off[16–19], dropping towards the low optical value. The AC conductance can be adjusted by engineering E_F and τ according to the equations:

$$G_{DC} = \frac{e^2}{4\hbar} \frac{4}{\pi} \frac{E_F \tau}{\hbar}$$

(2)

$$G(\omega) = \frac{G_{DC}}{1 + i\omega\tau}$$

(3)

Hence, graphene could act as an atomically thin conductor to control EM waves in the mm wave and THz bands without the need for nanoscale patterning that is typically required in the optical regime. Experiments for terahertz modulators and broadband absorbers performed will be discussed as the main application in this dissertation, but in order to realize such devices, the synthesis and transfer of graphene samples must be optimized to produce high quality graphene.

1.3 Graphene Synthesis

A major breakthrough in graphene research was realized with the advent of using chemical vapor deposition to grow graphene[4]. Compared to using mechanical exfoliation where it is difficult to control the number of layers (with monolayer and

bilayer graphene being the most desirable), size and shape of graphene, and location of graphene, CVD graphene on copper foil results in mostly monolayer graphene films. Since the CVD process occurs in a furnace, the copper foil and quartz tube can increased to industrial size scales, and hence 30-inch monolayer graphene films can be easily grown, Fig. 1.2[5].
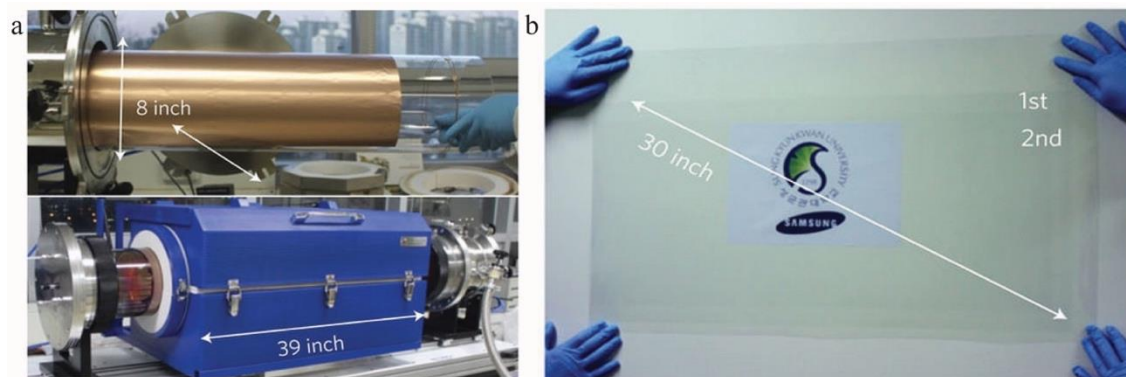
Figure 1.2: a) 8-inch diameter quart tube used for CVD graphene growth. b) 30-inch monolayer graphene films can be synthesized using CVD. Each additional layer increases the total optical absorbance[5].

Using various transfer techniques, the CVD grown graphene can be transferred to almost any substrate[5,7], and allows for lithographic patterning to fabricate arrays of devices in parallel[20,21].

There has been much attention towards increasing graphene domain size[22-25]. Initially, simple methods such as decreasing the concentration (partial pressure) of carbon precursor (methane), and tuning the $H_2:CH_4$ ratio during growth were used to decrease nucleation density, and increase the domain size[26,27]. Recently, it has been demonstrated that oxidized copper foils play an important role in controlling the nucleation density in order to promote graphene domain-size[22-24,28]. It has been shown, both by ex-situ and in-situ oxidation, that copper foils that are exposed to oxygen can essentially "turn off" graphene nucleation. By controlling the

amount of oxidation, researchers were able to grow large-area single-crystals (mm scale). Although large domain-size graphene can be synthesized using this method, thus far, the method requires long growth times (hours to days) in order to preserve a low nucleation density. Furthermore, while researchers have been successful in increasing domain sizes from μm up to mm, detrimental defects and contamination as result of transfer of the CVD grown graphene from the copper foil to target substrate hamper use of CVD graphene for large-area high quality device applications.

1.4 Graphene Transfer

The most widely used method to transfer graphene employs the use of a scaffold polymer[7,29–33]. Typically, graphene on copper foil is coated with a layer of polymer; the polymer layer adds support when the graphene is removed from the copper foil (by chemical etching or electrochemical delamination), as depicted in Fig. 1.3[34]. Usually, polymethylmethacrytlate (PMMA) is used because of its facile deposition and widespread use and availability in lithography[7,29]. Researchers have also experimented with a number of alternative polymers such as polydimethylsiloxane (PDMS), and poly (bisphenol A) carbonate (PC)[33,35,36]. Polymers can influence the graphene surface in different ways, and can provide varying levels of rigidity for transfer. For example, a thick layer of PDMS allows the graphene film to be fully removed from solution, and hence, provides a mean to "dry transfer".
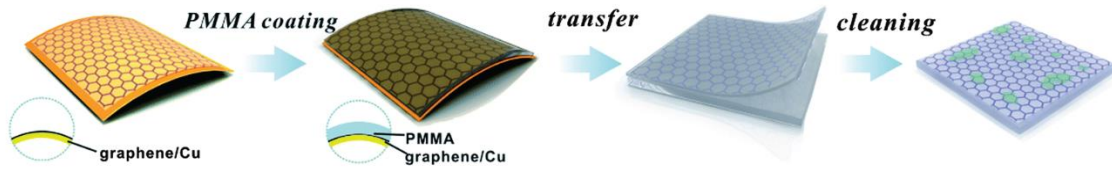
Figure 1.3: Standard Graphene Transfer. PMMA (or various polymer/metal support) is deposited on graphene. Graphene is then transferred to the target substrate. Finally, support layer is removed[34]**.**

Even with the use of a myriad of a polymers, the use of polymers in transfer usually induces unfavorable contamination such as doping and additional scattering[37]. Because of this fact, graphene researchers have explored completely polymer-free transfer[30,38–40]. Another issue resulting in degrading graphene quality during transfer arises from the formation of bubbles from the chemical etch and delamination solutions. Bubbles generated during graphene transfer adhere to the graphene surface, and consequently, are trapped between the target substrate and graphene film upon transfer. After drying, the trapped bubbles induce cracks, wrinkles, and tears in the graphene film which degrade the mobility and sheet resistance of transferred graphene films. Because of this issue, many researchers have intentionally avoided the generation of bubbles during graphene transfer, by means of low concentration etching solutions and low voltages during "bubble-free" electro-delamination[7,41]. Regardless of the employed transfer technique, the underlying concept remains the same. Transfer methods should minimize interaction with the graphene film to limit permanent changes to morphology or electrical quality of the CVD grown graphene.

1.5 Bottom-Up Graphene-Terahertz Devices

The end objective of this dissertation is to fabricate a high-quality graphene-THz optoelectronic device. In order to realize these devices, a bottom-up

methodology was employed with the intent of optimizing and preserving the high-quality properties of graphene. Specifically, desirable properties for a graphene-THz device include large-area films to accommodate the~ 3-mm diameter terahertz beam waist, high mobility for greater device sensitivity, and low sheet resistance for impedance matching. Starting with CVD graphene growth, we aim to increase individual domain-size of graphene films using copper oxidation to ensure that the synthesized graphene has high mobility and the scattering from grain boundaries is decreased. Following synthesis, the CVD graphene was transferred with a variety of techniques including substrate modification to decrease interface scattering, chemical doping to engineer large-area sheet resistance, and bubble-removal from the graphene surface to minimize tears and wrinkles of transferred films. By doing so, we fabricate graphene-THz devices that can easily tune the graphene sheet conductance so as to modulate the broadband transmittance of THz waves, Fig. 1.4.
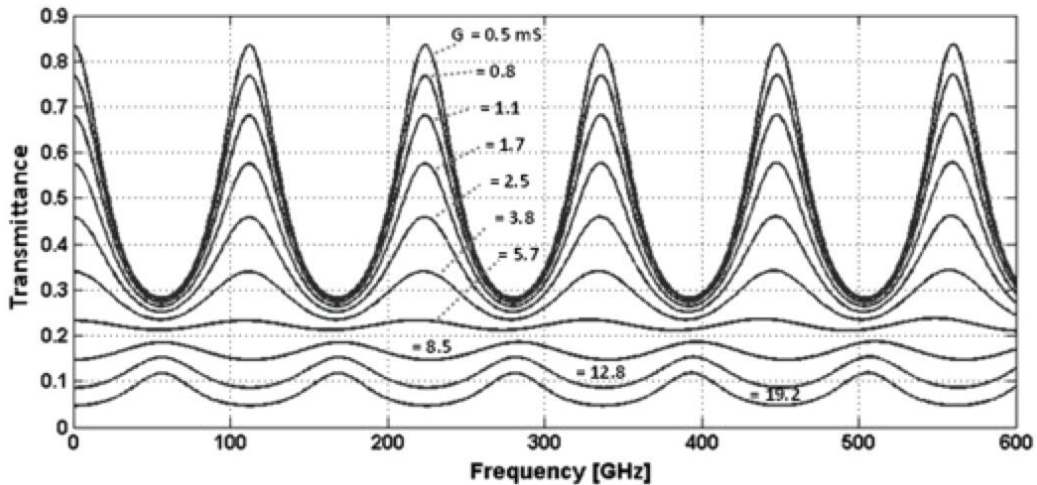
Figure 1.4: Transmittance vs Frequency for different sheet conductance ranging from 0.5 mS - 19.2 mS[42].

Our devices preserve the high mobility and allows the graphene sheet to span large ranges of sheet conductance (including the free-space impedance threshold),

thereby demonstrating the largest depth of modulation (DoM) and greatest absorption for a single-layer graphene device to date.

CHAPTER 2: Chemical Vapor Deposition of Graphene

2.1 CVD Graphene

We chose to pursue in-house CVD graphene for two main reasons; to provide large quantities of monolayer, polycrystalline graphene films, and to explore new, single-crystal recipes and procedures. By having the option to grow both, we can appropriately choose the best graphene for each research application. In this section, we discuss how the domain-size of polycrystalline films was increased, and how we approached the synthesis of mm-scale individual domains.

2.2 Polycrystalline Graphene

To establish a robust recipe for polycrystalline graphene, we start with the aim of growing monolayer graphene films across large areas. Desired attributes for the recipe would be mostly monolayer (<5% adlayer graphene), complete coverage of copper foil (no areas of no graphene), fast growth time (1 hour max growth duration), and high throughput. Our CVD system is a First Nano Easy Tube 3000 CVD system with 5-inch diameter quartz tube, and a 4 x 6-inch quartz-loading arm.

With this set up, we can easily load four flat (pita pocket geometry will be discussed later for single crystal growth), 5 x 5cm copper foils for growth, which addresses high throughput for graphene synthesis. A summary of general graphene growth procedure is outlined in Fig. 2.1.
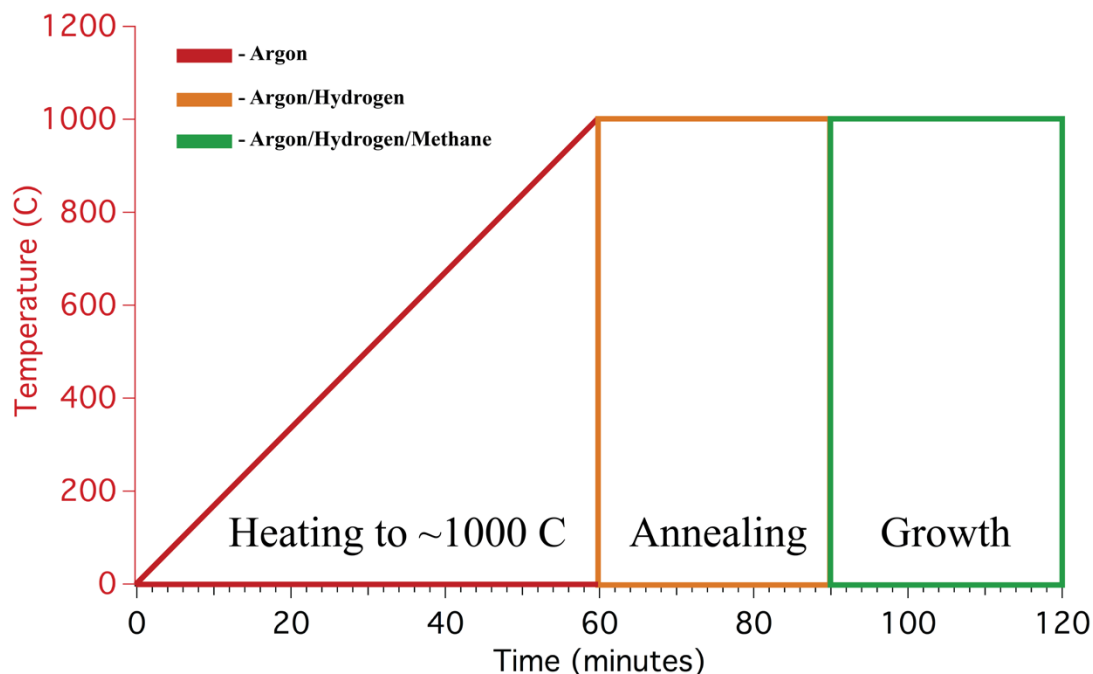
Figure 2.1: Graphene CVD growth stages for typical recipe including heating, annealing, and growth.

Copper foils are loaded into the growth chamber. The entire CVD process takes place while being pump by a dry-scroll pump. The sample is heated to ~1000 C under argon. After reaching the desired temperature, hydrogen is introduced for a short annealing period. Methane is then introduced into the system to start graphene growth. After desired growth duration, the system is cooled to room temperature under the same hydrogen and methane flows as the growth portion.

We changed the methane mass flow controllers to operate in the range of 0 - 200 sccm for initial experiments to increase grain size by decreasing methane flow rate. To assess the grain structure of the graphene films, we stop growth before a full film is grown (full films can be allowed to grow if we grow longer than this short duration). Because copper oxidizes in air very easily when heated, by heating the copper foil on a hot plate after growth, we can visualize where the graphene grows by observing the contrast of oxidized and non-oxidized regions; area's that contain

graphene protect the underlying copper from oxidation. Fig. 2.2 shows a series of optical microscopy images of oxidized copper foils after growth, and how decreasing methane flow rate can help increase nucleation size.
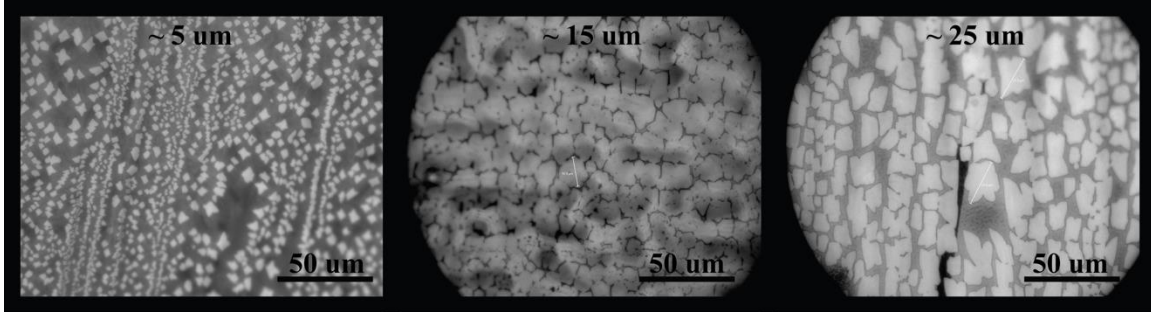
Figure 2.2: Optical microscopy images of copper foil oxidized on a hotplate after graphene growth to visual graphene domains. Grain sizes increase with decrease in methane low rate.

To assess the quality of the graphene growth, we can use Raman spectroscopy to give us feedback on the synthesized films. Fig. 2.3 shows a Raman spectra after transfer of the polycrystalline film onto a SiO_2 substrate; a Raman measurement from a commercial supplier is shown for comparison in the inset.
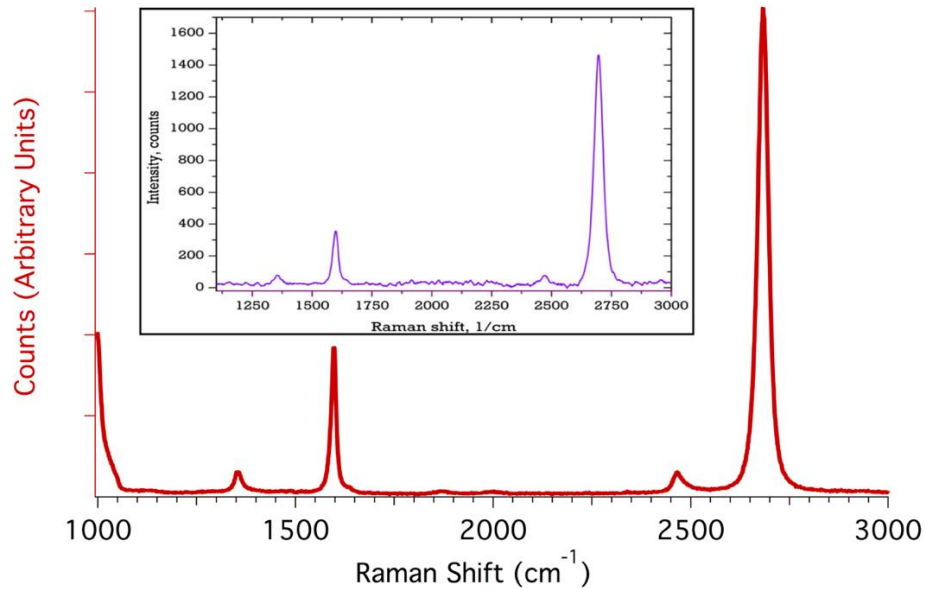
Figure 2.3: Raman spectra of synthesized monolayer graphene. The well known, G (~1583 cm^{-1}) and 2D (~2683 cm^{-1}) peaks are observed. Inset shows spectra from monolayer graphene from a commercial supplier (Graphene-Supermarket) for comparison.

The characteristic graphene peaks, the G and 2D peaks, are apparent at ~1583 cm-1 and ~2683, respectively[43]. The small D peak at ~1350, typical on samples transferred to SiO2, in combination with the fact that the ratio of intensities of the 2D:G is greater than 2, indicate high quality monolayer graphene films. These monolayer polycrystalline films are facile to synthesize, and provide major contribution to numerous research projects including microfluidic biosensors, graphene-THz modulators, and new transfer methods

2.3 Copper Oxidation for Single Crystal Graphene

We also explored the growth of mm-scale single crystal graphene. Following the CVD growth outline above, we discuss our findings and how it compares to the state-of-the-art literature for single-crystal graphene.

Initial studies of the graphene CVD process usually employed low-pressure growth systems, or atmospheric growth systems with hydrogen and methane concentrations that were heavily diluted in argon[4,27,44]. One reason these systems and growth protocols emerged was to keep the concentration of oxygen low, as it was known to be detrimental to graphene growth. The role of oxygen has since been investigated in detail, and contrasting to initial beliefs, can be a major tool in growing large area single crystals[22,23]. Graphene tends to nucleate at defect sites such as copper step-edges, impurities, and defects, as these sites act as sinks for strong binding of surface adsorbates. For the same reason, oxygen can absorb and passivate these surface-active sites to hydrocarbon accumulation (which is also why oxygen can be detrimental when trying to grow graphene films of full coverage). During the CVD process, surface oxygen can consequently be reduced during growth

by hydrogen, thus surface oxygen concentration will change over time. Understanding this basic theory allows us to optimize parameters such as annealing, oxygen exposure, and hydrogen/methane growth times and flow.

To prepare copper foils for CVD growth, one side of a ~ 5 x 5 cm sample of 25um thick copper foil from Alfa Aaser (#13382) is electropolished for 1 minute at 5 V in a solution of deionized water, phosphoric acid, ethanol, isopropyl alcohol, and urea as described in Ref[45]Following rinsing in deionized water and ethanol, the copper sample is gently blown dry, and placed on a 200 C hotplate for 1 min to undergo surface oxidation. Fig. 2.8, samples are typically oxidized for 1 minute, as this was found to be the optimal heating duration. The copper foil is then folded in half, and the sides are carefully crimped to create a copper pocket for CVD growth as seen in Fig. 2.4.
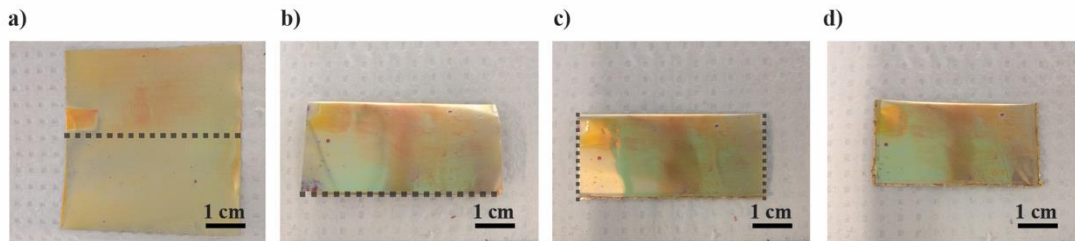
Figure 2.4: Optical images of construction of enclosed copper pockets following electropolishing and hotplate oxidation of ~ 5 x 5 cm copper foil. Copper foil is folded in half, and the remaining 3 sides are carefully crimped to create the enclosed copper pocket. Dotted line shows where the copper foil is folded/crimped.

Using the standard polycrystalline recipe for hydrogen: methane ratio, we started to explore the use of oxygen exposure after annealing. Fig. 2.5 shows two different growths of the same argon, hydrogen, and methane flow rates and ratio (growth time is adjusted accordingly to not grow full films in order to monitor grains size), except one is with oxygen and one is without oxygen exposure.

Standard Growth   **With Oxygen Exposure**

~ 25 um   ~ 210 um

50 um   50 um
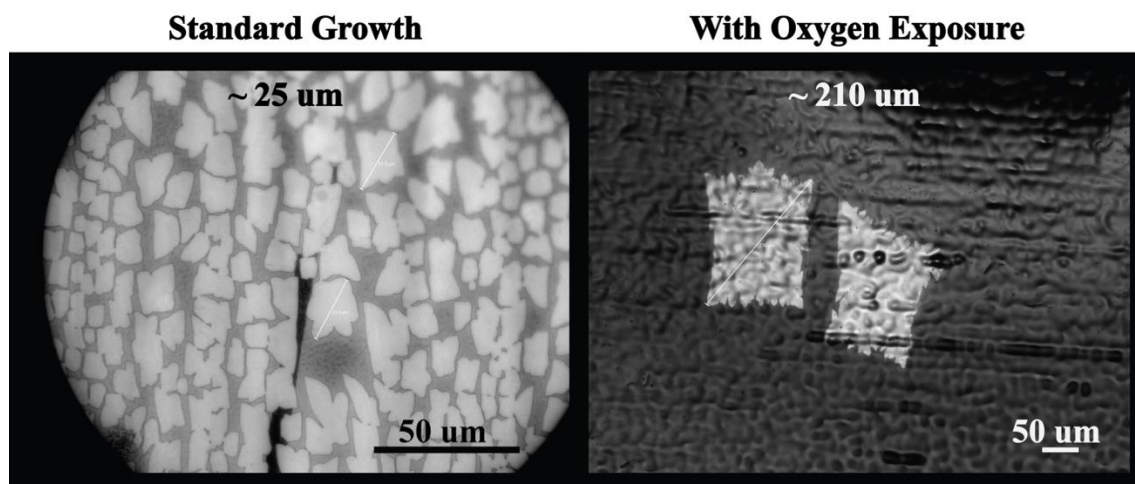
Figure 2.5: Optical microscopy images of graphene on oxidized copper. Comparison of graphene growth without (left) and with (right) oxygen exposure. Oxygen helps decrease nucleation, leading to an increase in grain size.

It is obvious that with the addition of oxygen exposure, the nucleation density of the graphene growth decreases, and overtime, this leads to greater grain size. After we confirmed that oxygen exposure did, indeed, drastically decrease nucleation density, we monitored how large our crystals could grow under the same growth conditions, but varying growth time. Fig. 2.6 shows two different of growths under the same growth and oxygen exposure parameters, but different (extended) growth times.

1 Hour Growth   **3 Hour Growth**

~ 210 um   ~ 770 um

50 um   50 um
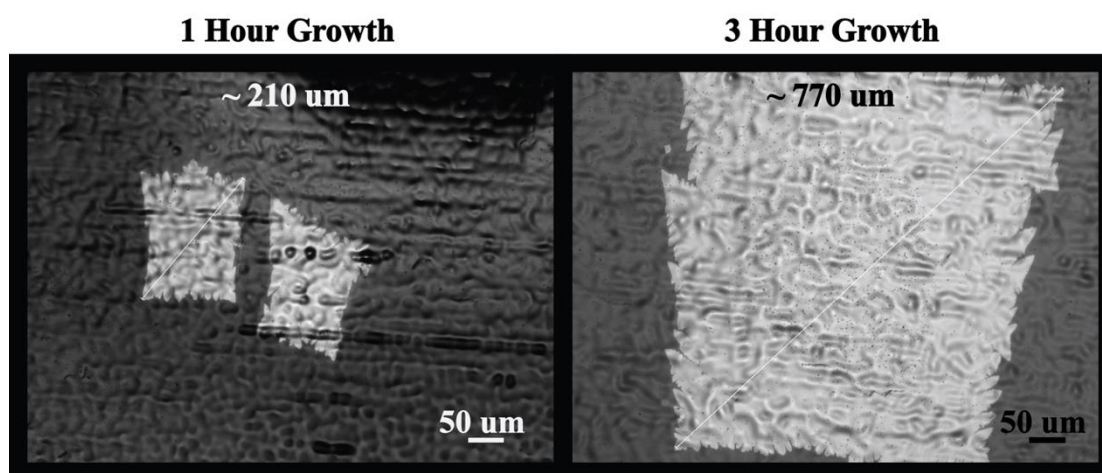
Figure 2.6: Optical microscopy images of graphene on oxidized copper. (Right) shows growths with longer growth duration. Obviously, extending growth time leads to increased grain size.

We found that, although increasing growth time did increase grain size by allowing the existing domains to continue to grow, this method is limited by the nucleation density, since as crystals grow bigger and bigger, they will eventually merge to form films. Thus, it is of high importance to decrease nucleation density, in order then allow for large crystal growth. This balance of nucleation density versus grain size is clearly displayed in Fig. 2.7, which shows two growths of identical conditions, but increased growth time. Because the nucleation density stays the same, an increase of grain growth eventually leads to the formation of films and connected networks of single-crystals.
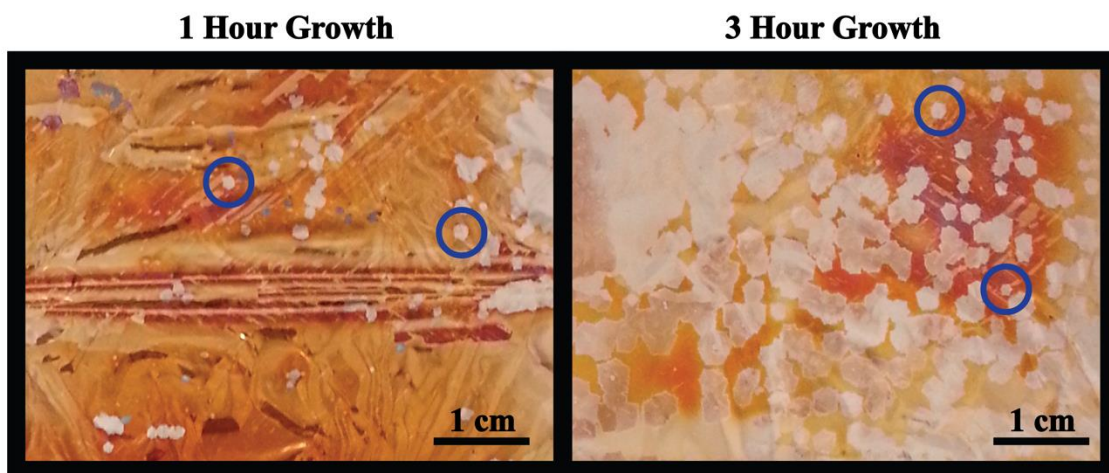
Figure 2.7: Optical images of graphene on oxidized copper. Extending growth duration increases grain size, but since nucleation density is high, grains connect to create single-domain networks. Blue circles are present to help identify isolated single domains.

Although oxygen is a useful tool to decreasing graphene growth nucleation density, a number of other key factors also play important roles in determining nucleation density including heating/annealing conditions, and formation of surface nanoparticles[23,24]. In addition to using a mid-growth oxygen exposure to introduce surface oxygen, alternative methods have been introduced in the literature

including heating copper foils ex-situ on a hotplate, and annealing under argon with trace amounts of oxygen. From these experiments, researches have gained a clearer picture of the role of surface oxygen; conclusively, the achievement of large single-crystals requires the careful balance of gas (argon, hydrogen, methane/ethanol) flow and flow times in order to accurately decrease nucleation while enabling grain growth.

Briefly, it is found that heating and annealing under argon can be advantageous, since the inert environment preserves surface oxygen species (to help keep nucleation density low). Additionally, a short annealing time under hydrogen also assists in decreasing nucleation density by smoothing the copper surface (compared to the minimal smoothing effect of argon) as believed in early CVD studies. Although the smoothing of the copper surface is advantageous, hydrogen also reduces the oxide species, increasing potential nucleation sites. Furthermore, long hydrogen exposure creates the formation of "pits" in the copper surface, and subsequently, the formation of nanoparticles that act as additional nucleation sites[46]. Clearly, there is no straightforward flow rate or ratio that can be used to grow large area crystals, and usually, each system and recipe needs to be fine-tuned as to optimize growth by controlling surface oxygen species and copper surfaces. Below, we outline some key parameters that have been adjusted for large crystal growth.

We first investigate holding the growth parameters constant, while varying initial pre-growth oxidation conditions. Other groups have approached this in two ways, pre-oxidation on a hot plate, or pre-oxidation under argon (from leaks in the

CVD system). Since our furnace is constantly purged in nitrogen (thus the trace oxygen level should be low), we choose to explore oxidation on a hotplate. Fig 2.8 shows 3 growths with different duration of oxidation on a hotplate.
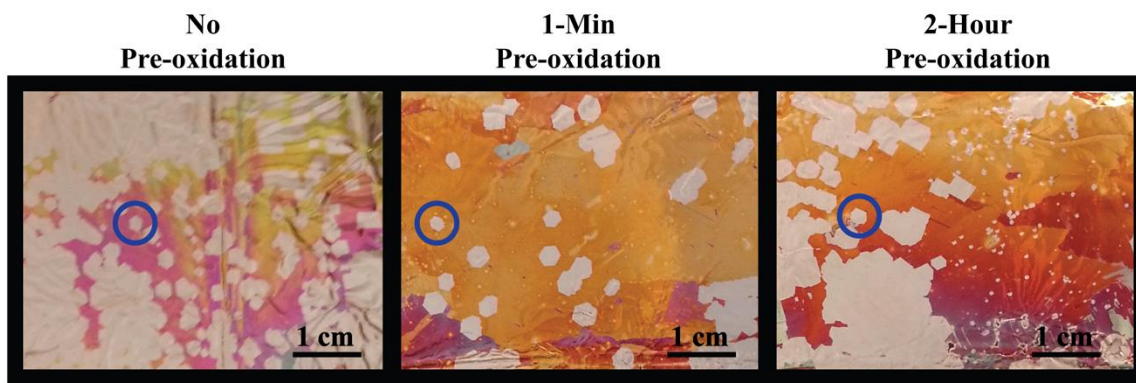
Figure 2.8: Images of graphene on oxidized copper. We study the influence of pre-oxidation on a hotplate. Results indicate that pre-oxidation helps decrease nucleation density, but over oxidation could result in additional nucleation. Blue circles are present to help identify isolated single domains.

For no oxidation, and 2-hour oxidation, the surface is nearly covered in nucleation sites. Interestingly, with only 1-minute oxidation, nucleation density is dramatically suppressed. We believe the 1-minute oxidation acts as an advantageous addition of surface oxygen that is not possible when skipping hotplate heating, since our CVD system is mostly evacuated of lingering oxygen. We theorize that 2-hour oxidation over oxidizes the surface, and thus, hydrogen works mostly to reduce the surface, and does not have sufficient time to smooth the surface.

We then investigate the role of hydrogen heating. To verify that preserving the surface oxide layer from hotplate heating decreases nucleation density, we show two samples of the same growth conditions, but with one heated under hydrogen, and the other heated under argon in Fig. 2.9.

Hydrogen Heating   **Argon Heating**
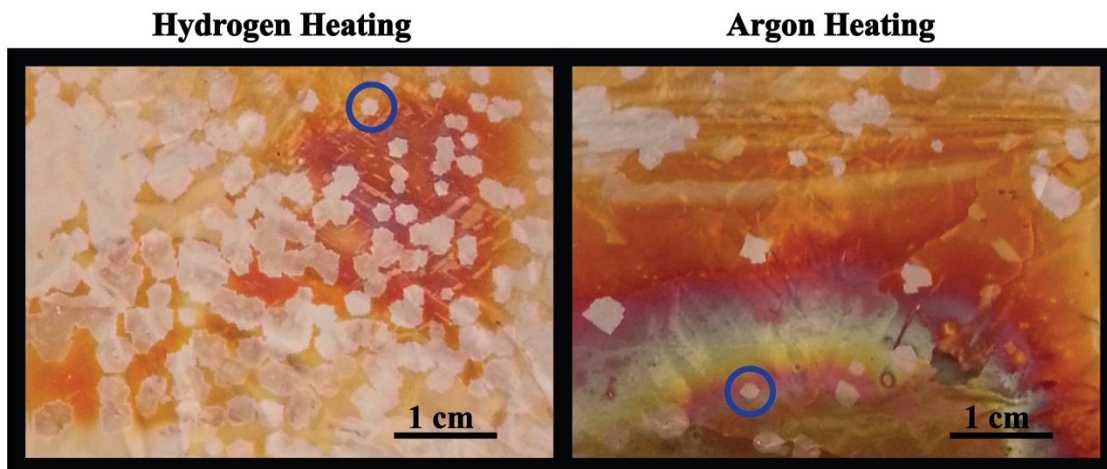
Figure 2.9: Optical image of graphene on oxidized copper. Hydrogen heating removes surface oxygen increasing nucleation, compared to heating under argon. Blue circles are present to help identify isolated single domains.

Indeed, the pure hydrogen heating sample shows a large nucleation density, compared to samples heated under argon, indicating the removal of oxygen species on the surface. The graphene samples grown in Fig. 2.9, under hydrogen and argon annealing are shown after transfer onto SiO$_2$ in Fig. 2.10.

Single Nucleation Site   **Multiple Nucleation Sites**
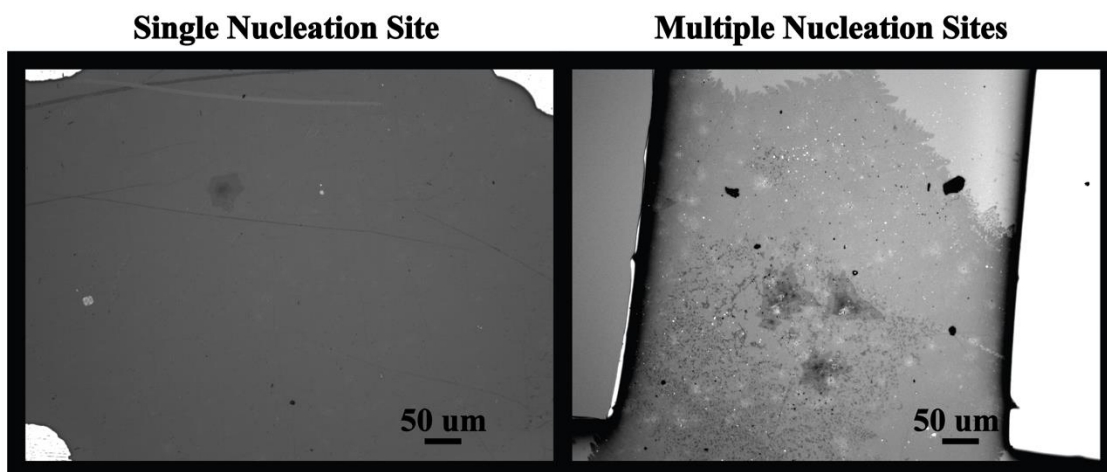
Figure 2.10: Optical microscopy image of graphene transferred onto SiO2 (gold electrodes are also seen). (Left) We observe one nucleation with some adlayer growth. (Right) The monolayer growth front is easily observed and looks nice a single nucleation site, but we can see a cluster of adlayer nucleation centers. Nucleation clusters are common for long hydrogen exposure.

The growth front appears to be of a single nucleation site, but upon further inspection, the right image shows a cluster of nucleation sites (more often observed in hydrogen recipes); this gives us evidence that after long exposure to hydrogen, growth and diffusion of surface nanoparticles create additional nucleation sites.

After the confirming that argon heating was advantageous to preserving the surface oxide accumulated during hot plate oxidation, we wanted to explore if adding a dilute hydrogen anneal could help decrease nucleation density from surface smoothing (we observed a high nucleation density in strictly argon heating and annealing). Fig. 2.11 shows a series of growths heated under argon, and annealed for 45 minutes under 10%, 33%, and 50% hydrogen.
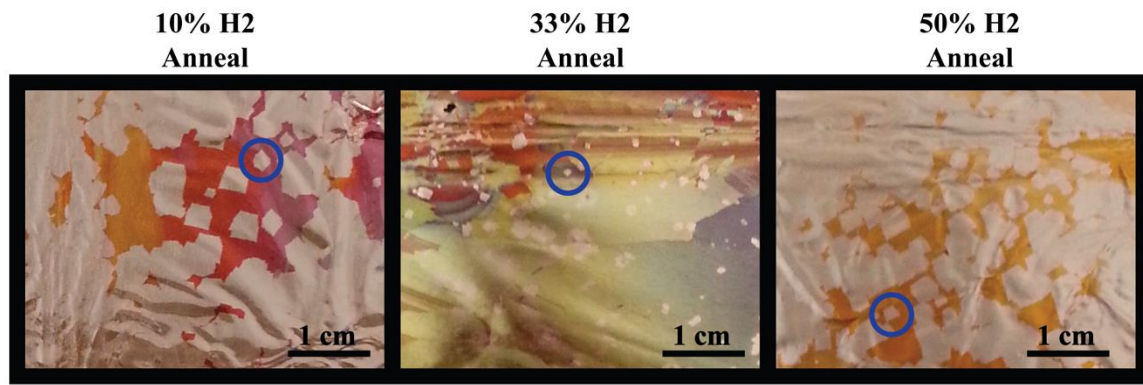
Figure 2.11: Optical image of graphene on oxidized copper. After heating under argon, the effects of hydrogen concentration during anneal are tested. We find that 33% hydrogen is the best balance of preserving surface oxygen and smoothing copper. Blue circles are present to help identify isolated single domains.

There is a stark contrast between the growths of 10% and 50% compared to that of 33%. From this experiment, we confirm that there is a tradeoff between smoothing the copper surface (decreasing nucleation density) and reducing copper oxide (increasing nucleation density) using hydrogen.

Once we found appropriate parameters for oxidation, heating, and annealing, we attempt to grow large single crystals by using a two-step fast growth method.

2.4 Fast Growth

What is the most rapid, efficient chemical vapor deposition (CVD) method to produce large-area, single-domain graphene? This task remains a challenge because rapid growth conditions usually result in concomitant high nucleation density, causing merging of domains and ultimately, full film coverage[4,26,47], prior to the growth of large domains. This results in multiple, detrimental grain boundaries[48] due to the polycrystalline nature of multi-domain films[49]. The ultimate goal, and only way to ensure that no grain boundaries exist within the graphene is the synthesis of wafer-scale, isolated single-domains. En route to reaching this goal, researchers have developed numerous methods (such as electropolishing copper foils[45], high pressure hydrogen annealing[50], low methane flow[47], and oxidized copper growth[6,23]) to minimize the nucleation density. Of these, CVD growth on oxidized copper substrates has proven to be one of the most effective[6,23] at allowing the necessary surface-area and spacing required to avoid merging of neighboring domains. However, this method, which relies on low flow rates of the carbon feedstock gas, comes at the cost of very long growth times[6,23,24,46,51], measured in days instead of hours.

We discuss a two-step CVD growth method for rapid synthesis of isolated large-domain graphene. The key feature of the two-step growth method is to separate nucleation from growth, performing the nucleation in step-one with a low feedstock gas (methane) flow rate, and rapid growth in step-two with a high flow

rate. We find empirically that, even under the high flow rate conditions of step-two, the nucleation density is suppressed by the geometry of the copper pocket[45] used, until the outside of the copper pocket is fully covered by a graphene film. During step-two (the high growth rate step), we are able to tune the carbon concentration on the inside of the copper pocket to be *above* the threshold concentration required for edge growth, but *below* the threshold concentration required for nucleation[52], even in the presence of high methane flow rates. Operating in this regime produces large-domain graphene without the formation of full films, ensuring that no detrimental grain boundaries develop.

A unique combination of mechanisms enables us to grow in this regime. While a quantitative model is still not available, the mechanisms involved are believed to include 1) passivation of active nucleation sites through oxidation of the copper surface[23], 2) reduction of the energy barrier for edge-attachment growth resulting from the de-hydrogenation of methane by the oxidized copper surface[6], and 3) a unique carbon concentration profile (resulting from the role of carbon sources and sinks at the inside and outside due to nucleation, growth, and diffusion of carbon through the copper bulk[53], in both directions). This "window" has not been explored previously in the literature. Furthermore, we show that this "window" of opportunity exists only when the outside is not fully covered with graphene. Once the outside surface is covered, the nucleation density on the inner surface increases dramatically, and quickly results in fully merged films with grain boundaries, rather than isolated single domains (the goal of this work). Using this

approach, we demonstrate growth of 5-mm isolated graphene domains in less than

5 hours of total growth time, much faster than traditional one-step growth methods.

We performed CVD graphene growth using enclosed copper pockets due to the improved surface conditions and decreased diffusivity, and hence, decreased nucleation and growth rate in the interior surface as reported in previous CVD studies[45,47,53]. Our findings regarding diffusion from the inside surface to the outside surface of the copper pocket will be discussed in depth, later in the paper. Briefly, a copper pocket is used, and large-domains grow on the inside. Our studies show a critical role of the surface coverage of the outside surface influencing growth on the inside, elucidated in detail below. Preparation of the enclosed copper pocket is documented in the methods and supporting information Fig. 2.4. Before growth optimization (two-step growth) experiments were conducted, we monitored and adjusted pre-growth conditions (excluding methane flow rate) to achieve the lowest nucleation density possible. These results including oxidation conditions[6,51], annealing conditions[23,50], and heating gases[24,46] are documented in Fig. 2.8-2.11. These parameters are held constant throughout the remainder of experiments including two-step growth studies.
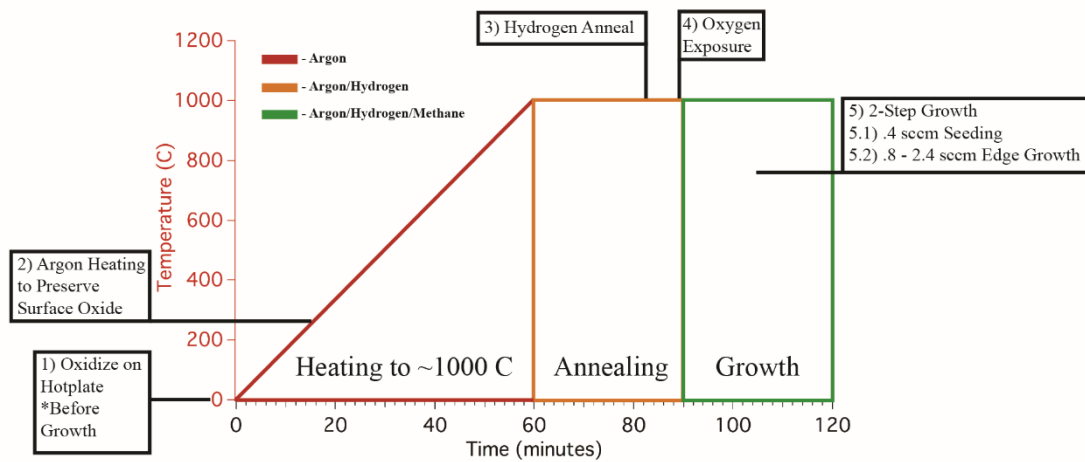
Figure 2.12: A general outline for typical two-step growth including pre-growth optimization.

CVD growth of graphene is performed using a First Nano Easy Tube 3000 inside a 5-inch quartz tube. Copper pockets are loaded into the growth chamber and the tube is evacuated at the beginning of each growth. (Fig. 2.12) depicts a typical growth recipe. The furnace is heated to the desired growth temperature under argon, followed by a 45 minute anneal in 33% hydrogen. We chose to expose the copper samples to an additional 50% oxygen exposure at elevated temperatures for 6 minutes to further suppress nucleation. Graphene synthesis is allowed to occur under the flow of 100 sccm argon, 150 sccm hydrogen, and 0.4 – 2.4 sccm methane while constantly evacuated by a dry scroll vacuum pump.

Typically, for one-step growth procedures, a low methane flow rate is used over long durations in order to keep the nucleation density low[6,23,24,46,51]. This methodology to achieve low nucleation density comes at the cost that the growth rate is also low[6,23,24,46,51], especially since the growth rate decreases overtime[54]. As verified in Fig. 2.13, when using a low methane flow rate (0.4 sccm), distinct mm-sized domains appear in low density, but long growth durations have limited effects on increasing domain size.
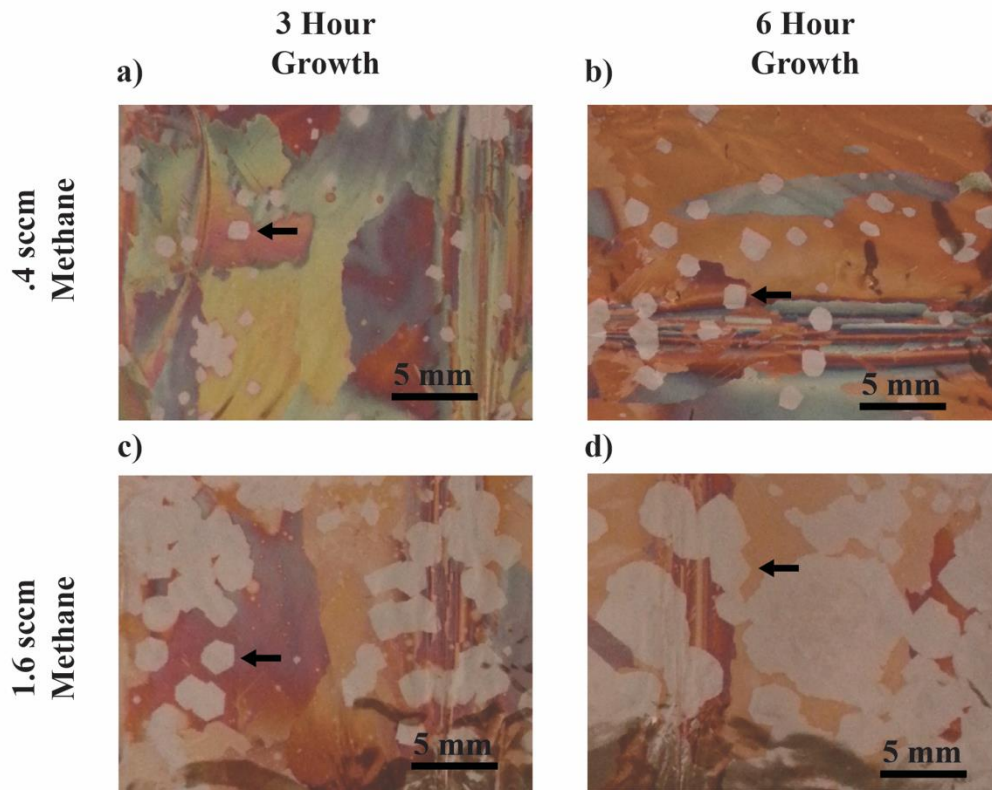
Figure 2.13: a-d) The results of control experiments for one-step growth for .4 sccm and 1.6 sccm for both 3 hours and 6 hour growth duration. Black arrows are provided to identify single-domains. Low methane flow rates produce distinct, individual domains that are limited in size, while elevated flow rates yield larger, merged domains.

To assess if a high methane flow rate could be used to synthesis large-domain graphene, we performed a series of one-step growths using elevated methane flow

rates (1.6 sccm) to probe the domain-size and nucleation density overtime Fig. 2.15a. Following growth, the enclosed copper pockets are cut open, and oxidized on a hotplate to reveal graphene growth coverage[55]. (Fig. 2.15b-d) shows a depiction and experimental verification that using elevated methane flow rates can noticeably increase the graphene domain-size, but due to the increased nucleation density (Fig. 2.14c-d), results in the formation of merged domains, and ultimately, continuous graphene films, as the growth duration proceeds.
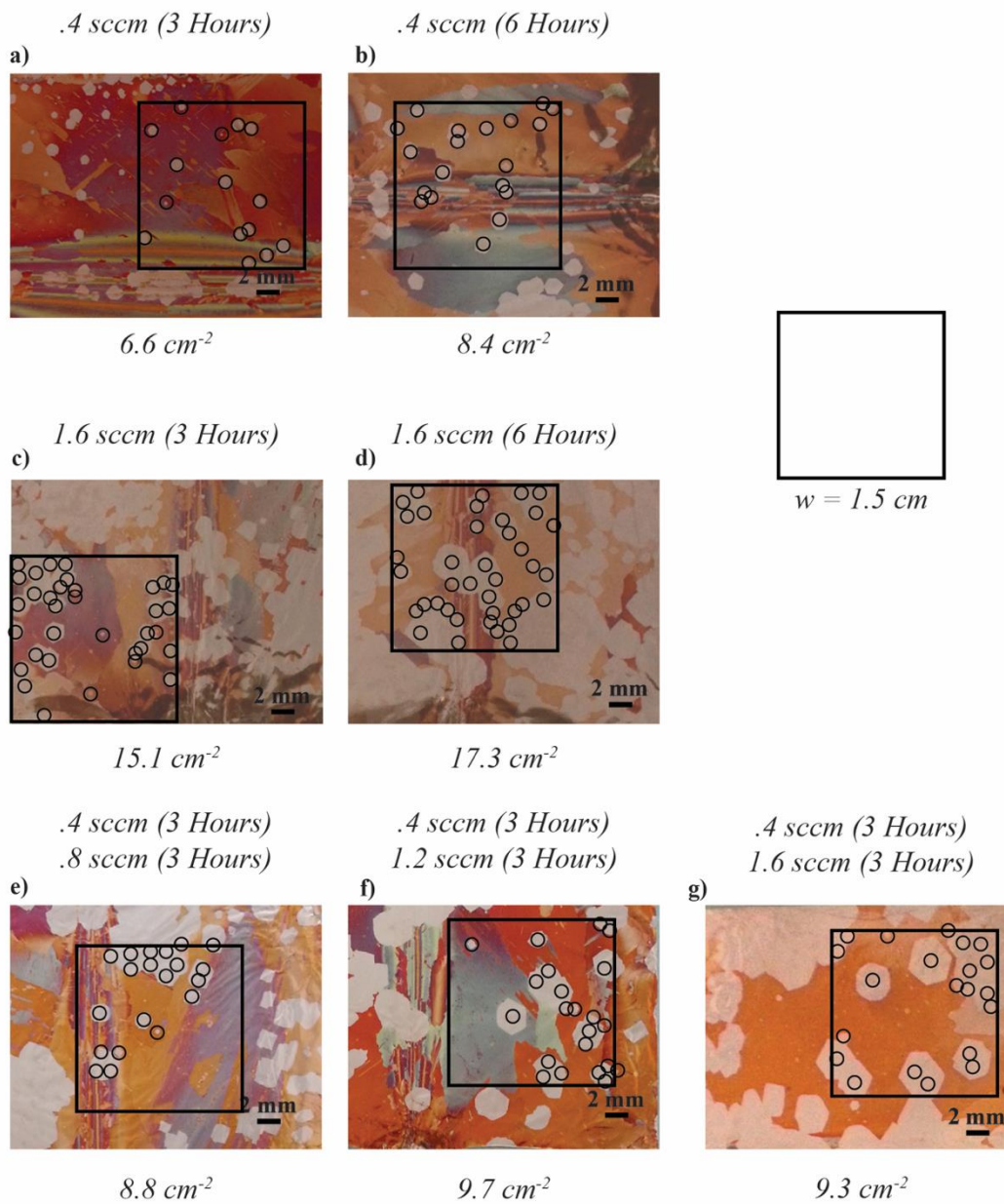
Figure 2.14: To estimate the local nucleation density for both one-step and two-step growth procedures, we used a standard of an area of 1.5 cm width to assess locations of low nucleation. a-b) shows the nucleation density for a one-step growth using low methane flow rates which results in low nucleation density. c-d) shows an increase of the nucleation density as the methane flow rate is increased for a one-step growth. e-g) shows that when using a nucleation step, allows the nucleation density to remain low, despite using elevated methane flow rates compared to one-step growth of the same flow rate and growth duration.

From these control studies, we confirm that in order to synthesize large-domain graphene using an increased methane flow rate (in order to decrease the

overall growth duration), without the detriment of increased nucleation density (which would limit the ultimate size of isolated graphene domains), a traditional one-step growth protocol is not adequate.
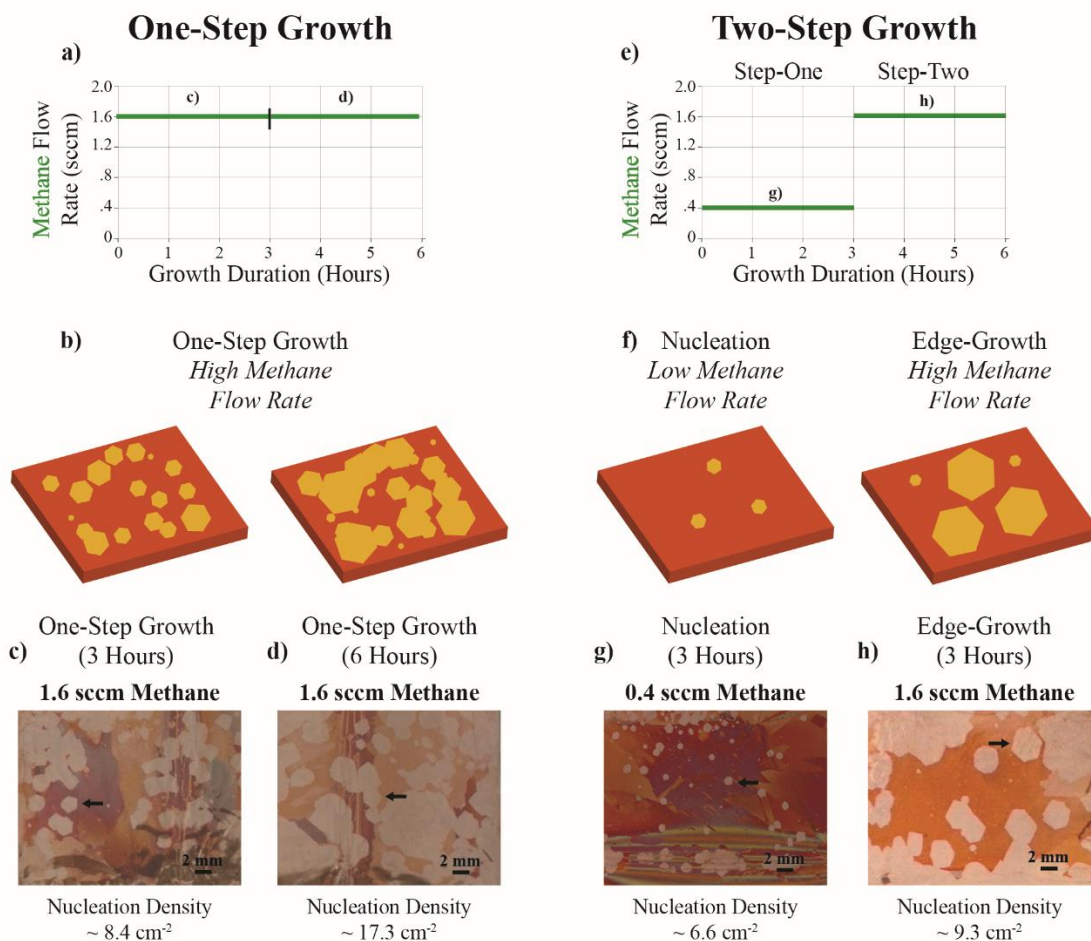
Figure 2.15: a) Outline of typical one-step growth, using high methane flow rate b) cartoon depicting graphene growth using high methane flow rate resulting in high nucleation density, which forms full films after long duration. c-d) Optical images of oxidized copper after one-step growth for 3-hour, and 6-hour duration. e) Outline of two-step growth, using low methane flow rate stage, followed by high methane flow rate stage. f) Cartoon depicting graphene growth using two-step growth. Step-one creates a low nucleation density by using low methane flow rates. Step-two promotes edge-growth using elevated methane flow rates. g-h) Optical images of oxidized copper after step-one, and step-two. Step-one (.4 sccm) produces domains of low nucleation density; step-two (1.6 sccm) increases the size of isolated domains. Black arrows point to graphene domains.

The two-step growth protocol employed here, outlined in (Fig. 2.15e), consists of a low methane flow rate stage, followed by a high methane flow rate

stage. Argon and hydrogen flow rates are kept constant throughout the entire growth duration. Step-one is intended to achieve a low nucleation density in order to allow the adequate surface area to grow isolated, large-area single-domain graphene, whereas step-two is aimed at enlarging the size of existing nucleated domains (Fig. 2.15f). Previous studies using two-step growth were designed to increase the nucleation density after large-domain graphene was synthesized in order to fill-in voids, and ultimately, create large-domain films[26], whereas our main aim is to avoid merging of domains by maintaining a low nucleation density. (Fig. 2.15g-h) shows growths after step-one, and step-two, and demonstrates that despite the increased growth rate (from the increased methane flow rate) during step-two, the nucleation density is does not dramatically increase (Fig. 2.14g), such that isolated domains are still apparent. The mechanisms that enable these experimental results are believed to be related to the diffusion of carbon species in copper, specifically to copper pocket growths, and will be discussed in detail below. Regardless of the mechanism, by using our two-step growth process, we are able to synthesize isolated, 5-mm single-domain graphene in less than 5 hours.

Following two-step synthesis, we employed a series of characterization techniques to assess the quality of the synthesized graphene, and to fully confirm that the graphene is neither polycrystalline nor multilayer. First, scanning electron microscopy (SEM) was used to image graphene on the copper foils; we found that the 120-degree angle of the domain growth front, and the lack of observable defects or boundaries highly advocate that the synthesized graphene is single-domain[50] as shown in (Fig. 2.17a). Optical images of transferred[7,56] single-domains onto silicon

oxide (SiO₂) show that the majority of the domain area is monolayer, with only a small nucleation center consisting of ad-layer graphene present (Fig. 2.17b). To further substantiate the growth of monolayer, single-domain graphene, we used selected area electron diffraction (SAED) to investigate the crystal structure of domains transferred[7,56] onto Transmission Electron Microscopy (TEM) grids. (Fig. 2.17c) shows a typical SAED pattern, recorded from one single domain and verifies that the graphene domain is single crystal[57]. (Fig. 2.16) shows a collection of SAED patterns from one single-domain spanning 2 mm².
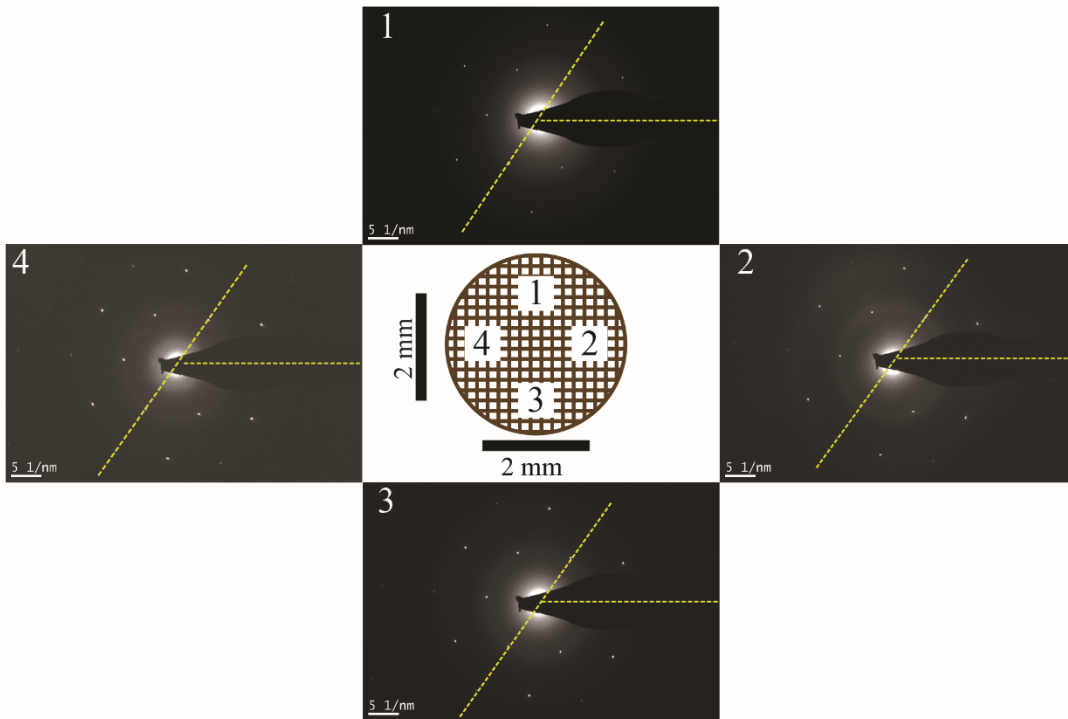
Figure 2.16: SAED patterns of single-domain graphene over 2-mm² area. The alignment angle of the electron diffraction pattern varies by less than 2 degrees, and further supports the synthesis of large-area single-domains.

The alignment angle of the electron diffraction patterns are within 2 degrees of variation (the single domain graphene was laid on a copper TEM grid, and as a consequence, patterns recorded across large distances vary from bending of the

32

TEM grid) and further supports the growth of single-domains[49,50]. Raman spectroscopy was used to assess the quality of single-domain graphene transferred onto an OctadecylTriChloroSilane (ODTS) modified SiO_2 substrate (as to minimize substrate effects)[58]. (Fig. 2.17d) shows a representative Raman spectra of a single-domain. (Fig. 2.17e-g) shows the intensity of the G-peak (~1583), 2D-peak(~2683), and the D-peak (~1350) collected for a sample using Raman mapping, respectively[43]. In all 3 intensity-mapping images, a clear boundary between the graphene and the substrate is obvious. A small patch of PMMA contamination near the bottom of the graphene sample is also evident[59]. The lack of D-peak[60] (except around the graphene boundary, and PMMA contamination), in addition to the large ratio of 2D:G intensities[59,61] (> 3:1) (Fig. 2.17h), indicates a very high-quality monolayer of graphene. Altogether, our characterization methods confirm that the synthesized graphene using two-step growth is monolayer, and single-domain.
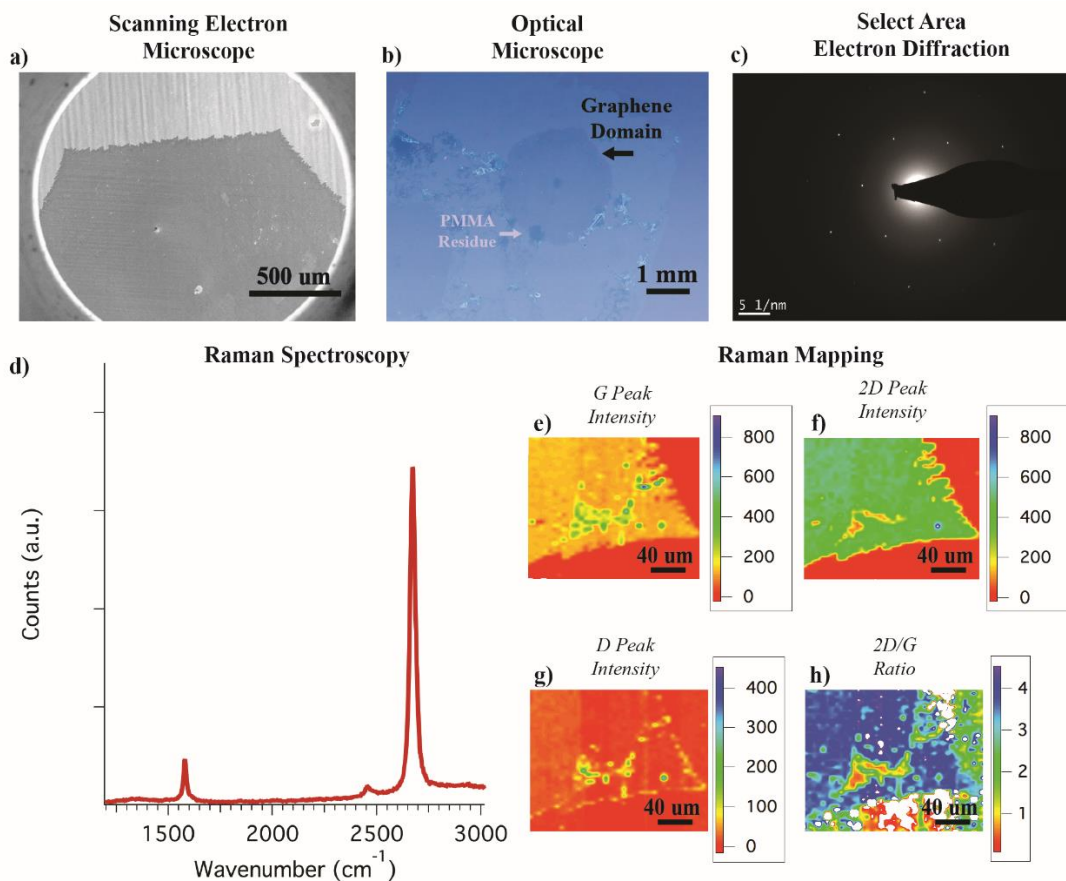
Figure 2.17: a) SEM image of hexagonal growth edge of large-domain graphene synthesized using two-step growth. **b)** Optical image of large-domain graphene transferred onto SiO₂ substrate. The majority of the domain is monolayer, with a small observable nucleation center consisting of adlayer graphene. **c)** A representative SAED pattern of one single-domain showing the single crystal nature of the domain. **d)** A representative Raman Spectra of monolayer graphene **e-g)** Raman mapping images of single-domain graphene on a domain corner to spatially track intensities of the G peak, 2D Peak and D Peak, respectively. Defects are observed on a small patch of PMMA contamination near the bottom edge of the domain, and on the domain-edge. **h)** The ratio of the intensity of the 2D:G peaks is greater than 3:1 for the majority of the single-domain, and further confirms high quality, monolayer graphene is synthesized.

To investigate the dependence on the methane flow rate during two-step growth, we performed a series of growths, varying the methane flow rate using the two-step process. Step-one, and step-two were both held for 3-hour duration each. (Fig. 22a) shows an optical image of the inside surface of the copper pockets after 3 hours of low methane exposure (step-one growth). Distinct mm-sized domains

appear spread across the inside surface, with the adequate spacing necessary for edge-growth during step-two (Fig. 2.14a).
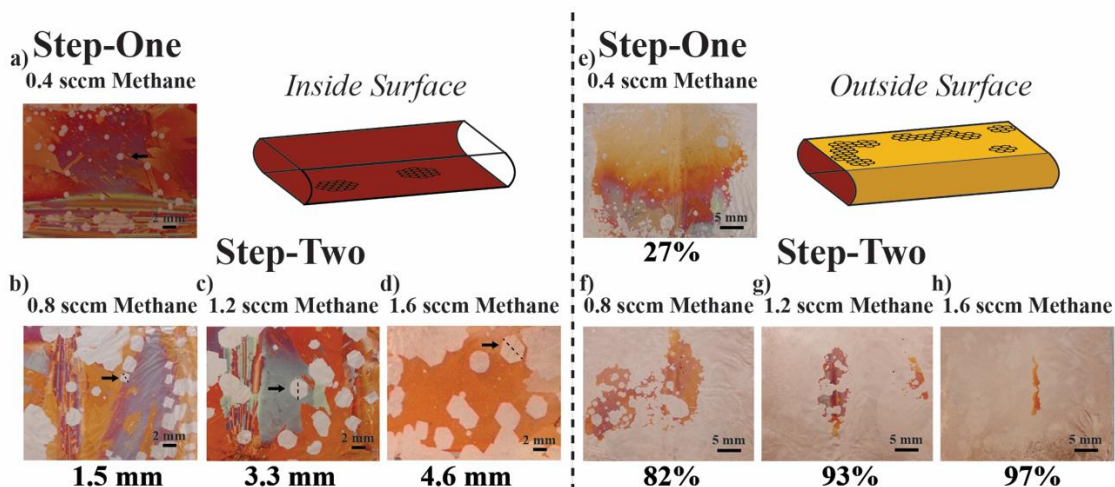
Figure 2.18: a) Optical image of graphene on the inside of copper pockets following copper oxidation after step-one. Step-one uses low methane flow (.4 sccm) over 3 hours to create low density of nucleation. b-d) Optical images of graphene on the inside of copper pockets following copper oxidation after two-step growth varying the second-step flow rate from .8, 1.2, to 1.6 sccm, respectively. By increasing the methane flow rate (for step-two) the average domain-size increases, without the need to increase growth duration. e-h) Optical images of graphene on the outside of copper pockets following copper oxidation after step-one and step-two. Increases in methane flow rate (step-two) causes an increase of growth on the outside, with greater percent coverage for greater methane flow rate. Using 1.6 sccm methane for the step-two flow rate (for 3 hours) results in nearly full coverage of the outside surface. Black arrows point to graphene domains.

After defining the low nucleation density set in step-one, we monitored the effects of increasing the flow rate for step-two. (Fig. 2.18b-d) shows a series of optical images of the inside of the copper pockets after two-step growth using identical conditions for the step-one (0.4 sccm), but with increasing methane flow rate for the second step, ranging from 0.8 – 1.6 sccm, respectively. Interestingly, by using a two-step growth process, we do not observe a dramatic increase in the nucleation density of graphene domains to the extent that isolated domains exist, even though the methane flow rate is increased incrementally for each experiment (Fig. 2.14e-g). Moreover, as the second-step flow rate is increased, from 0.8 to 1.2,

and then to 1.6 sccm, the average domain-size increases for respective increases in flow rate, without the need to increase the growth duration.

Using a two-step growth, it is possible to control the size of large-area single-domains by choosing the corresponding step-two methane flow rate. Compared to the single-step growth using low methane flow (0.4 sccm) (Fig. 2.13b), using a two-step growth over the equivalent growth duration, results in larger domain-sizes (for all flow rates, 0.8, 1.2, and 1.6 sccm). Furthermore, the increase in methane flow rate effectively increases the graphene domain-size, without the expense of additional ad-layer coverage (Fig. 2.19).
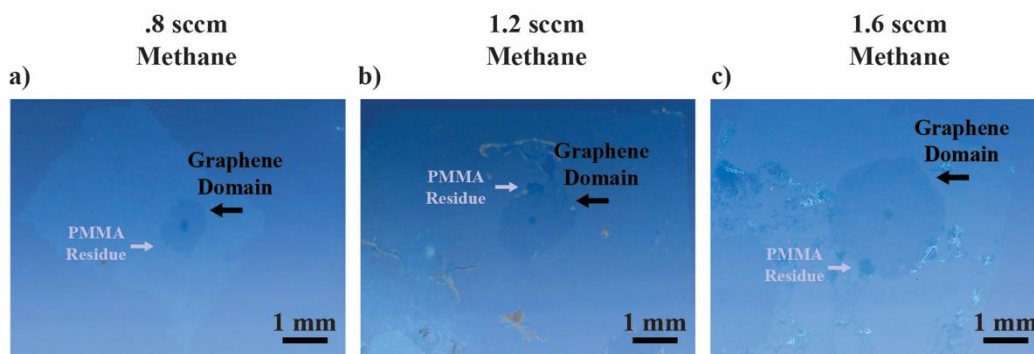
Figure 2.19: Optical images of large-domain graphene transferred onto SiO₂ substrate. The domain-size increases for increases of step-two, methane flow rate, without expanding the area of the adlayer nucleation center.

Thus, we have shown that by using a two-step growth protocol, it is feasible to promote domain-edge growth while simultaneously controlling the nucleation density.

Why does the nucleation density not increase with an increase in the step-two methane flow rate as revealed in our experiments? The use of high methane flow rate to grow large-domain graphene while retaining a low nucleation density

seems contradictory to previous experiments[6,23,24,26,46,47,50,51,55], and indicates that other factors play a key role in limiting the overall nucleation density inside the copper pocket. To investigate why elevated methane flow rates could result in low nucleation density instead of full graphene films, we monitored graphene growth both on the inside and outside surface of the copper pocket following two-step growth. We observe that after step-one (Fig. 2.18e), the majority of the outside surface remains uncovered (27% surface coverage); as the flow rate is increased from 0.8 sccm, up to 1.6 sccm for step-two, we notice that the surface coverage of the copper foil subsequently increases, up to nearly full coverage (97%) for the largest flow rate (Fig. 2.18f-h). Clearly, increases in step-two methane flow rate increase the overall growth rate[47,52,54], generating the increase in domain-size on the inside surface, and increasing coverage on the outside surface.

We found a significant transition occurs whenever the outside surface was fully covered. When we used step-two flow rates larger than 1.6 sccm (97% outside surface coverage), such as 2.4 sccm, the inside surface contains merged graphene domains, not isolated single-domains (Fig. 2.22a-b). This apparent increase in nucleation density corresponds to full graphene coverage on the outside surface (100%). These results provide an important clue on how two-step growth preserves a low nucleation density inside the copper pocket during elevated methane flow rates. To assess if the formation of a full film on the outside surface is related to the increase of the nucleation density inside, or merely a result of using elevated methane flow rates, we investigated the influence of the growth duration of step-two, maintaining elevated methane flow rates.

The increased growth rate that occurs from using elevated methane flow rates results in faster coverage of the outside surface; thus, by decreasing the overall growth duration we are able to probe the influence of elevated methane flow on the nucleation density on the inside surface, before a full film exists on the outside. Despite using high methane flow rates (2.4 sccm), reducing the growth duration of step-two (from 3 hours to 1.5 hours) to avoid formation of a full film on the outside, results in the growth of isolated, large-domain graphene on the inside surface (Fig. 2.22c-d). Similar results tuning the growth duration to avoid full film coverage are shown in (Fig. 2.20a-d) for an additional elevated methane flow rate.

Within Nucleation Threshold

2.0 sccm Methane (3 Hours)

a) *Inside* b) *Outside*

2.0 sccm Methane (2 Hours)

c) *Inside* d) *Outside*

5 mm 5 mm 5 mm 5 mm

Beyond Nucleation Threshold

2.7 sccm Methane (1 Hour)

e) *Inside* f) *Outside*

3.0 sccm Methane (1 Hour)

g) *Inside* h) *Outside*

5 mm 5 mm 5 mm 5 mm
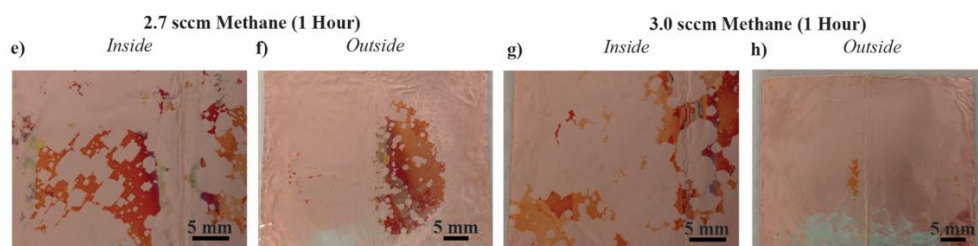
Figure 2.20: Control experiments for limiting nucleation density by monitoring outside growth coverage. a-b) Using 2.0 sccm methane for 3 hours produces increased nucleation density inside, due to full coverage of growth outside. c-d) If we reduce growth duration to 2 hours, we maintain the low nucleation density inside and observe that the copper surface on the outside is not fully covered. e-h) For very high methane flow rates (2.7 sccm, 3.0 sccm) the growth rate is pushed beyond the nucleation threshold, thus diffusion through the copper bulk is not adequate to limiting the nucleation rate when the outside surface is persevered (even when restricting growth to 1 hour), as evident in the widespread formation of small-domain graphene in between large domain sites. At 3.0 sccm (1 hour) the large-domains are almost indistinguishable from the formation of films.

Thus, we show that the nucleation density inside remains low, only when the outside surface remains uncovered (by adjusting methane flow rate, or growth duration). We have verified this method of synthesizing isolated large domains with over 80 successful growth runs. Regardless of the mechanisms dictating this trend, we can exploit the fast growth rate (using high methane flow rates) and curb the increase of nucleation density by avoiding full film coverage on the outside surface, in parallel. This allows the overall growth duration to be severely reduced when synthesizing isolated large-domain graphene. (Fig. 2.22e) shows an optical image of the inside of a copper foil following a two-step growth with only a 4.5-hour (total) growth duration. We are able to grow isolated, large-domain graphene up to 5 mm

in domain-size utilizing the high methane flow rate of step-two, and by tuning the growth duration to avoid full films on the outside to keep nucleation low inside. The majority of the growth duration is the slow, step-one stage (3 hours), where low nucleation density is first established. Compared to other methods that utilize only a single-step growth on oxidized copper substrates, our two-step growth method can be up to 10 times faster than conventional, one-step methods[6,23,24,46,51] (Fig. 2.22f). Until the ultimate goal of a wafer-scale single-domain graphene without grain boundaries is achieved, for various large-area graphene applications where grain boundaries could be detrimental, continuous monolayer films of merged large-domains can be useful. Using our two-step method, it is simple to grow a full film (as shown in Fig. 2.22a) consisting of large-domain graphene on the inside surface of the copper pocket by extending the growth duration. We investigated the merging of the large-domain graphene to form full films as the two-step growth duration progressed. Fig. 2.21a-d shows the growth of isolated large-domains from short growth periods (as demonstrated as the main goal of this paper), until the merging of these isolated domains (towards a continuous film) as the growth duration is extended. The time evolution of the two-step growth suggests that the resultant continuous films start off as large-domain graphene, and possibly concludes with some areas being patched together by smaller domains, which nucleate as the growth extends. We further investigated the merging of these films using SEM. Fig. 2.21e-f shows SEM images of graphene on copper on an area shortly before the full merging of large-domain crystals; an arrow is provided to help locate where two distinct large-domains merge with no observable defects. The large growth front observed under SEM before full film growth suggests the merging of large-

domains consist of domains at least hundreds of microns in size. Fig. 2.21g-h shows a continuous 1cm x 1cm large-domain film transferred onto a SiO2 substrate. Under optical microscopy, no detrimental defects other than the typical, transfer-induced features such as wrinkles, tears, and PMMA residual contamination are observed. To further confirm that the continuous graphene film consists of large-domain graphene, we employed UV exposure of the full films after growth on copper to reveal the grain boundaries[62]. Following 30 minutes of UV exposure in ambient conditions (~45% humidity), grain boundaries are observed by the preferential oxidization of copper beneath the boundary. Fig. 2.21i-j shows optical microscopy images of a full film and an observable grain boundary following UV exposure. We observed grain boundaries on the order of millimeters in length, which further suggest that large-domains merge together to form continuous films.
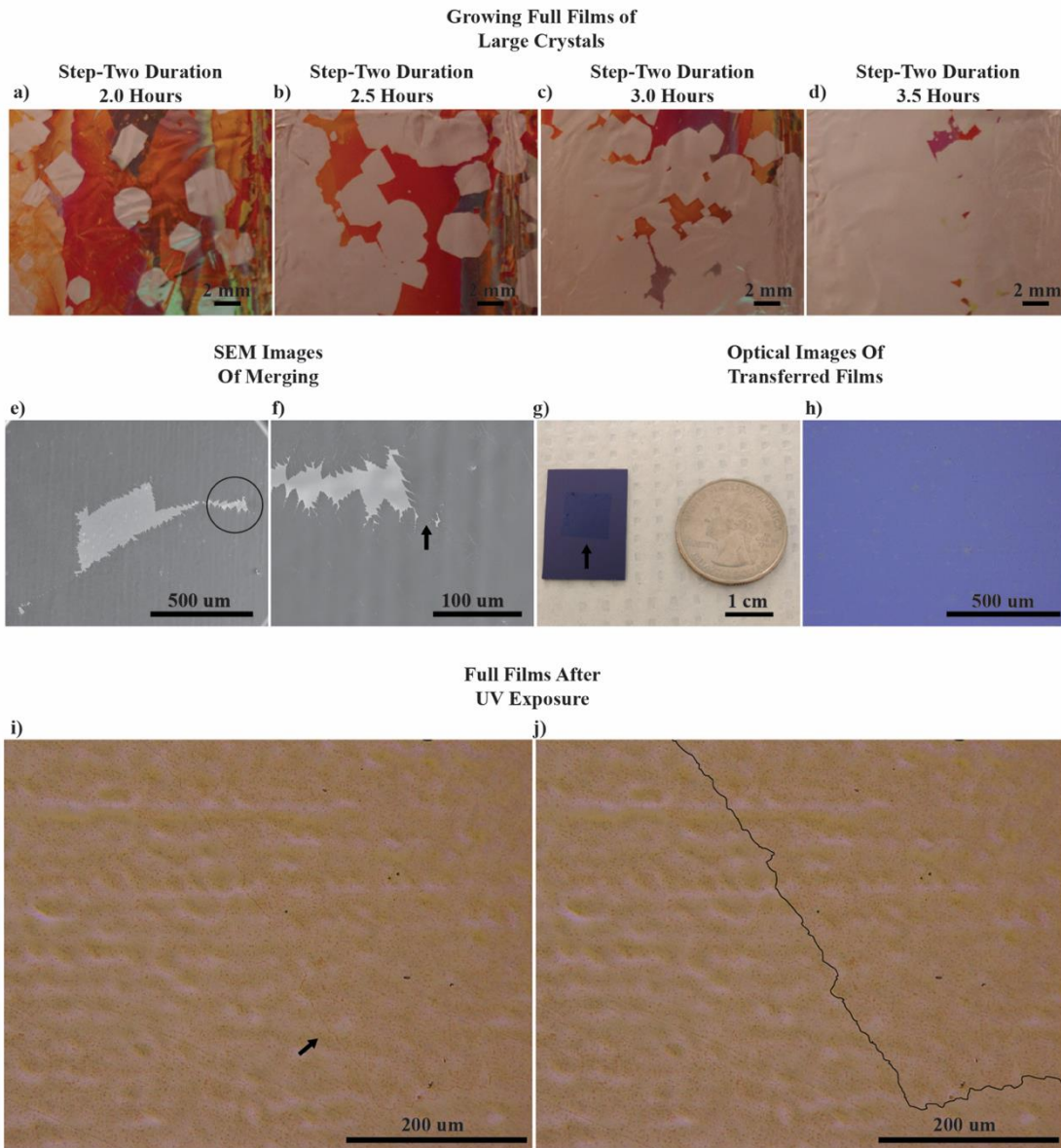
Figure 2.21: a-d) optical images of graphene on copper foil following two-step growth ranging from 4.5 – 6.0 hours of total growth. As the growth duration proceeds, the large graphene domains start to merge and form a film. **e-f)** SEM images of an area before full merging **g-h)** optical images of continuous films transferred onto a rigid substrate **i-j)** optical images of graphene on copper following UV exposure to observe large-domain grain boundaries

Altogether, by simultaneously controlling nucleation density and edge-growth, the synthesized graphene demonstrated here highlights the versatility, in terms of domain-size, growth duration, and continuous surface coverage, of the developed growth protocol.
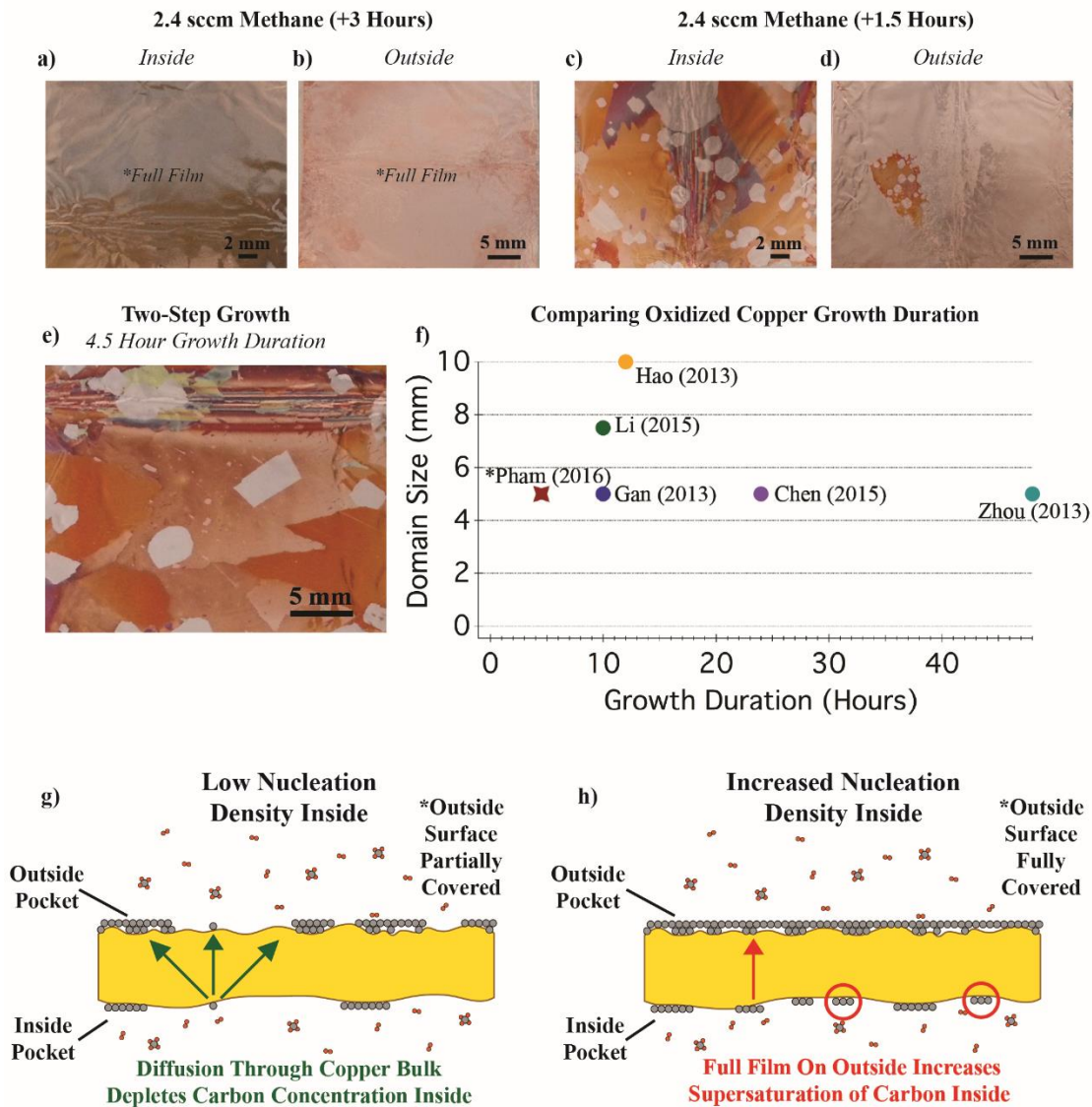
Figure 2.22: a-b) Optical images of inside and outside of copper pockets following copper oxidation after two-step growth. After full films cover the outside surface, growth inside produces merged domains/films. c-d) Full film coverage on the outside surface is avoided by reducing the growth time to 1.5 hours for step-two using 2.4 sccm. We observe preservation of low nucleation density inside after decreasing growth duration. e) Optical image of inside of copper pockets following copper oxidation after optimized two-step growth resulting in isolated 5-mm graphene domains. f) Comparing other oxidized copper growth durations (one-step) compared to our two-step growth. g-h) Cartoon depicting the influence on the diffusion of carbon and the inside nucleation density, before and after the formation of full films on the outside surface. After formation of a full film on the outside surface, the nucleation density inside, increases.

In order to postulate how the formation of a full film on the outside surface influences the nucleation density on the inside surface, we must consider the

conditions whence nucleation occurs. Verified both by observations in our two-step studies, and in the literature, growth inside enclosed copper pockets has the characteristic trend of low nucleation density inside, resulting in larger domains on the inside surface than the outside surface[6,45,47,51]. Nucleation, in addition to edge-attachment, and ad-layer growth, results from the diffusion of carbon species on the copper surface[52,53,63–73]. The formation of large carbon chains and clusters responsible for graphene nucleation[70–73] occurs when the concentration of carbon species on the surface, $C_{Surface}$, is much higher compared to the equilibrium concentration ($C_{Nucleation} \approx 2C_{Equilibrum}$)[52,66]. On the other hand, if the level of carbon species is between the nucleation and equilibrium concentrations ($C_{Nucleation} > C_{Surface} > C_{Equilibrum}$), edge-growth of graphene can occur[52,66,68–72].

Our results suggest that, during step-one where we use a low methane flow rate, the concentration of carbon species on both surfaces remains close to the equilibrium concentration ($C_{Surface} \geq C_{Equilibrum}$), thus, in order to cause supersaturated nucleation, long growth durations (3 hours) are required. As soon as nucleation occurs, the amount of supersaturated carbon species quickly depletes[52]; hence, the low nucleation density on the inside surface[52,66]. This assumption is further supported by the nearly bare, outside surface. During step-two, when the methane flow rate is increased, we observe a dramatic increase of domain-size on the inside surface, with negligible increase in nucleation density. This suggests that the carbon concentration on the inside surface still remains in the sensitive region between equilibrium and nucleation, ($C_{Nucleation} > C_{Inside} > C_{Equilibrum}$)[52,66]. The increasing coverage on the outside surface (for increasing methane flow rate) also

agrees with a rise in the carbon concentration. It is observed that new nucleation sites on the inside surface do arise, but overall, since we are able to yield isolated domains, nucleation does not dominate, and indicates that the carbon concentration level remains close to, or below the nucleation threshold. Finally, after a full film is grown on the outside surface, indicating that the carbon concentration has remained above the equilibrium level over long durations[52], we observe increased growth on the inside surface, which results in the formation of merged domains.

From our experiments adjusting growth duration to compensate for the elevated methane flow rates, we observed that full film coverage on the outside surface acts as a convenient, observable threshold where nucleation inside remains low, such that isolated domains are synthesized. This suggests that, on the inside surface, before the formation of a full film, the concentration of carbon species is still relatively close to the nucleation threshold, ($C_{Surface} \leq C_{Nucleation}$); subsequently, after the formation of a full graphene film on the outside, we observe an increase in nucleation density on the inside, suggesting the carbon concentration on the inside increases, up to the nucleation threshold[52,66]. The tuning of growth duration would hence not be effective in limiting nucleation on the inside if the concentration of carbon species were well above the nucleation threshold before the formation of a full film on the outside, as would be in the case of extremely high methane flow rates. This regime is where previous two-step studies have typically operated[26], and we confirm these results in (Fig. 2.20e-h). Nonetheless, for our control experiments avoiding formation of full film coverage on the outside surface to limit the nucleation density inside, before formation of a full film on the outside surface, we

believe that the carbon concentration inside is still within the sensitive range between growth and nucleation. Thus, it is plausible that the formation of a full film on the outside, could affect the concentration of surface carbon species on the inside to a large enough degree, such that, distinct changes in the nucleation rate occur. We speculate that the ability to operate in such a sensitive carbon concentration range is only enabled by the unique effects of oxidized copper growth, which are utilized during the two-step synthesis.

Although the growth pathways for CVD graphene synthesis have been widely studied both experimentally and theoretically[26,50,52,63–74], the exact evolution of graphene growth is still not fully developed, especially for oxidized copper growths[6,23,46,53]. Recently, it has been revealed that the presence of surface oxygen species not only limits the nucleation density[6,23,46], but also plays a crucial role in decreasing the edge-attachment barrier for domain growth[6], and imperative to our studies using copper pockets, enables the diffusion of carbon monomers through the copper bulk[53]. While the control of the nucleation density via passivation of active nucleation sites has been exploited in other studies growing large-domain graphene[6,23,24,46,51], the use of elevated methane flow rates in our studies directly utilizes the decreased edge-attachment barrier for domain growth. When using elevated methane flow rates for two-step growth, due to the decreased edge-attachment barrier, we expect that the surface carbon species can easily be incorporated into existing domains to contribute to edge growth[6]. This is supported by the fact that we see an increase in domain-size for increased methane flow rate. We observe this oxygen assisted edge-growth, despite the presence of hydrogen gas

flow, which can act as a growth inhibitor[68,69]. Furthermore, with an increase in methane flow rate, we observe a variety of isolated, domain morphologies, instead of compact hexagons, which further supports utilization of an oxygen aided, decreased edge-attachment barrier and diffusion limited growth[6], and suggest the observed domain morphologies are not directly dictated by substrate aligned growth[73,74]. This aspect of our method is dually advantageous, since carbon species that are incorporated into existing domains can quickly deplete the overall concentration of surface carbon species, preventing further nucleation[6,52,66,69]. In addition, metal step-edges, which often act as sites for nucleation, do not effectively trap carbon monomers[71]; therefore, the complete dehydrogenation of CH_4 to carbon monomers from oxygen species[6] could play a role in decreasing the nucleation density. For these reasons, a two-step growth on oxidized copper is ideal for limiting the nucleation density, since existing domains from step-one can easily incorporate and deplete the surface carbon species during step-two, resulting in a lower nucleation density compared to a one-step growth of equivalent methane flow rate and growth duration (Fig. 2.14e-f).

Due to the fact that our two-step method utilizes oxidized copper growth, which results in the full dehydrogenation of methane to readily yield carbon monomers, diffusion of carbon through the copper bulk is expected to occur[53,69]; this could be the underlying mechanism controlling increases in the nucleation density on the inside, after a full film covers the outside surface. Even before full film coverage, we observe areas of adlayer graphene growth on the outside surface of the copper pocket for all methane flow rates (Fig. 2.23).
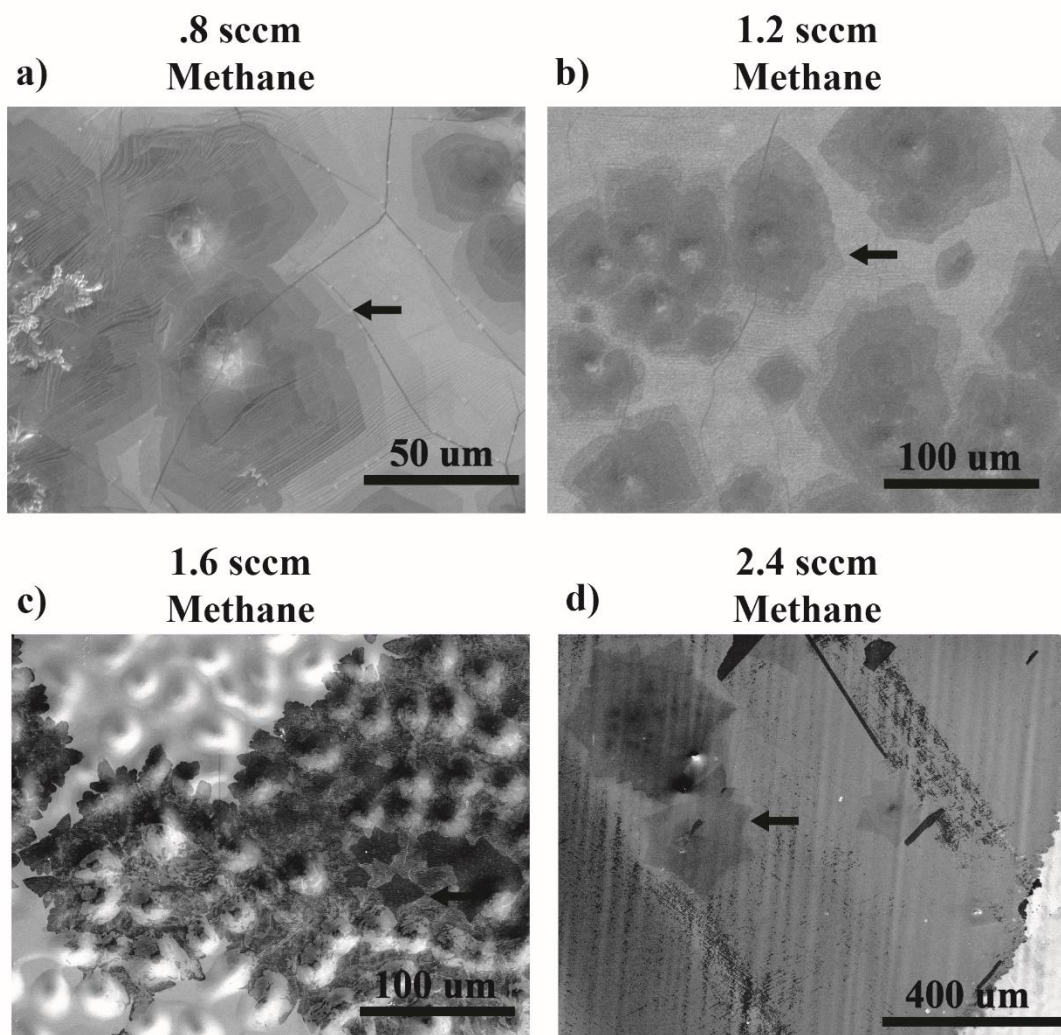
Figure 2.23: SEM images of the outside of the copper pocket following two-step growth (using 0.4 sccm methane for step-one) for various methane flow rates. Adlayer growth is observed for all two-step growths. Our results suggest that the adlayer growth outside and the large-domain growth inside are closely related.

Since adlayer growth on the outside surface results from the diffusion of carbon monomers originating from the inside surface[53,67], our observations suggest that during the two-step process, diffusion through the copper bulk occurs without the need for full film coverage. These results are markedly different compared to previous experiments where the formation of adlayer graphene only takes place after a full film forms on the outside surface[53,67]. Although the diffusion of carbon

through the copper bulk before full film conditions (on the outside surface) has not been established, the evidence suggests that the diffusion rates could depend on a number of factors on both surfaces, including the nucleation density, exposed copper surface areas, adlayer nucleation density, and concentration of surface oxides[53,67–69], but the optimization of these parameters is beyond the scope of this paper. However, our observations of distinct variations (in domain size and coverage) in adlayer growth on the outside surface (Fig. 2.23) indicate that the diffusion of carbon, feeding adlayer growth on the outside can be altered upon changes in the methane flow rate; thus it is reasonable to speculate that the real time diffusion of carbon species through the copper bulk can influence the local carbon concentration on the inside surface during growth.

One possible explanation of why the nucleation density remains low on the inside surface before full film conditions during two-step growth is that the diffusion of carbon through the copper bulk can "store" excess carbon as adlayer growth where metal defects or impurities exists[69,71]. Increases in the carbon concentration on the inside surface during two-step growth could thus drive the diffusion rate through the copper bulk[53]. This allows the local carbon concentration on the inside to remain below the nucleation threshold as carbon species are depleted from the inside surface (Fig. 2.22g). After the formation of a full film, we observe an increase in the nucleation density on the inside surface (implying an increase of the local carbon concentration) (Fig. 2.22h). We have not confirmed where the increase of the carbon concentration arises from, but consider that a decrease of carbon diffusion through the copper bulk could result as a consequence

of a decreased concentration gradient as adlayer coverage increases on the outside surface[53]. This hypothesis that the diffusion rate through the bulk is determined by full film conditions (such as nucleation density, copper surface coverage) is consistent with previous studies demonstrating a correlation of the inside nucleation density to adlayer coverage on the outside surface[67]. Further investigation on the diffusion mechanism during two-step growth could foster development of new methods to severely suppress nucleation on the inside surface, and improve bilayer synthesis on the outside surface.

The methods and techniques developed here, simultaneously controlling nucleation density and edge growth, should be adapted to other graphene growth substrates to further extend current single-domain size limits and rates. The fast two-step growth protocol for growing large single-domain graphene can be easily modified to other metallic growth substrates, where graphene nucleation and edge growth can be separated into two steps, including but not limited to platinum, ruthenium, iridium, and palladium[75–77]. The increased catalytic activity for CH_4 and H_2 dissociation on platinum for example[75], could provide additional means for accelerating the growth rates of graphene single-domains when used in combination with a two-step protocol. Additionally, the two-step growth method could realize the synthesis of large-domain graphene from the seamless stitching of aligned graphene nucleation centers[73].

Methods to limit the nucleation density and growth rate by controlling the carbon diffusion through the bulk, as investigated in this work, could be further examined using metals such as nickel[78], where the increased carbon solubility, and

carbon segregation growth mechanism could provide an obvious means to regulating the local carbon concentration, and hence, large-domain graphene growth. Methods using nickel and ruthenium substrates under controlled carbon segregation conditions have already demonstrated utility for growing mm-scale monolayer domains[79,80]; combined with the techniques developed here on copper, it is reasonable to anticipate metals such as these (as alloys, layered stacks, or pure metals) as appropriate growth substrates for synthesis of wafer-scale single-domain monolayer graphene or large-domain bernal stacked graphene.

We have demonstrated a simple method for fast synthesis of mm-domain-size graphene using a two-step oxidized copper growth inside copper pockets. The two-step approach, which is supported from oxidative-assisted mechanisms to control nucleation, promote edge growth, and drive carbon diffusion through the copper bulk, exploits the low nucleation density using low methane flow rates, which are then enlarged using increased methane flow rates. We find that the outside surface of the copper pocket acts as an observable threshold where the nucleation density remains low inside. Thus, we can easily tune the first and second stage durations and methane flow rates according to the coverage on the outside copper surface to obtain isolated, large-domain graphene. Applying this method, we show that 5-mm single-domains can be synthesized in 4.5 hours of growth. A host of characterization techniques were employed to confirm that the synthesized graphene is monolayer and single-domain. Our studies focused on optimizing growth conditions can be adapted to most existing CVD systems, and will promote

the development of synthesizing wafer-scale single-domain graphene, which will further stimulate advances in graphene integration and applications.

Chapter 3 – Graphene Electrical Tuning and Transfer

3.1 Standard Wet Transfer

The standard transfer technique starts with CVD graphene on copper[7,29]. PMMA is spun onto the sample, and cured overnight. Following oxygen plasma removal of backside graphene, the copper foil is then etched in ammonium persulfate solution. The floating PMMA/graphene stack is then washed (in DI water, and often times RCA 1 and 2 solutions to remove residual metal[81]), and can then be wet transferred onto a target substrate. After drying the sample, PMMA is removed by acetone and then annealed in low-pressure hydrogen environment.

One obvious advantage of using transferred CVD graphene is that the fabricated devices can easily be on the cm-scale, which is necessary for graphene-THz devices. The drawback is that the transfer process modifies the electrical quality of graphene films, usually from contamination, and defects from wrinkles and tears. This issue is further exacerbated when the device dimensions are on the cm-scale, since nano/microscale defects and variations could easily be masked if the device is also on the nano/microscale. Fig. 3.1 shows the depletion curve (Ids v Vg) for a typical 1 x 1 cm device on SiO_2 using acetone wash and annealing to remove PMMA.
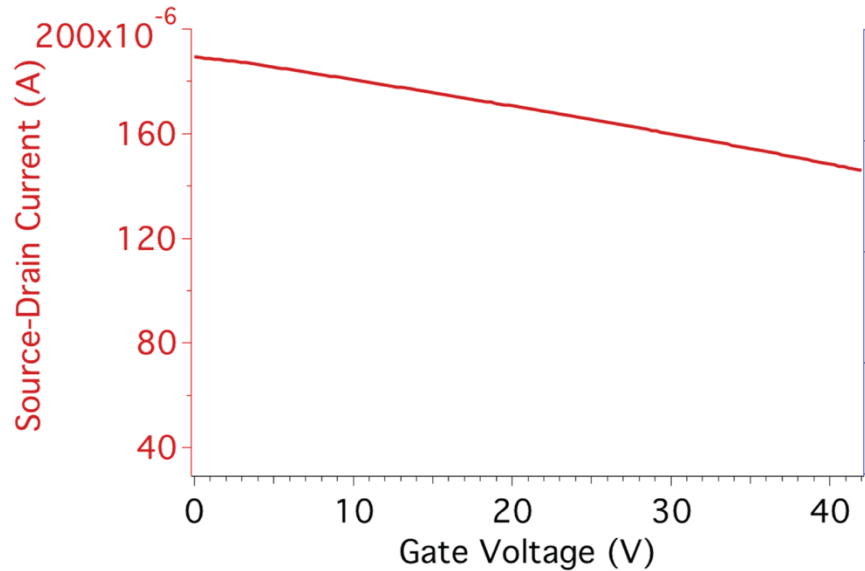
Figure 3.1: Source-drain current vs gate voltage for a GFET device using standard PMMA wet transfer with vacuum annealing step. The flat behavior indicates strong substrate interaction which pushes the Dirac point to > 100 V.

The results indicate high p-type doping from substrate interactions; the device only changes by 30 uA for a 40 volt change in the gate, and the Dirac point is estimated to > 80 V. From the electrical data, it is clear that the large-area graphene films are inferior to the electrical quality of mechanically exfoliated graphene (with a source-drain current that can easily be altered by a back gate). If we aim to have a\ high on/off ratio device (easily changes Ids for small Vg range) with low sheet resistance for graphene-THz devices, we must improve the large-area graphene transfer techniques.

3.2 ODTS Modification

Literature has demonstrated that the use of self-assembled monolayers (SAM) can provide a means to decrease substrate interactions with graphene[58,82,83]. Validation of decreased substrate effect has conducted on micron scale GFETs, and thus, we employ the technique for our mm scale device. Briefly, the SiO2 substrate is

cleaned in piranha solution, which creates a large number of OH- groups on the SiO2 surface. The substrate (which at this time is hydrophilic from OH groups), is washed and dried, and then placed into anhydrous toluene. ODTS is then dropped into the toluene for reaction at a 1 ul/ml concentration for one hour. Following cleaning and drying, the substrate is observed to be hydrophobic from the methyl terminated ODTS SAM. We also performed vapor deposition of SAMs on the wafer following piranha clean, where a vacuum desiccator is evacuated with a vial containing 50 uL of the SAM solution.

Graphene is then wet transferred onto ODTS SAM modified substrates using the standard technique. Two differences should be noted; PMMA is removed only with acetone since annealing under low-pressure hydrogen is found to be detrimental to the GFET on ODTS SAM. Another downside of using the SAM modified substrate is that water becomes trapped under graphene (due to the large contact angle of water on ODTS SAM) that results in large-scale wrinkles after the graphene film is dried. Fig. 3.2 shows a typical depletion curve for devices transferred onto ODTS SAMs.
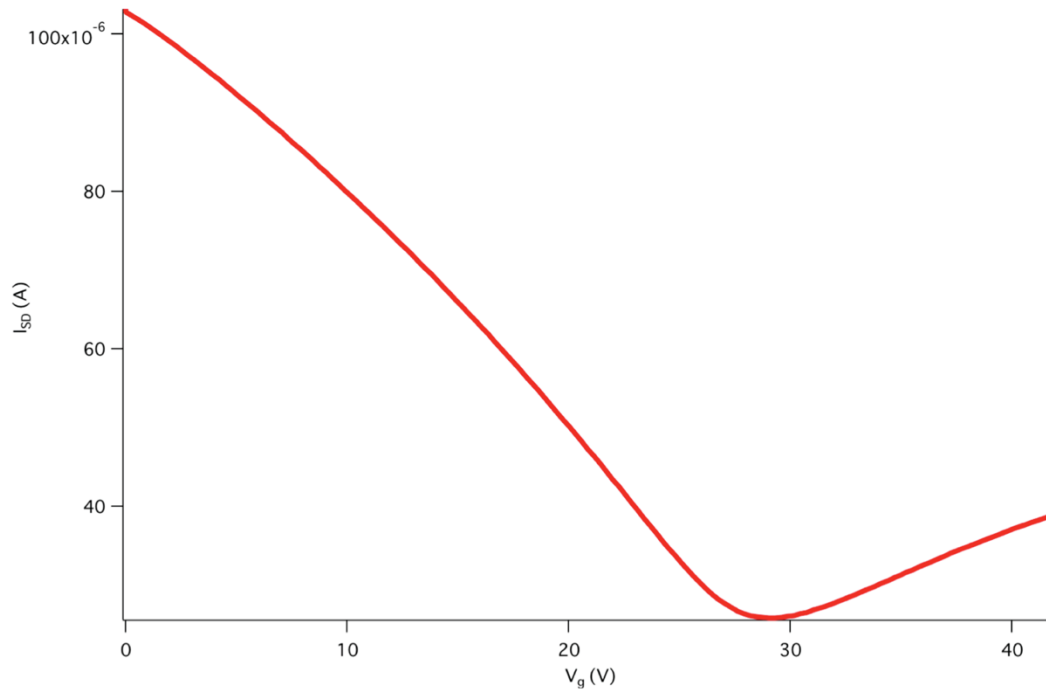
Figure 3.2: Source-drain current vs gate voltage for a GFET transferred using PMMA wet transfer onto a ODTS functionalized wafer. The Dirac point is clearly observed ~29 V, and the transconductance is dramatically increased.

The Dirac point (point of minimum conductance) is clearly observed ~35 V, suggesting decrease in substrate interaction. The lowering of the Dirac point (from > 80 V to ~ 35 V) also results in an increase in on/off ratio (from ~1.1 to > 4). Additionally, leakage current is observed to dramatically decrease from typically [10^-6] without SAMs to [10^-8] with ODTS SAMs (the number of leaky devices also greatly decreases). With a high on/off ratio device, the ODTS SAM modified GFETs should perform better as a THz modulator than those without SAMs; enabling greater depth of modulation. Although the SAM modification does create advantages for THz modulators, using PMMA transfer onto ODTS SAMs achieves a minimum sheet resistance of ~800 $\Omega/\square$, which is 2 times greater than our goal of 377 $\Omega/\square$.

3.3 Controlling Doping

Aiming to reach 377 $\Omega/\square$ we explore intentional doping of GFETs. PMMA transfer does result in p-doping of the GFETs, so our devices are inherently already p-doped. Thus, it could be helpful to further dope GFETs using additional acceptors. Typically, for higher doped graphene, the on/off ratio will be decreased as a tradeoff. We investigate doping our large-scale GFETS with benzimidazole (BI), following the process by S.J Kim et al[84]. Briefly, BI (a metal-chelating agent) is mixed into a dilute etching solution that is composed of a combination of sulfuric acid, hydrogen peroxide, and ammonium persulfate. Fig. 3.3 shows the depletion curve for a GFET after wet transfer using BI doping.
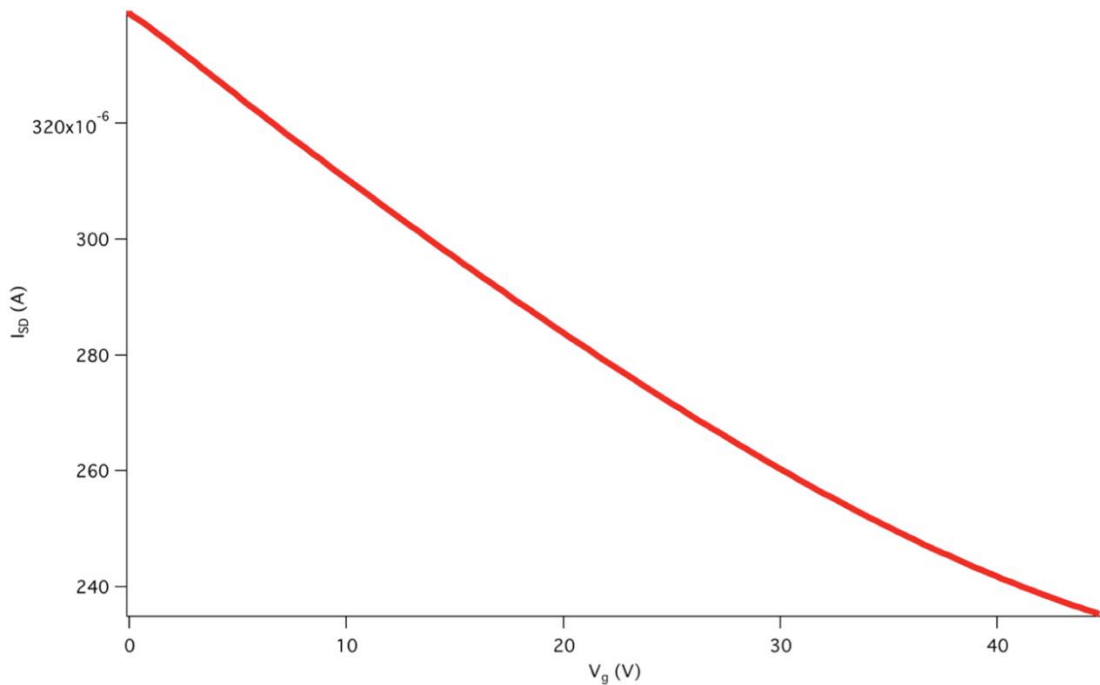
Figure 3.3: Source-drain current vs gate voltage for a GFET doped with benzimidazole during of etching of copper. The Dirac point is pushed passed 45 V, which is out of the range that can be applied to the ODTS SAM.

Doping using BI appears to further p-dope the GFET, indicted by no observable Dirac point below 45 V (after 45 volts on the back gate, ODTS starts to break down

and leak), and a decrease on/off ratio. The voltage on the source-drain is 0.1 V, giving us a DC resistance value of 303 Ω. We perform van der pauw, 4-point measurements, and measure the lowest value of 250 Ω/□.

We obtain sheet resistance values below 377 Ω/□ only by using intentional doping. Although the devices do exhibit slight changes in source-drain current as we vary gate voltage, the desired mobility and on/off ratios probably cannot be met with simple doping. If we are to demonstrate ideal graphene-THz modulation (1 – 99% depth of modulation by back gating), it is essential that we find a method to transfer graphene without defects, and contamination, in hopes of preserving the high on/off ratios and low sheet resistance.

3.4 Direct Transfer

We also performed experiments on polymer free transfer of graphene. Most transfer techniques call for the use of some sort of sacrificial layer (PMMA, PDMS, polymer, metal) and usually results in doping and additional scattering; we have developed a novel, direct-transfer method. Briefly, a graphene on copper sample is taped directly, face-to-face on an ODTS wafer. By placing the wafer and copper into a copper etching solution, the copper becomes etched, and the graphene adheres to the hydrophobic wafer. We investigated how to optimize transfer using different chemical functionalization of the substrate, high-pressure etching, and differing etching solutions. The most promising result was by increasing the fluid pressure. Fig. 3.4 shows the influence of the height (and thus fluid pressure) of the etching solution.
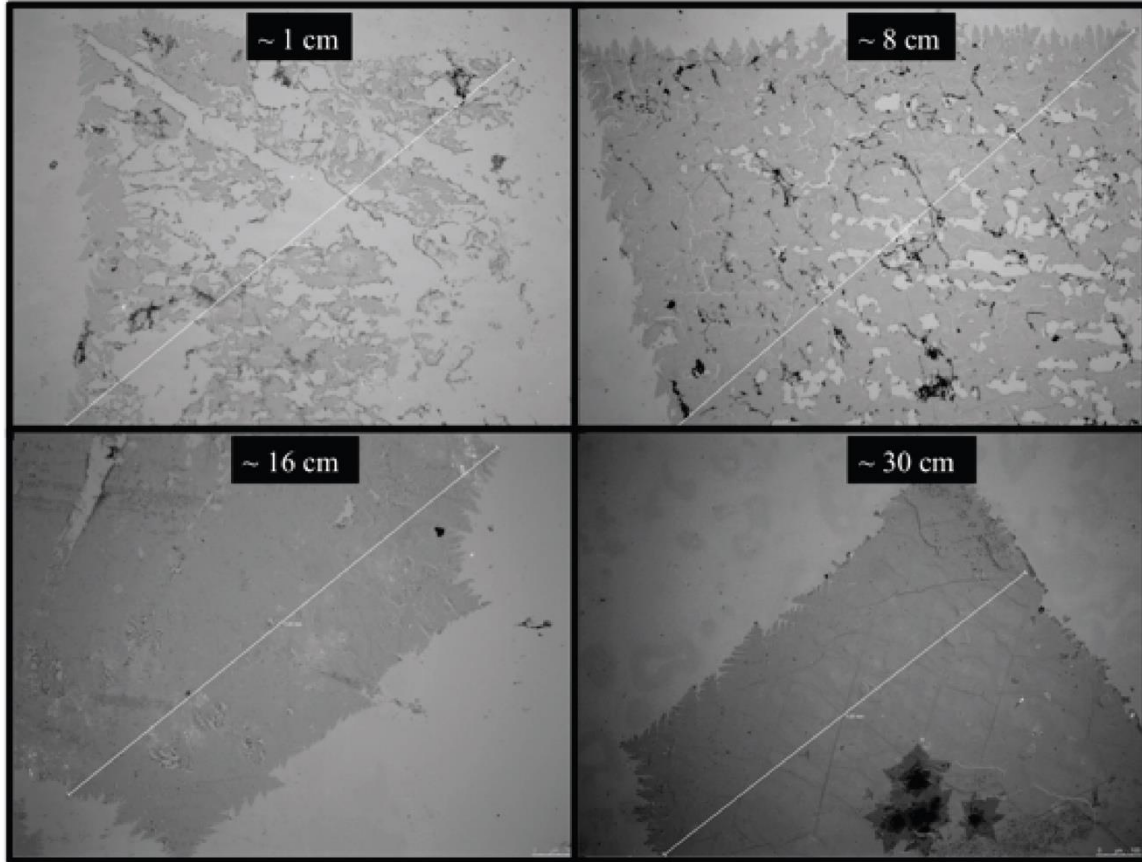
Figure 3.4: Novel direct transfer using ODTS substrate. We notice an increase in transferred surface area % as we increase the height (and thus fluid pressure) of the etching solution from 1 - 30 cm.

We speculate that the increase in pressure correlates to the percentage of the surface area that is successfully transferred. Although we have demonstrated the proof of concept of a completely sacrificial-layer-free, direct transfer, in a novel technique, the method is still far from adequate in terms of device properties. Upon electrical investigation, the electrical properties indicate high p-type doping, and diode like properties. Furthermore, the DC sheet resistance is measured to be 1000 Ω. The electronic properties could possibly be improved by differing etching, or by performing a series of surface cleaning techniques such as annealing and RCA cleansing. By using the full spectrum of cleaning techniques, a direct transfer

method could possibly enable fabrication of a highly sensitive GFET with low sheet resistance.

3.5 Bubble Removal Transfer

Bubbles generated during electro-delamination and chemical etch during large-area two-dimensional (2D) material transfer has been shown to cause rippling, and consequently, results in tears and wrinkles in the transferred film. We demonstrate a scalable and reusable method to remove surface adhered micro-bubbles by using hydrophobic surfaces modified by self-assembled monolayers (SAM). Bubble removal allows the 2D film to flatten out, and prevents the formation of defects. Electrical characterization was used to verify improved transfer quality, and was confirmed by increased field-effect mobility and decreased sheet resistance. Raman spectroscopy was also used to validate improved electrical quality following transfer. The bubble removal method can be applied to an assortment of 2D materials using diverse hydrophobic SAM variants. Our studies can be integrated into large scale applications, and will lead to improved large-area 2D electronics in general.

Chemical vapor deposition (CVD) has enabled the synthesis of large-area two-dimensional (2D) materials including graphene[4,85,86], transition metal dichalcogenides[87,88], and hexagonal boron nitride[89]. In order to fabricate practical devices, the synthesized materials often require various wet-transfer processes which rely on removing the CVD-grown material from the growth substrate[90,91], usually by chemical etching[7] or electro-delamination[41,92]. During these steps, the formation of bubbles between the 2D material and etch/delamination solution lead

to rippling and detrimental defects[90,93], and hence, developed processes have specifically aimed to minimize bubble formation by using low concentration of etchant[81], or low voltages during delamination[41,94]. Although the formation of bubbles has generally been circumvented, no such method of removing bubbles that adhere on the 2D material/solution interface has been reported. Here, we report a scalable method at removing micro-bubbles on the surface of CVD graphene by using hydrophobic surfaces modified by self-assembled monolayers (SAM), which allows the graphene film to flatten before transfer to a substrate, which significantly improves the large-area electrical performance of devices. The enhanced electrical properties are shown to arise from decreased tears and wrinkles produced from trapped bubbles. The bubble removal method can be adapted to wafer-scale processing, and will lead to defect-free 2D electrical devices with uniform device performance across large-areas.

During transfer, because it is unfavorable for bubbles to be in contact with water[95], bubbles generated in solution prefer to adhere to the hydrophobic graphene surface[96]. One means to remove these bubbles is by a "dry transfer" method, completely removing the graphene from solution by using exclusively designed rigid supports such as thermal release tape or pressure sensitive polymers[5,97,98]. Instead, we investigated a simple "wet transfer" method that can be easily implemented using counter-adhesion from a hydrophobic surface. The hydrophobic surface that is used is a vapor deposited SAM of 1H,1H,2H,2H-perfluorodecyltrichlorosilane (FDTS) on a silicon-oxide (SiO_2) layer on silicon (Si).

Following SAM functionalization, the surface becomes hydrophobic (Fig. 3.5), and can be used for bubble removal during graphene transfer.

To grow large-domain monolayer graphene on copper foils, we use an oxygen-assisted CVD process with two-stages of methane flow rate to first, decrease the nucleation density, and then, promote edge-growth until a full film forms[99]. Following graphene synthesis, the graphene films can be "wet transferred" following standard protocol using a poly (methyl methacrylate) (PMMA) support layer. The graphene/PMMA stack is then removed from the copper foil growth substrate using an electro-delamination process in NaOH solution, where the copper/graphene/PMMA is used as the cathode, and a carbon rod is used as the anode. Previously, researchers have used a small voltage between the cathode and anode in order to deliberately avoid the generation of bubbles on the graphene surface[41]. Instead, as the main purpose of this work, the generation of bubbles is not avoided (as the bubbles will be removed using the hydrophobic SAM wafer), and the voltage used to delaminate does not need to be delicately tuned. The bubble removal process is illustrated in Fig. 3.6 and described below.

The process begins after the graphene/PMMA stack is delaminated from the copper foil where bubbles generated on the graphene surface cause rippling, Fig. 3.6a. The floating graphene/PMMA stack is then moved to a clean deionized (DI) water bath, as per standard transfer process. While in DI water, the graphene/PMMA film is brought into contact with the hydrophobic SAM wafer by "scooping", Fig. 3.6b. The bubbles act as a capillary bridge between the substrate and the graphene film[95], which prevents irreversible adhesion to the wafer that would damage the graphene film[39]. By submerging the wafer into DI water, the graphene film is subsequently released from the hydrophobic wafer, though the bubbles stay adhered to the hydrophobic substrate. This allows the bubble-free graphene film to flatten out on the surface of the DI water, Fig. 3.6c.
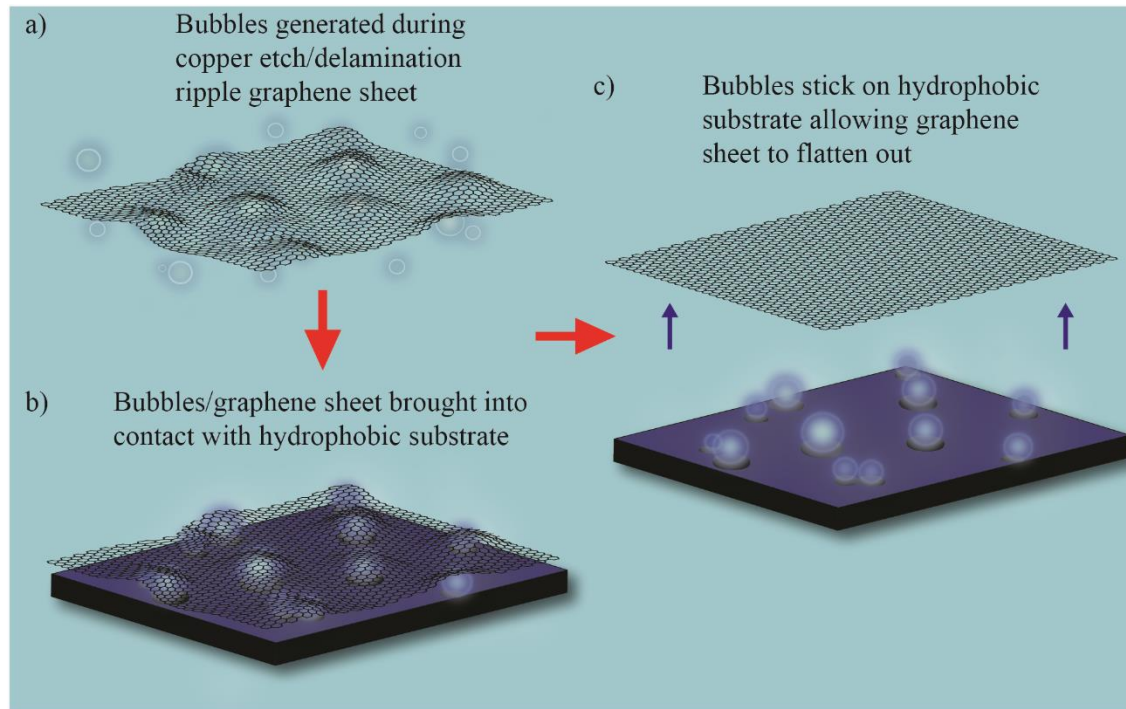
Figure 3.6: a) Bubbles are generated in solution during the etch/delamination step when CVD grown graphene is removed from the growth substrate (copper foil). Bubbles stick to the bottom side (in contact with solution) of the floating graphene film. b) The graphene film with bubbles on the bottom side is brought into contact with a SAM modified SiO2 chip. c) The hydrophobic bubbles adhere to the hydrophobic SiO2 surface, which removes the bubbles from the graphene surface, and allows the floating graphene film to flatten out.

Fig. 3.7a-d contains optical images of bubble removal from an actual graphene film. Fig. 3.7a shows a floating graphene/PMMA film with bubbles on the bottom clearly evident. A yellow dotted line was added to help identify the boundary of the film. In Fig. 3.7b, the graphene/PMMA film is "scooped" from DI water using the hydrophobic modified substrate, with half of the film still floating in DI water, while the other half is "pinned" to the substrate. After the film makes full contact with the hydrophobic substrate, the substrate is immersed back into DI water to release the film, allowing the graphene to float to the surface of DI water. Even as the graphene/PMMA film floats away, the square imprint of the bubbles is

apparent on the hydrophobic substrate, highlighted by the red arrow in Fig. 3.7c. Upon exposing the hydrophobic substrate to air, the bubbles can be simply popped, and hence, the substrate can be readily reused for further bubble removal from the graphene film. The procedure is repeated three more times, each time rotating the graphene film by 90 degrees in order to fully remove all bubbles from the graphene surface. Fig. 3.7d shows the floating graphene/PMMA film with all bubbles removed, ready for transfer to the desired target substrate.
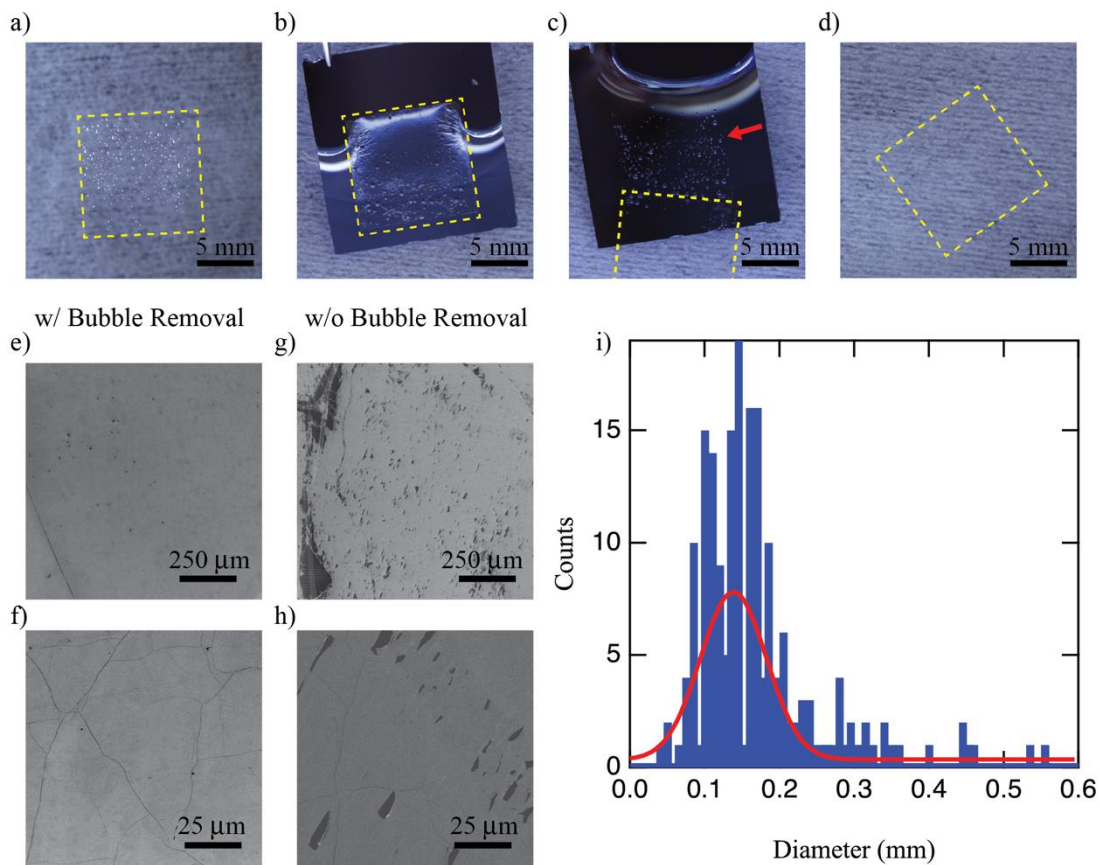
Figure 3.7: a) Floating graphene film (covered with PMMA) contains bubbles on the bottom surface generated during electro-delamination. A yellow dotted line is provided to help identify the boundaries of the floating graphene/PMMA film. b) The graphene/PMMA stack is brought into contact with the hydrophobic SAM modified SiO2 chip by "scooping". c) By submerging the hydrophobic SAM modified wafer beneath water, the graphene/PMMA is released to float on the water surface, while the bubbles remain on the hydrophobic SAM modified chip. A red arrow points to bubbles that remain on the SAM modified chip. d) A bubble-free graphene film floats on the surface of water, and is ready to be transferred to the desired target substrate. e-f) SEM images of a graphene film transferred to a oxide-on-silicon chip following bubble removal. g-h) SEM images of a graphene film transferred to an oxide-on-silicon chip without bubble removal. Without removing the bubbles on the bottom side of the graphene film, bubbles become trapped between the graphene film and target substrate, resulting in detrimental tears in the graphene film after drying. i) Histogram of the diameter of bubbles on the graphene surface generated during electro-delamination. The diameter distribution was analyzed with a Gaussian fit, with a value centered at ~ 140 um.

Fig. 3.7e-f comprises of scanning electron microscopy (SEM) images of transferred

graphene films (with the PMMA support layer removed) after utilizing the bubble

removal process. To compare, Fig. 3.7g-h, shows SEM images of transferred

graphene films without the bubble removal process. In both cases, wrinkles typical to CVD grown graphene, which are generated upon cooling due the difference of thermal expansion of graphene and the copper growth substrate[4], are observed. Notably, without the bubble removal process, the SEM images in Fig. 3.7g-h includes a large number of tears in the graphene film, not present when the bubble removal process is used. These images show that the flattening of the graphene film before transfer prevents the formation of tears produced by trapped bubbles[93]. Furthermore, Fig. 3.8 contains optical photographs of transfers with and without bubble removal.
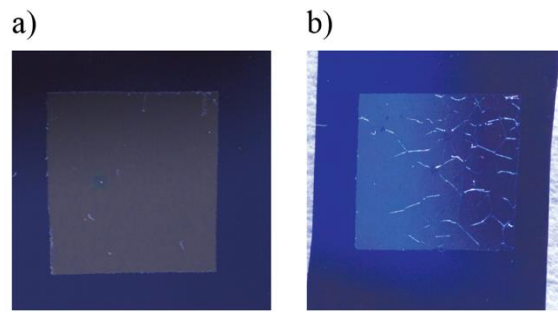
Figure 3.8: a) Graphene with PMMA film transferred onto target substrate with bubble removal processs. b) Graphene with PMMA film transferred onto target substrate without bubble removal process. Trapped bubbles between graphene and the target substrate cause large wrinkles and tears in the transferred film after drying.

Large-scale wrinkles in the graphene film, caused by the trapping of bubbles between the graphene film and target substrate film (not from the CVD cooling process), are clearly evident in the case when bubbles are not removed.

Using the optical image in Fig. 3.7a, we estimate the size of bubbles removed using image analysis software. The bubble diameter distribution is plotted in Fig. 3.7i, and a Gaussian fit yields a diameter centered at ~ *140* um, although a tail of large bubbles is present, with ~ 23% of bubbles > 0.20 mm (the 1σ threshold).

However, nanoscale tears in Fig. 3.7h suggest that nanoscale bubbles that exist on the graphene surface are removed with the bubble removal process, but we have not confirmed this with nano-imaging. Nonetheless, the removal of micro-scale to mm-scale bubbles effectively decreases micro-scale to mm-scale tears and wrinkles in the graphene film.

In order to investigate the effects of removing micro-scale to mm-scale bubbles on the graphene device performance, we perform a variety of large-area (mm-scale) characterization. The large-area measurements allow us to probe collective device behavior that, elsewise, could be undetectable at micro-scale dimensions. Following transfer to an oxide on Si wafer (and PMMA removal), we deposit chromium/gold contacts to probe the graphene electrical properties. Fig. 3.9a shows the large-area source-drain current versus gate voltage of devices of dimensions $\sim$ 7 x 4.5 mm with and without prior bubble removal. Although the charge neutral point voltage (V_{CNP}) is nearly identical for both cases, removing bubbles from the graphene surface results in increased large-area field-effect mobility compared to when bubbles are not removed, as evident in the depletion curve data. We define the on/off ratio as ratio of the current at 0 V_g to the current at V_{CNP}; the on/off ratio is $\sim$ 10 (2x larger than when bubble removal is not used), consistent with increased mobility, Table 1.

Device Number	With or Without Bubble Removal	Sheet Resistance (Ω/□)	Field-effect Mobility (cm²/Vs)	On/Off Ratio
1	With	1525	1.09E+03	5.11
2	With	770	8.41E+02	4.69
3	With	702	1.56E+03	3.81
4	With	844	1.82E+03	7.07
5	With	498	3.18E+03	8.37
6	With	521	3.15E+03	9.19
7	With	489	3.26E+03	10.3
8	With	541	2.71E+03	9.71
9	With	697	2.87E+03	8.3
10	With	466	2.88E+03	10.2
11	Without	1277	8.58E+02	4.86
12	Without	1305	7.15E+02	5.1
13	Without	1285	8.68E+02	6.15

Table 3.1: Electrical characterization of devices with and without bubble removal. The device sheet resistance, estimated field effect hole mobility, and on/off ratio are listed.

Using the equation, $\mu_{FE} = \frac{\partial I_{DS}}{\partial V_g} \frac{1}{V_{DS}} \frac{L}{W} \frac{1}{C_{ox}}$, where I_{DS} is the measured source-drain current, V_{DS} is the applied source-drain voltage, L is the device length, W is the device width, C_{ox} is the oxide capacitance, and V_g is the gate voltage applied, we calculate the large-area field-effect mobility[100]. The greatest field-effect hole mobility calculated for large-area devices is ∼ 3260 cm² V⁻¹ s⁻¹ (compared to ∼ 868 cm² V⁻¹ s⁻¹ without bubble removal).

We also measured the large-area (zero gate biased) sheet resistance to quantify the effects of removing bubbles before transfer. We used a shadow mask to deposit four contact electrodes separated by 5 mm in a square geometry to ensure that probed area is equivalent for each device. Table 1 lists the sheet resistance values for devices with and without bubble removal. For devices with and without bubble removal, the average sheet resistance is ∼ 705 Ω/□ and ∼ 1289 Ω/□, respectively. The lowest sheet resistance values obtained is ∼ 466 Ω/□ when

bubbles are removed, and $\sim 1277\ \Omega/\square$ when bubbles are not removed prior to device fabrication. The combination of increased large-area mobility and decreased large-area sheet resistance confirm that electrical quality of graphene devices is improved by the bubble removal process.
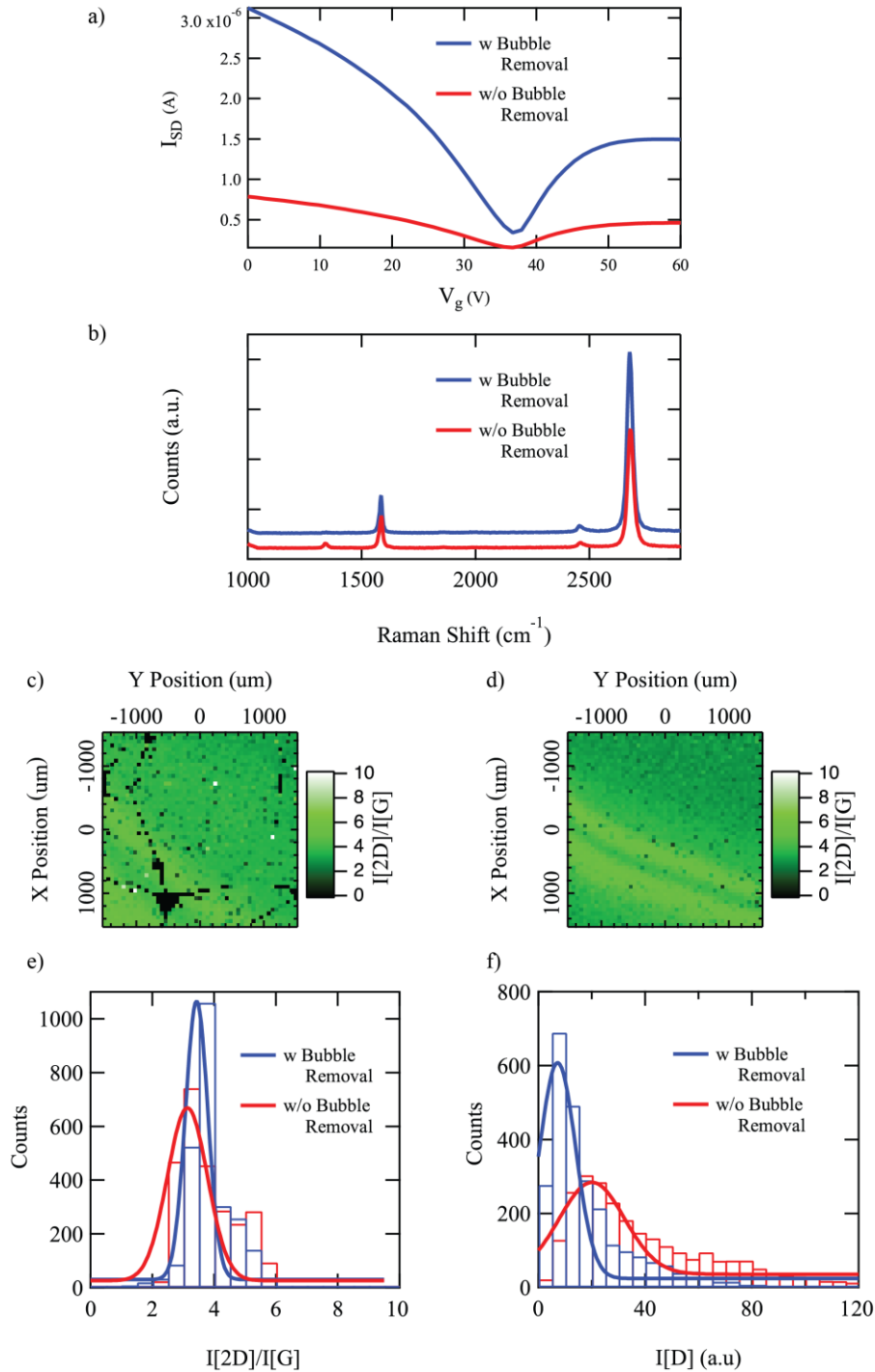
Figure 3.9: a) The source-drain current versus gate voltage is measured over large-areas (mm-scale) for devices with and without bubble removal. With bubble removal, the on/off ratio is increased to ~ 10. b) Representative Raman spectra of transferred graphene films with and without bubble removal. c-d) Raman mapping data of the I[2D]/I[G] for devices fabricated both without and with bubble removal. Cracks and tears in the graphene film from trapped bubbles during transfer are apparent. e) Histograms of the I[2D]/I[G] for graphene films with and without bubble removal. f) Histograms of the D peak intensity for graphene films with and without bubble removal

The improved electrical properties by bubble removal can also be supported using Raman Spectroscopy. The Raman spectra of monolayer graphene exhibits two distinct peaks called the G peak ($\sim$ 1583 cm^{-1}) and the 2D peak ($\sim$ 2680 cm^{-1})[43,61]. Another peak called the D peak ($\sim$ 1350 cm^{-1}), is often used to quantify defects[43,61]. For high quality graphene without defects, the ratio 2D:G peak intensities should be as large as possible (> 2 for monolayer graphene), and the D peak intensity should be as low as possible[43,61]. The representative Raman spectra of transferred samples with and without using bubble removal are shown in Fig. 3.9b. We performed Raman mapping to assess the graphene quality across large-areas. Presented in Fig 3.9c-d, are the Raman mapping images of the ratio of the intensities of the 2D:G peaks. The histograms of the 2D:G ratio for samples with and without bubble removal are shown in Fig. 3.9e. The histograms reveal the ratio of the 2D:G peak intensities is generally larger (Gaussian fit is larger amplitude, greater in center value, and sharper) when bubble removal is used, indicating a higher quality graphene than compared to when bubble removal is not used . Also clearly displayed in Raman mapping image Fig. 3.9c (when bubble removal is not utilized) are areas where the 2D:G peak intensity is approximately zero; these areas are undoubtedly where cracks and tears exist, and hence, do not exhibit the distinct graphene peaks. The cracks and tears can also effect the spatial variation of the D peak. The histograms of the D peak for samples with and without bubble removal are shown in Fig. 3.9f, and confirm that the sample without bubble removal exhibits more frequent and higher intensity D peak. The collective information presented

from the Raman mapping experiments confirm that the electrical quality of transferred graphene devices is significantly improved using bubble removal.

Although our studies can be directly utilized in applications that require high-electronic-quality large-area graphene such as graphene-terahertz devices[101–103], the developed bubble removal method can also improve large-area 2D insulators such as hexagonal boron nitride (h-BN) by reducing pinholes and decreasing wrinkles. We have successfully used the FDTS SAMs for bubble removal on the surface of h-BN films Fig. 3.10.
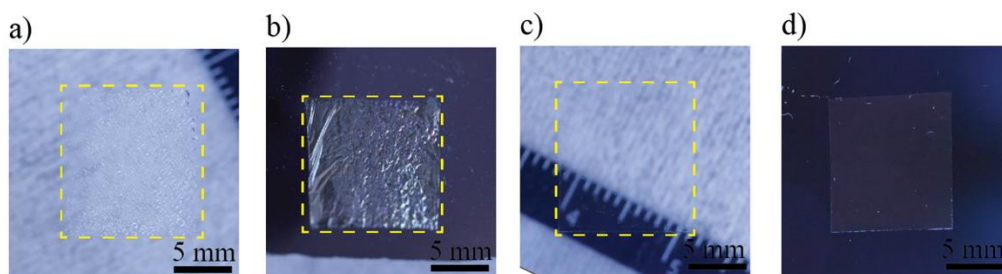
Figure 3.10: a) Bubbles generated from the electro-delamination process adhere to the bottom surface of the HBN/PMMA film. b) Bubbles removed by contacting with the FDTS SAM modified substrate. c) Floating HBN/PMMA film without bubbles on the bottom surface. d) Transferred HBN/PMMA film on target substrate following bubble removal and drying. Bubble removal also works for HBN (not limited to just graphene films) and results in flat large-area films without tears and wrinkles.

Hydrophobic functionalization is not limited to the FDST SAMs used in this work; we have also experimented with octadecyltrichlorosilane (ODTS) SAMs (Fig. 3.5) with similar effectiveness in bubble removal, but possible differences in efficacy have not been quantified. Depending on the chosen SAM, it is plausible that the interaction with the graphene (2D material) film may inhibit release from the substrate, and thus, the choice of SAM may need to be tailored for each material of choice in future uses. However, vapor deposited SAM functionalization can be

performed on full wafers, and hence, the developed method provides a scalable means for bubble removal from large-area 2D materials.

Another advantage of the developed bubble removal method is that, once the graphene film is released from the hydrophobic substrate, the adhered bubbles can be cleared simply by pulling the wafer out of solution. This facile technique allows the process to be quickly cycled, and more importantly, the functionalized wafer is readily available for further bubble removal. The reusability aspect is not true for most dry transfer techniques due to the use of non-reusable materials such as thermal release tape[5,97]. We have successfully used one single functionalized wafer for repeated bubble removal without noticeable degradation over 100 times.

We have developed a scalable and reusable bubble removal method using hydrophobic functionalized surfaces that reduce tears and wrinkles created by trapped bubbles between transferred graphene films and the target substrate to improve the large-area electronic quality of graphene devices. We confirm that the developed bubble removal method results in improved large-area mobility (device on/off ratio), and decreased (zero gate-biased) sheet resistance. Following bubble removal, the high-quality graphene was also confirmed using Raman spectroscopy mapping, and shows increased 2D:G peak ratio and decreased the D peak intensity across large areas. Our bubble removal method could find wide use in applications such as large-area 2D optoelectronics, and wafer-scale fabrication of 2D hetero devices.

Chapter 4 – Graphene-Terahertz

4.1 Transmission Line Model

To analyze the THz transmittance of metallic films on dielectric substrates, a transmission-line model can provide accurate values of the transmittance, absorptance, and reflectance over a wide frequency range[104]. The primary requirement is that the incident beam be much wider in extent than the thickness of the substrate + metallic film, and that the beam be at, or near, a "waist". The secondary requirement is that the metallic film be much thinner than a wavelength, which is quite easy to satisfy in the THz region. The "waist" condition means that the constant-phase surface for the beam is a plane perpendicular to the direction of propagation. Hence, because the transmittance depends heavily on the interference effects of propagation in the film + substrate structure, the propagation can be handled as a transverse electromagnetic (TEM) mode. And TEM modes are the basis of the transmission-line model. From a practical standpoint, it is actually more realistic than the standard "plane-wave" model in physical optics because the latter assumes the beam has not only a planar constant-phase surface but also infinite lateral extent - something impossible to achieve in real optical systems.

The equivalent-circuit diagram of the transmission-line model is shown in Fig. 4.1b. The incident beam is modelled as a TEM ideal voltage source having phasor amplitude v_s and source resistance η_0 - the intrinsic impedance of free space. The thin-film-on -substrate structure is represented by the parallel combination of a complex impedance Z_G and a possibly lossy transmission line (to account for

substrate absorption effects) of characteristic impedance Z_0. The free space region after the structure is represented by the free-space intrinsic (load) resistance η_0.
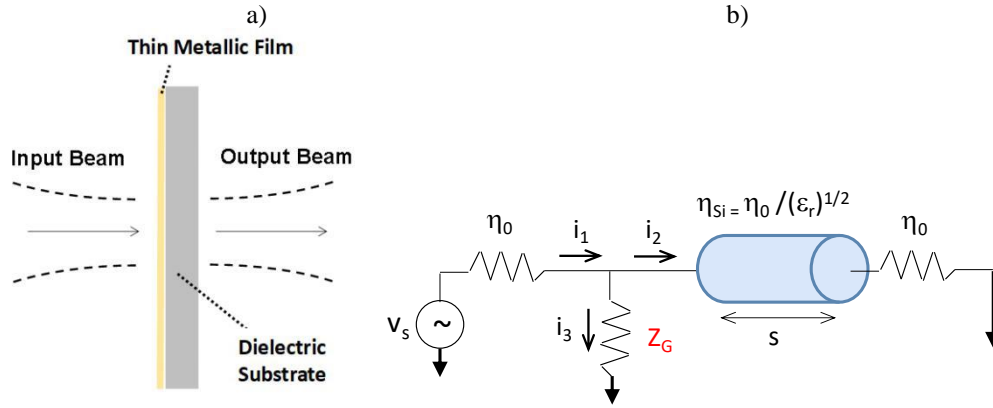
Figure 4.1: a) Beam propagation through a thin metallic film on substrate b) Transmission-line equivalent-circuit model

The combination of transmission line plus free load resistance can be written

$$\eta(s) = \eta_\sigma \left[\eta_0 + \eta_\sigma \cdot \tanh(\gamma \cdot s) \right] / \left[\eta_\sigma + \eta_0 \cdot \tanh(\gamma \cdot s) \right]$$

$$(4)$$

where s is the substrate thickness and γ is the complex propagation constant, and η_σ is the intrinsic impedance of the substrate = $\eta_0 / (\varepsilon_\rho)^{1/2}$. Eqn. (4) comes from the basic theory of lossy TEM transmission lines such that $\eta(s)$ represents the complex impedance "seen" by a generator connected to the input port[105].

Given the circuit in Fig. 4.1b, we can calculate the transmitted power, the power dissipated in the thin-film-on-substrate structure, and the reflected power as follows. We first calculate the phasor currents flowing out of the generator i_1, into

the transmission line i_2, and into the thin film i_3, where $i_1 = i_2 + i_3$ by the Kirchoff current law. By voltage division, we then have

$$i_1 = \frac{v_s}{\eta_0 + Z_G \| \eta(s)}, \quad i_2 = i_1 \frac{Z_G}{Z_G + \eta(s)}; \text{ and } \quad i_3 = i_1 \frac{\eta(s)}{Z_G + \eta(s)}$$

(5)

where the last two follow from current division. Substitution for i_1 then yields

$$i_2 = \frac{v_s}{\eta_0 + Z_G \| \eta(s)} \frac{Z_G}{Z_G + \eta(s)}$$

(6)

and,

$$i_3 = \frac{v_s}{\eta_0 + Z_G \| \eta(s)} \frac{\eta(s)}{Z_G + \eta(s)}$$

(7)

The average power dissipated in the thin-film-on-substrate structure is (assuming Ohm's law and sinusoidal phasor)

$$P_2 = \frac{1}{2} |i_2|^2 \text{Re}\{\eta(s)\} = \frac{1}{2} |v_s|^2 \left| \frac{1}{\eta_0 + Z_G \| \eta(s)} \frac{Z_G}{Z_G + \eta(s)} \right|^2 \cdot \text{Re}\{\eta(s)\}$$

(8)

and the transmittance T through the metal film is just P_2 divided by the "available power" from the source, $|v_s|^2/8\eta_0$. Hence, we can write

$$T = \frac{1}{2} |i_2|^2 \text{Re}\{\eta(s)\} = 4\eta_0 \cdot \left| \frac{1}{\eta_0 + Z_G \| \eta(s)} \frac{Z_G}{Z_G + \eta(s)} \right|^2 \cdot \text{Re}\{\eta(s)\}$$

(9)

By similar reasoning the average power dissipated in Z_G is

$$P_3 = \frac{1}{2} |i_3|^2 \text{Re}\{Z_G\} = \frac{1}{2} |v_s|^2 \left| \frac{1}{\eta_0 + Z_G \| \eta(s)} \frac{\eta(s)}{Z_G + \eta(s)} \right|^2 \cdot \text{Re}\{Z_G\}$$

(10)

Such that the thin film absorptance is

77

$$A = \frac{1}{2}|i_3|^2 \operatorname{Re}\{Z_G\} = 4\eta_0 \cdot \left| \frac{1}{\eta_0 + Z_G \| \eta(s)} \frac{\eta(s)}{Z_G + \eta(s)} \right|^2 \cdot \operatorname{Re}\{Z_G\}$$

(11)

By conservation of energy (and power), the reflectance is just

$$R = 1 - T - A$$

(12)

This set of equations can handle a wide variety of materials and conditions which are difficult to calculate by conventional (i.e., plane-wave) propagation techniques.

Special Case#1: No Substrate; Purely Resistive Film

The lack of a substrate is the simplest case since according to Eqn. (4) and the behavior of the tanh function, $\eta(s) \to \eta(s=0) = \eta_0$. Substitution into (9) then yields,

$$T = 4\eta_0^2 \cdot \left| \frac{1}{\eta_0 + (Z_G\eta_0)/(Z_G + \eta_0)} \frac{Z_G}{Z_G + \eta_0} \right|^2 = 4\eta_0^2 \cdot \left| \frac{Z_G}{\eta_0^2(1 + 2Z_G/\eta_0)} \right|^2$$

(13)

substitution into (11) yields,

$$A = 4\eta_0^3 R_G \cdot \left| \frac{1}{\eta_0^2(1 + 2Z_G/\eta_0)} \right|^2$$

(14)

and substitution into (12) yields

$$R = 1 - 4\eta_0^2(\eta_0 R_G + |Z_G|^2) \left| \frac{1}{\eta_0^2(1 + 2Z_G/\eta_0)} \right|^2$$

(15)

In the special case of a resistive film, $Z_G = R_G$, Eqn. (13) - (15) can be greatly simplified algebraically:

$$T = \frac{4R_G^2/\eta_0^2}{(1 + 2R_G/\eta_0)^2}$$

(16)

$$A = \frac{4R_G/\eta_0}{(1 + 2R_G/\eta_0)^2}$$

(17)

78

$$R = \frac{1}{(1 + 2R_G / \eta_0)^2}$$

(18)
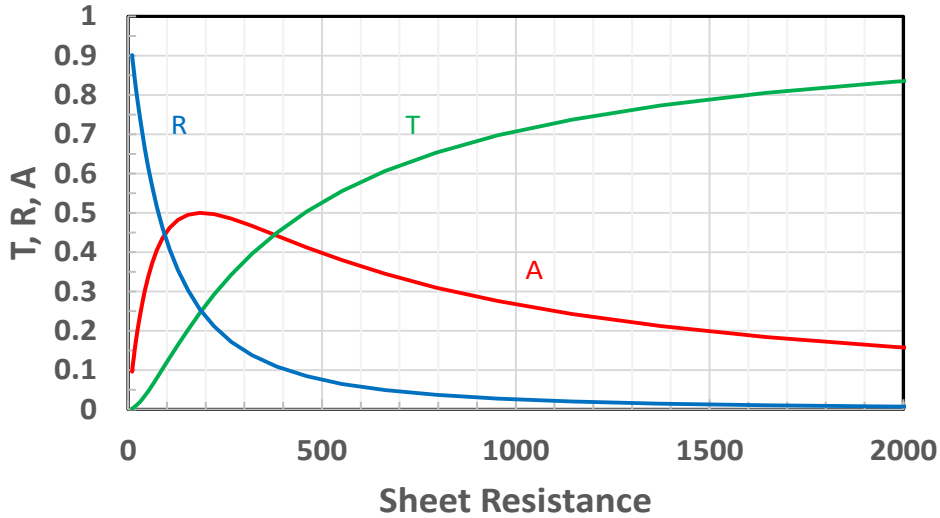
Figure 4.2: The T, R, A values versus sheet resistance for a suspended, purely resistive film.

Interestingly none of these depends on frequency unless R_G is dispersive (more on

that later). Historically, Eqn. (17) is known as the Wolsterdorff equation[106].

To check on the physical reasonableness of these last three equations, we

note that in the limit of $R_G \to 0$ (thick metal or "ideal conductor"), T =0, A =0, and R

=1, i.e., we have the "perfect mirror". In the limit, $R_G \to \infty$ (infinitesimal metal or

"ideal insulator"), T =1, A =0, and R =0, i.e., we have the "perfect transmitter". In the

special case $R_G \to \eta_0$, we have T = 4/9, A = 4/9, and R = 1/9. Plots of Eqn. (16) - (18)

vs R_G are shown in Fig. 4.2. The value of R_G that maximizes A is $R_G = \eta_0/2$ for which

T=1/4, A=1/2, and R=1/4. For all values of R_G, T + A + R = 1, consistent with

conservation of power.

Special Case#2: Lossless Substrate; Purely Resistive Film

Because of the difficulty of suspending thin metal films in free space, a more

practical case is a substrate of finite thickness but negligible loss. This can be

readily achieved even in the THz region by highly-resistive substrates having zero or very low polarity, such as high-resistivity silicon. The low polarity is necessary to make the optical phonons weakly interacting with electromagnetic radiation (silicon having near-zero polarity). In this case, we can re-write Eqn. (7) as

$$\eta(s) = \eta_\sigma \left[\eta_0 + i\eta_\sigma \cdot \tan(\gamma \cdot s)\right] / \left[\eta_\sigma + i\eta_0 \cdot \tan(\gamma \cdot s)\right]$$

(19)

which is the familiar expression from microwave engineering textbooks. Because $\eta_\sigma \neq \eta_0$, substitution into Eqn. (9), (11), (13) then creates a distinct frequency dependence consistent with the well-known behavior of transmission lines that are not impedance matched to their load. But there are special cases well known from microwave transformer theory that simplify the analysis once again.

For a "half-wave" transformer, $\gamma \cdot s = m(2\pi/\lambda) \cdot \lambda/2 = m\pi$, where m is any integer (including zero) and λ is the wavelength in the transmission-line medium having dielectric constant ε_ρ, and index of refraction, $n = (\varepsilon_\rho)^{1/2}$. This condition makes $\tan(\gamma \bullet s) \to 0$ for all m, so according to Eqn. (19), $\eta(s) = \eta_0$. And then we recover the same values of T, A, and R, as given by Eqn. (16) - (18). For a given s, the half-wave condition is satisfied by a set of periodic frequencies $\nu = m \cdot c/(2ns)$, where m = any positive integer (including zero). For a "quarter-wave" transformer, $\gamma \cdot s = (2\pi/\lambda)*\lambda/4 = \pi$, so that $\tan(\gamma\sigma) \to \infty$, and $\eta(s) = (\eta_\sigma)^2/\eta_0$.

Using the transmission line model, the effect of different substrate dielectric constant/index of refraction can be easily accounted for, and provides a convenient "device design tool". For our experiments where graphene is mounted on a silicon substrate, $\varepsilon_s \approx 11.66$, and a substrate thickness of L = 400 μm is used for the

calculations of T, R, and A. These values are compared to a suspended film, and a graphene film on substrate in Fig. 4.3. In order to investigate the frequency dependence, in the figure below, the scattering time is set as, τ = 50 fs, as this value is widely reported in the literature (see table below). On half-wave resonance ($\sim$ 110 GHz for L = 400 µm), which occur at even integer multiples of $f = \frac{c}{(4*n*L)}$, or when kL = Nπ, the transmittance, reflectance, absorptance values from the transmission line model reduce to the Woltersdorff[106] values. In contrast, at odd integer multiples $f = \frac{c}{(4*n*L)}$, the device is at quarter-wave resonance ($\sim$ 164 GHz for L = 400 µm), and mostly reflecting. The equations for T, R, A are listed below. For device design, in the limit where the substrate index of refraction n = 1, and thickness of L = 0, the frequency dependent Fabry-Perot fringes of T, A, R decrease in amplitudes, and approaches the ideal case of a suspended film where the T, R, A values are generally flat with broadband, 50% absorption, matching the Woltersdorff values.

It is important to note that, even though the transmission line model matches the Woltersdorff values at the half-wave resonance values (Fig. 4.3d,h), the half-wave resonance condition does not always occur at a transmittance peak maxima. The half-wave resonance condition occurs at a transmittance maxima up to a certain critical sheet resistance value (i.e. when the sheet resistance is large), but because of a phase shift when the graphene film becomes reflecting (i.e. when the sheet resistance value is small), the half-wave resonance condition occurs at the transmittance minima[104]. This phenomenon is obvious in Fig. 4.3e; for sheet

resistance values greater than 156 Ω/sq, the half-wave resonance condition occurs at the transmittance maxima, but for sheet resistance values less than 156 Ω/sq, the half-wave resonance condition occur at the transmittance minima. In this work, we never reach this critical sheet resistance threshold, and thus, in the manuscript, the half-wave resonance condition is referred to at the transmittance peak maxima. The opposite situation occurs for quarter-wave resonance, that is, for high sheet resistance the quarter-wave resonance occurs at a transmittance minima, but after the critical sheet resistance is reached, the quarter-wave resonance flips and occurs at the transmittance maxima.
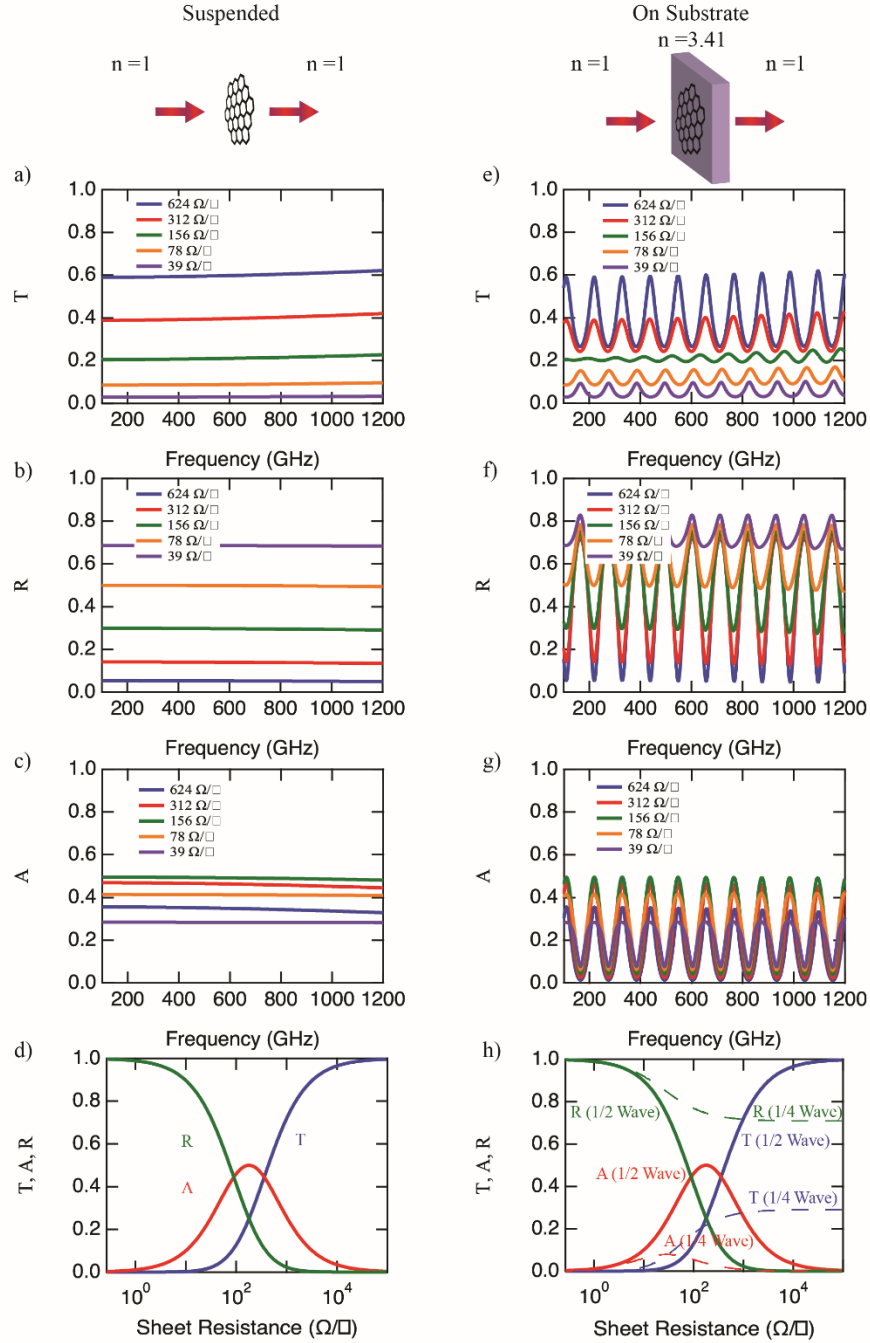
Figure 4.3: Two scenarios were analyzed to investigate the effects of the index of refraction of the substrate used in this work: suspended graphene films, and graphene on a substrate of finite thickness (n = 3.41, L = 400 um) with the THz beam incident on the graphene film first. a-c) The frequency dependent T, A, R was calculated for a suspended film for various assumed values of the DC sheet resistance. d) The single frequency T, A, R values for a suspended film as the sheet resistance is varied. e-g) The frequency dependent T, A, R was calculated for a film on a substrate, using the transmission line model for various assumed values of the DC sheet resistance. At the half-wave resonance, the amplitudes of the transmittance match those of the suspended sheet. h) The half-wave resonance, and quarter-wave resonance values for T, A, R are plotted as the sheet resistance is varied.

Theoretical T, R, A for Suspended Film (Woltersdorff[106])

$$A = \frac{4\,(R_\square/Z_0)}{(1 + \frac{R_\square}{Z_0/2})^2}$$

(20)

$$A = \frac{4\,g}{(1 + 2g)^2}$$

(23)

$$R = \frac{1}{(1 + \frac{R_\square}{Z_0/2})^2}$$

(21)

$$R = \frac{1}{(1 + 2g)^2}$$

(24)

$$T = \frac{1}{(1 + \frac{Z_0/2}{R_\square})^2}$$

(22)

$$T = \frac{4g^2}{(1 + 2g)^2}$$

(25)

Quarter-Wave Resonance Case (Incident on Graphene)

$$A = \frac{4\,R_\square Z_0}{|R_\square n + R_\square + Z_0|^2}$$

(26)

$$R = \left| 1 - \frac{2R_\square}{R_\square n + R_\square + Z_0} \right|^2$$

(27)

$$T = 4Z_0{}^2 \left| \frac{R_\square}{2R_\square Z_0 + Z_0{}^2} \right|^2$$

(28)

The absorptance versus sheet resistance is plotted using the general absorptance Eqn. (10) – (12) in the case where the THz beam is incident on the graphene side for three values of the n (substrate index of refraction), while varying kL from 0 to 2π. When n = 1 the maximum absorptance is 50%. The maximum absorptance value is also 50% with when n = 3.41 (substrate used in this work) at the half-wave resonance values (kL = Nπ), with a minimum value of ∼ 8% in the quarter-wave resonance case. Although Eqn. (10) – (12) can yield absorptance

values greater than 50%, this is only satisfied for values of n < 1, which is not considered in this manuscript, but nonetheless useful for cases such as metamaterials. Hence, 50% is considered the maximum for incidence on the graphene side.
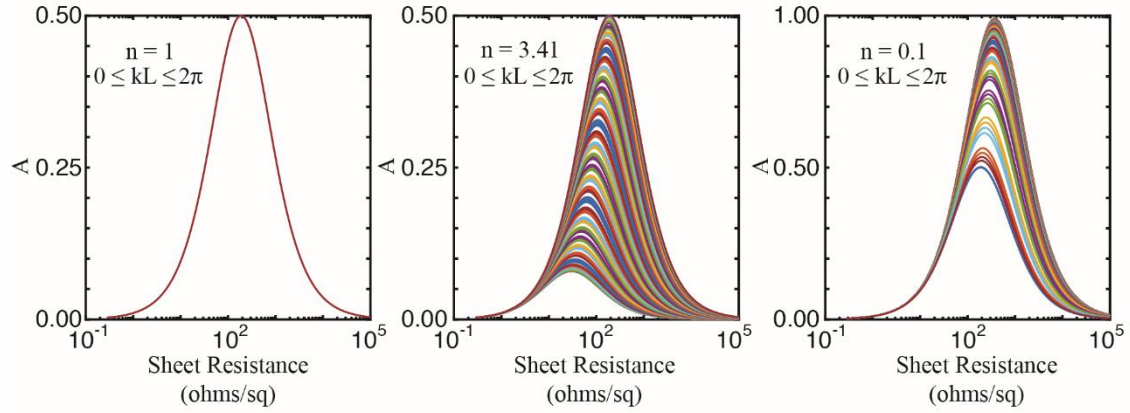
Figure 4.4: The absorption versus sheet resistance for 3 different values of n, while varying kL from 0 to 2π.

The case where the THz beam is incident on the substrate first (with a graphene film on the backside) was investigated analytically with similar results as ref[107]. Contrary to the experimental setup used in this work, that is, where the THz beam is incident on the graphene film, if the THz beam is incident on the substrate side, the transmittance through the etalon remains the same (compared to incidence on the graphene side), but the reflectance and absorptance are different. The absorptance is plotted (with n = 3.41) varying the graphene sheet resistance and kL varying from 0 – 2π in Fig. 4.4a Although the values T, R, A, remain identical at half-wave resonance when kL = Nπ, at quarter-wave resonance, as clearly evident at kL = Mπ, where M is odd integer values, the total reflectance can decrease, resulting in increased absorbance. For this case (which is different from the experimental setup

85

in this work) the absorptance values can be greater than 50% for n > 1. The peak

absorption found at very low sheet resistance values calculated here were not

apparent in similar plots in ref[107] (the sheet resistance where absorption begins to

decrease was beyond the range analyzed), but here we emphasize that a sheet

resistance dependent maximum absorption does indeed occur. The maximum

absorptance, and the sheet resistance value at which it occurs can vary depending

on the substrate index of refraction. These values were computed in Fig. 4.5b. Here,

it is obvious that the largest sheet resistance value for maximum absorbance occurs

at 377/2 Ω/sq, when n = 1. Absorptance values greater than 90% can be achieved

when n > 3 with the sheet resistance value required decreasing to values < 100

Ω/sq.
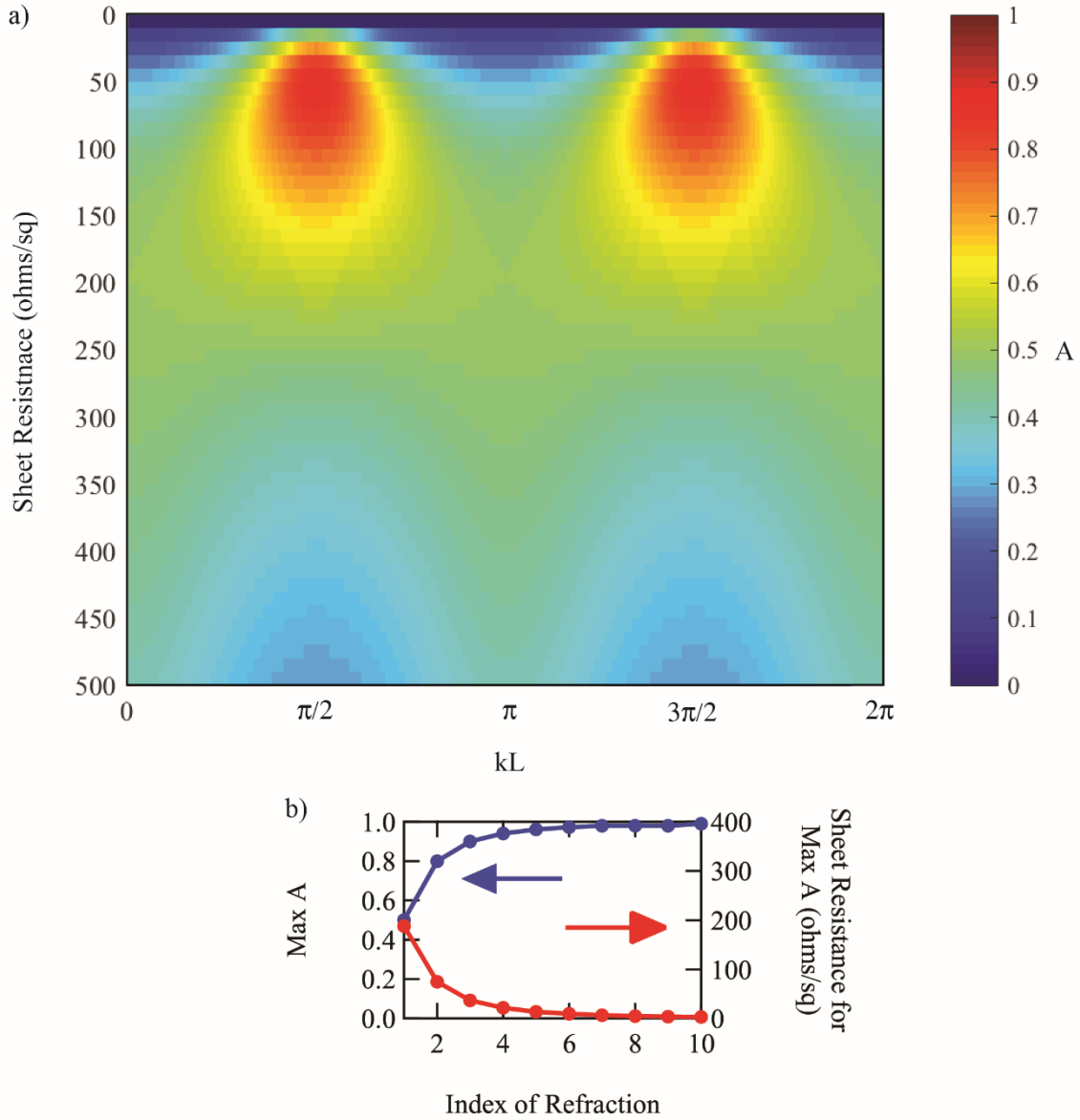
Figure 4.5: a) The absorptance is plotted for the case when the THz beam is incident on the substrate (n = 3.41) side first as a function of the sheet resistance (ohms/sq) with kL varying from 0 − 2π. b) The maximum absorptance, and the sheet resistance required for various values of the index of refraction of the substrate.

T, R, A (Incidence on Substrate Side)

$$T = 4Z_0 \left| \frac{gn\big(n\sin(kL) - i\cos(kL)\big)}{(1 + g + gn^2)Z_0\sin(kL) - i(1 + 2g)nZ_0\cos(kL)} \right|^2 \frac{2Z_0}{1 + n^2 - \cos(2kL)\,(n^2 - 1)}$$

$$(29)$$

$$R =$$

$$\left| \frac{(1 + g - gn^2)\sin(kL) + in\cos(kL)}{(1 + g + gn^2)\sin(kL) - i(1 + 2g)n\cos(kL)} \right|^2$$

(30)

$$A =$$

$$4gZ_0^4 \left| \frac{n}{Z_0^2((1 + 2g)n\cos(kL) + i(1 + g + gn^2)\sin(kL))} \right|^2$$

(31)

4.2 Absorption, Transmission, and Reflection Regimes

The graphene films are mounted on high-resistivity silicon substrates of thickness ~ 400 μm, which do not absorb significantly in the THz region. Because of the difference in the index of refraction between the silicon substrate ($n \approx 3.4$) and air ($n = 1$), there is an etalon effect present in the frequency dependent transmission (even in the absence of graphene). With graphene present, we can model the effect of varying the graphene sheet resistance to calculate the net transmittance using the transmission line model, and compare these values (for a film on a substrate with incidence in both directions) to that of a suspended graphene film Fig. 4.6a-c.

a) Suspended Sheet **b)** On Substrate **c)** On Substrate

(Incident on Graphene) (Incident on Substrate)

d)
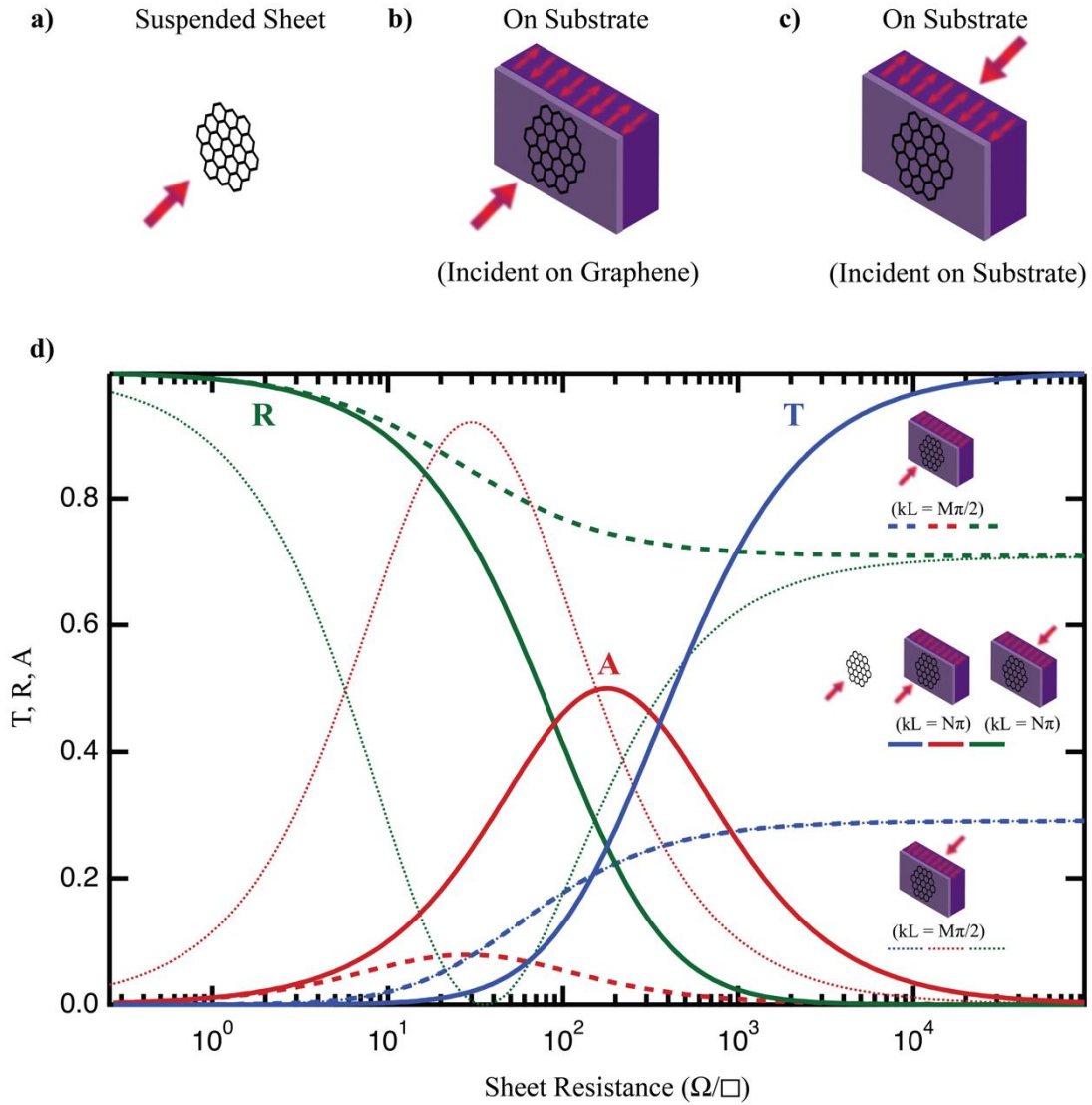
Figure 4.6: a-c) A suspended film, and a film on a substrate for two incidence directions were analyzed using the transmission line model. *n* **= 3.41 was used as the substrate index of refraction for calculation. d) The suspended film/Woltersdorff equations (plotted as solid lines) for T, R, A versus sheet resistance were compared to a film on a substrate. When the half-wave resonance condition is satisfied, (k***L* **= N***π***, where** *N* **is an integer), the equations for T, R, A reduce to exactly the Woltersdorff equations (plotted for both directions as solid lines, and are indistinguishable from the suspended film). Hence, analyzing the device at half-wave resonance provides a direct comparison of the graphene absorption on a substrate to that of a suspended film. At quarter-wave resonance**

A plane wave can be transmitted (T), reflected (R), or absorbed (A). Electromagnetics states that a perfect conductor is a mirror (T=0; R=1; A=0), and a perfect insulator is a transmitter (T≤1, R≥0, A=0). What is the quantitative relationship between T, R, A, and the sheet resistance? The three are not completely

independent, as T+R+A must equal unity due to conservation of energy. The relationship for the transmittance, reflectance, and absorptance of a suspended thin metallic film was derived in 1934[106], and is given by,

$$T = \frac{4g^2}{(1+2g)^2}$$

(32)

$$R = \frac{1}{(1+2g)^2}$$

(33)

$$A = \frac{4\,g}{(1+2g)^2}$$

(34)

$$g \equiv R_\square / Z_0$$

(35)

These expressions show the change from transmission-dominating to absorption-dominating occurring at the critical threshold of $Z_0 = 377\ \Omega$. Within the absorption-dominating regime, the peak absorption occurs when the sheet resistance is equal to $Z_0/2$, Fig. 4.6d.

When mounted on a substrate of index of refraction, n, numerous considerations such as direction of normal incidence (on the graphene or substrate side first) and substrate thickness govern T, R, and A. Furthermore, interference effects from the substrate cause Fabry-Perot behavior depending on the THz frequency (f), substrate thickness (L), and index of refraction (n). When incident on the graphene side first, the general analytical expressions for T, R, A are given by,

$$T = 4Z_0 \left| \frac{gn(n\sin(\mathbf{k}L) - i\cos(\mathbf{k}L))}{(1+g+gn^2)Z_0 \sin(\mathbf{k}L) - i(1+2g)nZ_0 \cos(\mathbf{k}L)} \right|^2 \frac{2Z_0}{1+n^2 - \cos(2\mathbf{k}L)(n^2-1)}$$

(36)

$$R = \left| \frac{(1-g+gn^2)\sin(\mathbf{k}L) - in\cos(\mathbf{k}L)}{(1+g+gn^2)\sin(\mathbf{k}L) - i(1+2g)n\cos(\mathbf{k}L)} \right|^2$$

(37)

90

$$A = 4gZ_0^4 \left| \frac{\sin(\mathbf{k}L) - in\cos(\mathbf{k}L)}{(1+g+gn^2)Z_0 \sin(\mathbf{k}L) - i(1+2g)nZ_0\cos(\mathbf{k}L)} \right|^2$$

(38)

Similar expressions for incidence on the substrate side are given in Eqn. 29 - 31.

For both incidence directions, when $\mathbf{k}L=N\pi$, where $\mathbf{k}$, is the wave vector, L is the substrate thickness, and N is integer values, or when the THz frequency is at half-wave resonance with the graphene-silicon etalon, which occurs at even integer multiples of $f = \frac{c}{(4*n*L)}$, the equations for T, R, A reduce to exactly the same as the Woltersdorff equations[106], Eqn. (32) – (34). Hence, for a broadband transmittance measurement, at half-wave resonance, or at the transmittance maxima (up to a critical sheet resistance value, after which the half-wave resonance occurs at the transmittance minima, the behavior of the graphene film can be directly compared to a suspended film, where the onset of strong absorption occurs at $Z_0 = 377$ Ω, with maximum absorption of 50% occurring at $Z_0/2$. In Fig. 4.6d the half-wave resonance condition for T, R, A are indistinguishable from those of the suspended case.

In contrast, at quarter-wave resonance, when $\mathbf{k}L=M\pi/2$, where M is odd integer values, the sheet resistance dependent transmission through the graphene-silicon etalon remains low (transmission never dominates). Although the transmittance is low and equivalent for both incidence directions (graphene or substrate first), the sheet resistance dependent reflection and absorption indeed depend on the incidence direction. When the THz beam is incident on the graphene side first, interference effects cause the device to behave as mostly reflecting (always reflection-dominating), resulting in low absorption. On the other hand, when the THz beam is incident on the substrate first (with graphene on the

backside), the absorption, transmission and reflection can be affectedly tuned by the sheet resistance. This allows the absorption maximum to increase to > 50% for low sheet resistance values (Fig. 4.5a).

The two extreme cases (half-wave resonance and quarter-wave resonance) shows contrasting behavior, but like the suspended film, there still exists certain impedance values that determine the peak absorption, and the onset of the absorption-dominating threshold, Fig. 4.6d. The absorption-dominating threshold and peak absorption can shift (to even lower sheet resistance values) depending on the substrate index of refraction. We have calculated and plotted this trend for various values of the index of refraction in Fig. 4.5b. Regardless if the graphene film is suspended, or on a substrate, the largest sheet resistance value (most resistive) in which the film becomes absorption dominating is 377 $\Omega/\square$, and hence, this value signifies the doorway to strong absorption. Detailed below, we observe a decrease in the broadband transmittance as the graphene sheet resistance is tuned below 377 $\Omega/\square$, signifying absorption approaching the 50% maximum for a THz beam incident on a graphene sheet on substrate.

4.3 Graphene-Terahertz Coupling without Optimization

In order to fabricate a back-gated graphene-THz modulator, we started with commercially available graphene from Graphene Square. To act as scaffold support during transfer, we spun a layer of PMMA (30 mg/ml) onto our graphene on copper foil sample for 30 seconds at ~4000 RPMs. After the PMMA cured overnight, graphene on the backside of the copper foil was removed using O_2 plasma. The copper foil was then etched away in ~5% ammonium persulfate solution for ~12

hours. The floating graphene/PMMA stack was then cleaned in deionized water, and "wet transferred" onto our target, 90 nm oxide on silicon substrate. Following drying overnight, the PMMA was first removed using acetone, and further removed by annealing under argon and hydrogen at 400 C for 1 hour. The inset in Fig. 4.7. shows a typical graphene device fabricated using this method.

In order to assess the DC behavior of the device, electrodes are deposited on the sides of graphene. Using an electrostatic back gate, graphene carrier density of the GFET can be effectively tuned; we can easily verify gate voltage induced changes in carrier density by measuring the source-drain current as we alter the gate voltage. Source-drain current vs. voltage curves for different back gate voltages are shown in Fig 4.7. Modest transconductance was observed, but does confirm back gating field-effects.
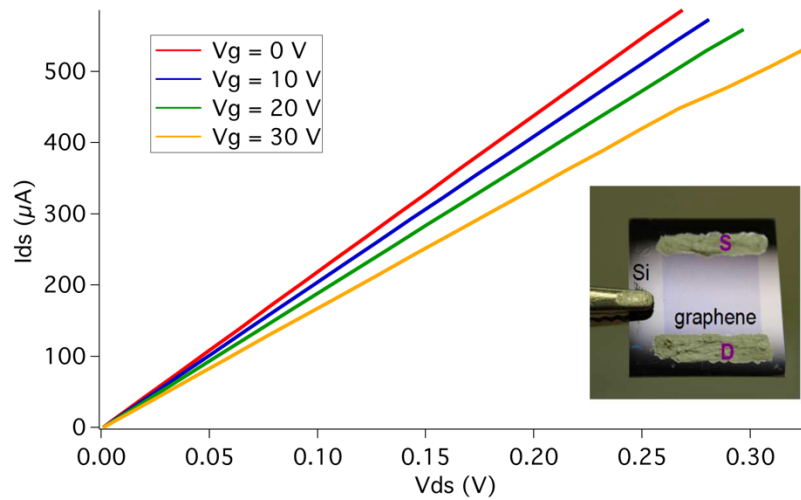
Figure 4.7: Source-drain current vs gate voltage for a GFET device. Different Gate voltages induce changes in carrier density. Inset shows typical 1 x 1 cm^2 GFET with electrodes.

After confirming DC behavior of the GFET, THz transmission measurements were carried out in an Emcore PB7100/PB7200 Broadband Frequency-Domain THz

Transceiver. The Emcore 7100 and 7200 can sweep between .1 – 1.6 THz with 500 MHz resolution while maintaining at least 40 dB dynamic range; the beam size is approximately 3mm diameter[108]. The measurement schematic is shown in Fig. 4.8.
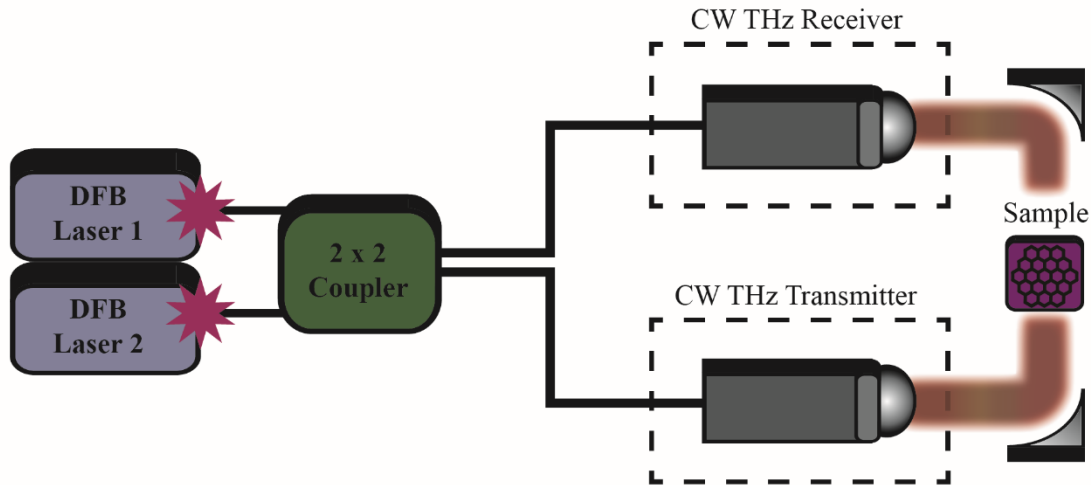
Figure 4.8: Block diagram of the Emcore PB7200 broadband frequency-domain photomixing spectrometer used to perform THz transmission measurements through the graphene-on-Si etalon structures. Two distributed feedback lasers (DFB) are mixed in order to perform broadband frequency sweeps between 0.2 – 1.2 THz with 500 MHz steps.

For our experiment, we used a range of .2 – 1.2 THz. Before measuring a control sample of bare silicon, a background measurement (with nothing in the beam path) and a noise measurement (with a metallic plate in the beam path) were performed. Then, as a control, a bare silicon wafer (of the same thickness as our GFET) was placed in the beam path, and the transmission was measured; transmission maxima (near unity) and minima are observed since the silicon wafer acts as a Fabry-Perot resonator, setting the "baseline" for our modulation measurement.

Upon inserting a GFET device into the THz beam path, we observed a clear decrease in the maxima of the transmission peaks as compared to those of the nearly lossless silicon wafer as shown in Fig. 4.9 (left). We know from the DC measurement that since our graphene film exhibits nearly 20 times the conductivity of that of the optical value, a significant portion of the incident THz wave should interact with the graphene, a result that is confirmed over broadband frequencies. Upon applying 5 V on the gate, we observed a small amount of modulation of the broadband transmission Fig. 4.9 (right).
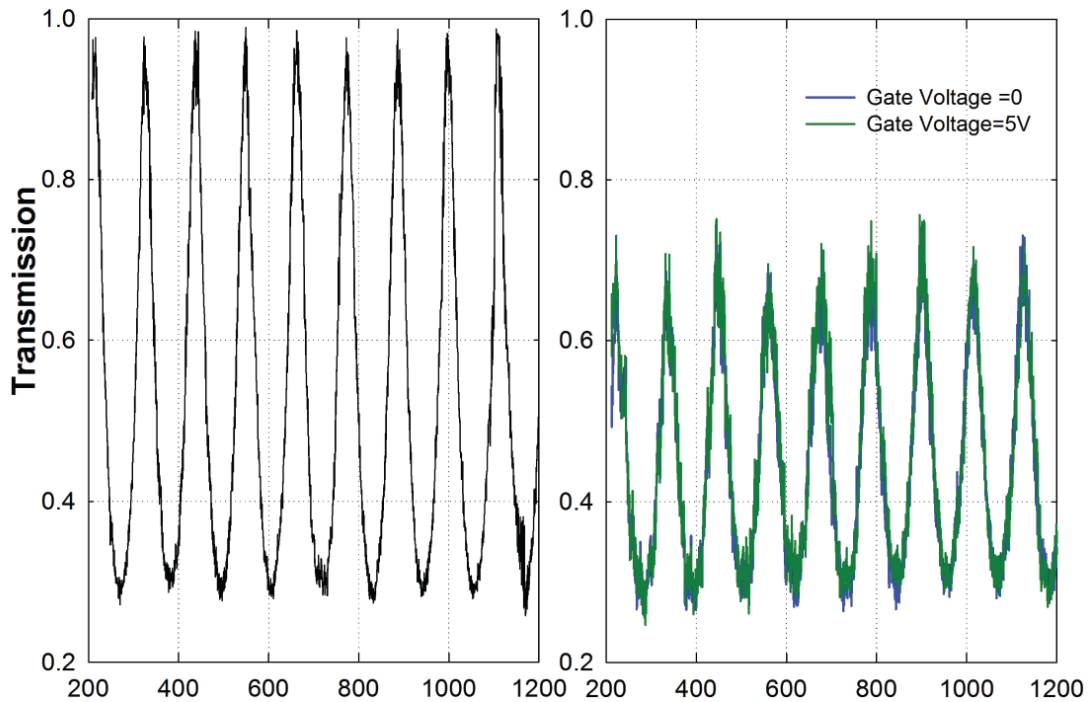
Figure 4.9: Nearly lossless transmission from bare silicon control sample (left). Reduction of THz transmission from addition of graphene, biased at 0 V and 5 V (right).

From the etalon transmission measurement, we can extract the complex graphene conductivity using the transmission matrix method (TMM) outlined below.

Since we know that the transmittance of the THz beam through the substrate equates to $T_e = |S_{21}|^2$ where,

$$S_{21} = \frac{t_1 t_2 exp(-jk_s L)}{1 + r_1 r_2 \exp(-2k_s L)}$$

(39)

where L is the substrate thickness, and k_s, the wave vector inside the substrate, is equal to $2\pi\mathcal{E}_s/\lambda$. t_1 and r_1 are coefficients of transmission and reflection for the air/Si etalon and are given by,

$$r_1 = \frac{1 - \sqrt{\varepsilon_s}}{1 + \sqrt{\varepsilon_s}}$$

(40)

$$t_1 = \frac{2}{1 + \sqrt{\varepsilon_s}}$$

(41)

where $\mathcal{E}_s$ is the substrate dielectric constant, and λ is the free space wavelength. The Si/graphene/graphene/air etalon is given by,

$$r_2 = \frac{\sqrt{\varepsilon_s} - \left(\sqrt{\varepsilon_g} + 1\right)}{\sqrt{\varepsilon_s} + \left(\sqrt{\varepsilon_g} + 1\right)}$$

(42)

$$t_2 = \frac{2\sqrt{\varepsilon_s}}{\sqrt{\varepsilon_s} + \left(\sqrt{\varepsilon_g} + 1\right)}$$

(43)

Where $\mathcal{E}_g$ is the complex dielectric constant of graphene. Finally, the conductivity of graphene is given by,

$$\sigma_g = \frac{\sqrt{\varepsilon_g}}{377}$$

(44)

where 377 Ω is the impedance of free space. In order to solve for the graphene conductivity, we simply needed to fit the transmission data to solve for the complex dielectric constant, $\mathcal{E}_g$, applying the TMM. To do so we used a least squares fitting procedure on each transmission peak to solve for the complex dielectric constant. Fig. 4.10 shows the calculated real and imaginary conductivity values plotted versus frequency using the fitted complex dielectric constant.
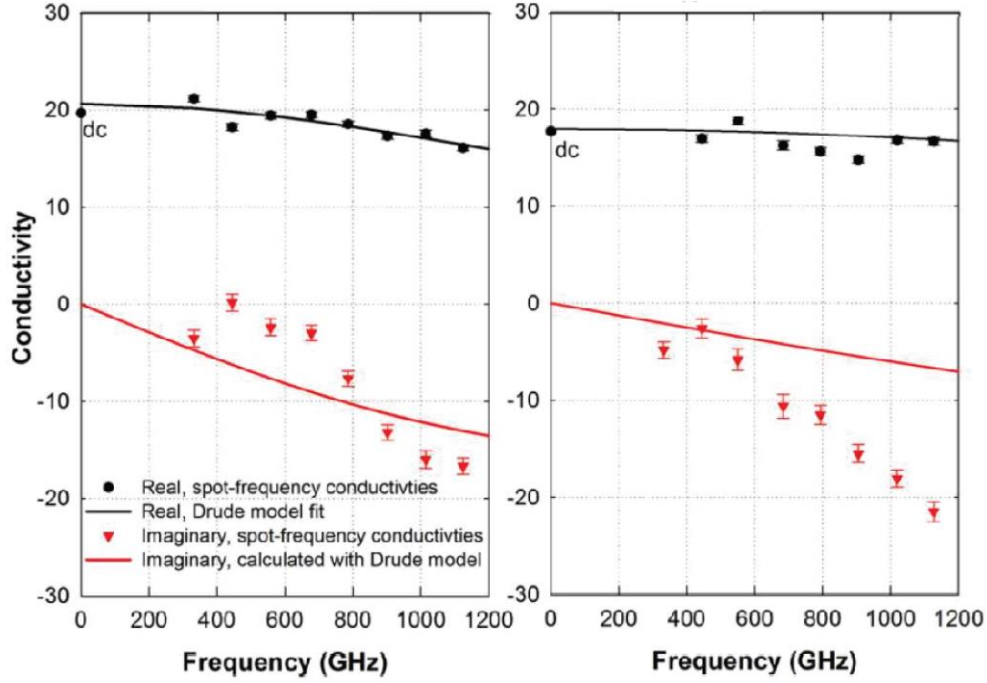
Figure 4.10: Calculated conductivity using transmission data for 0 V (left) and 5 V (right). The real conductivity (at spot frequencies) is fitted to the Drude model to extract the scattering parameters and Fermi level. These values are inputted into the Drude to plot the imaginary trend.

We then used the calculated complex conductivity values, and plugged them into the Drude model of intraband conductivity, which are given by,

$$Re\{\sigma_{intra}(\omega)\} = \frac{e^2}{4\hbar} \frac{2}{\pi} \frac{8k_B T\Gamma}{\hbar^2 \omega^2 + 4\Gamma^2} \log\left[2\cosh\left(\frac{\mu}{2k_B T}\right)\right]$$

(45)

$$Im\{\sigma_{intra}(\omega)\} = - \frac{e^2}{4\hbar} \frac{2}{\pi} \frac{4k_B T\hbar\omega}{\hbar^2 \omega^2 + 4\Gamma^2} \log\left[2\cosh\left(\frac{\mu}{2k_B T}\right)\right]$$

(46)

Thus, using the extracted spot frequency conductivities previously attained, we can do an additional least squares fit to the real conductivities (the standard deviation for the real was 2-3% while the standard deviation for the imaginary portion was as high as 50%, thus the imaginary was not fitted to), and obtain Γ and μ. This fitting of the spot frequency conductivities (also plotted in Fig. 4.10) yielded values of Γ = 4.6 meV, μ = -.015 eV for the device at 0V on the gate, and Γ = 9.23 meV, μ = -0.26 eV at

97

5V on the gate. Accordingly, the scattering time constants $\tau = \hbar/2\Gamma$ are 72 fs at V_{GS} = 0, and 36 fs at V_{GS} = 5 V. Using these parameters, we can input the calculated Γ and μ values to create a fit line for the imaginary Drude prediction (45); this line is added in Fig 4.10. Calculating the DC conductivity using equation (45) gives us a value of 20.63 $e^2/4\hbar$ at 0 gate volts, which is very close to our measured value of 19.7 $e^2/4\hbar$, and thus confirms the accuracy of our parameter fitting procedure.

We have successfully demonstrated a dramatic increase of on/off ratio of large-area GFETs devices. Using these devices, we aim to measure the depth of modulation using a set 101 GHz transmission set up. Initial depth of modulation experiments are shown in Fig. 4.11; we show both the change of source-drain current as a function of gate voltage, and amplitude of transmission as a function of gate voltage.
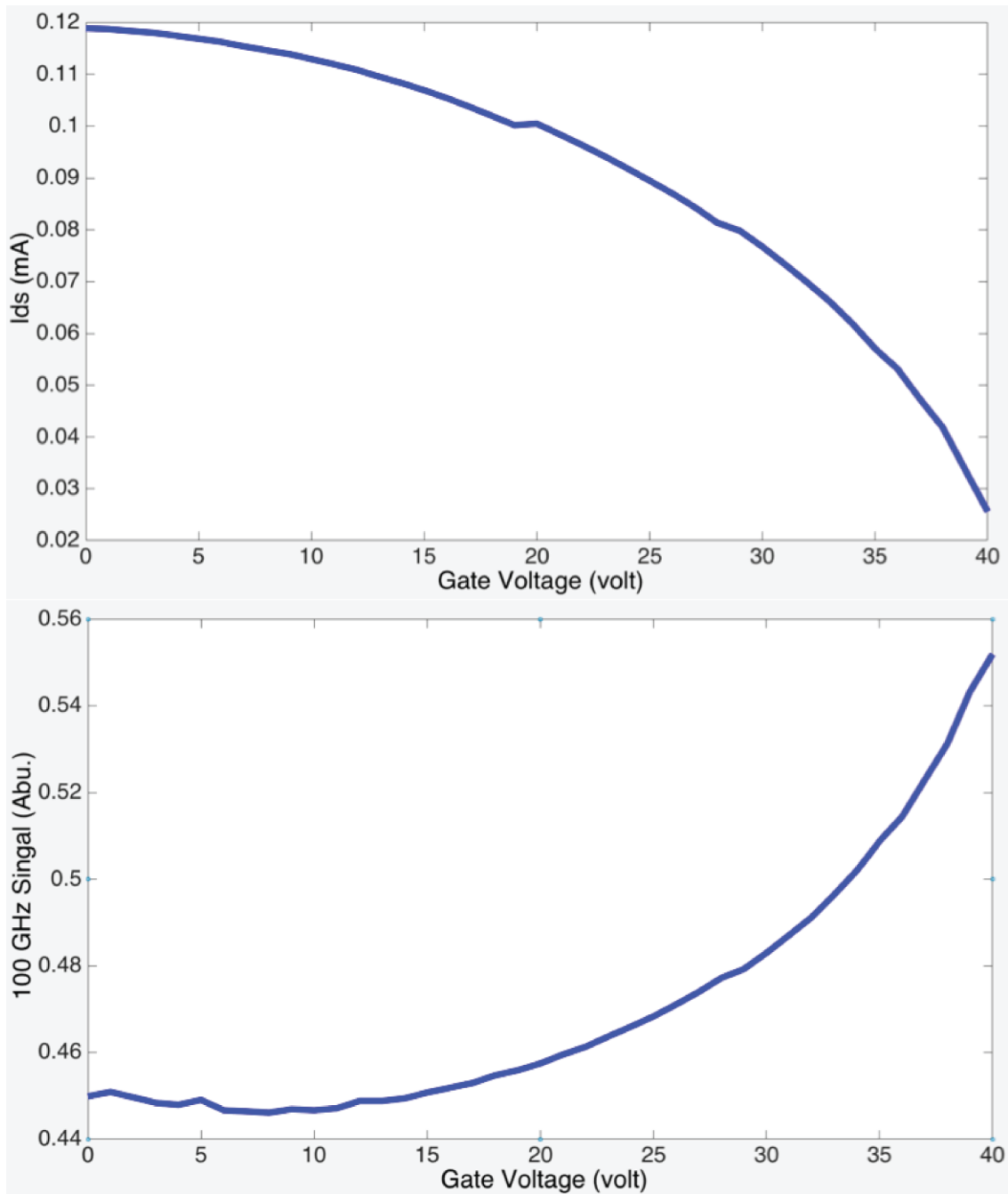
Figure 4.11: Initial test for transmission depth of modulation. (top) shows the depletion curve for the GFET, (bottom) shows amplitude of 101 GHz signal as a function of gate voltage.

The on/off ratio for the above device is ~4, with a depth of modulation ~18%. By increasing the on/off ratios to ~6, we anticipate that the depth of modulation can be greatly improved. A noteworthy milestone would be 40% depth of modulation for a transmission measurement of single-layer graphene.

4.4 Impedance Matching

In circuits, impedance means the ratio of the voltage across a given element to the current through a given element, and can be complex (i.e. the current and voltage may be out of phase). An "element" is a physical object with dimensions much smaller than the wavelength at the frequency of interest. The resistance, reactance, admittance, susceptance, and conductance all are various representations of the real or imaginary part of the impedance or its inverse. However, in our experiments, there are no "elements" (all of our structures are of order the wavelength in size), hence one must consider the electromagnetics of waves, not lumped elements.

In electromagnetic waves, the wave impedance means the ratio of the electric field to the magnetic field, and can also be complex (i.e. the electric field and magnetic field may be out of phase). This is also sometimes referred to as the characteristic impedance or the wave impedance of the medium. In cases where the medium is not lossy, the electric field and magnetic field are in phase, and hence the wave impedance is purely real. For example, in vacuum, the wave impedance is 377 Ω. Even though there is no imaginary component, one still generally refers to this as the "characteristic impedance of free space". For all of our experiments, the medium is not absorbing and so the wave impedance is always real. In a medium with index of refraction *n* (assuming *n* real as is the case for our experiments), the wave impedance (or also called the characteristic impedance of the medium) is given by 377 Ω/n. Note that a similar definition holds for the characteristic impedance of a

transmission line, which is a distributed inductance and capacitance (and perhaps conductance).

In the context of conducting media such as a metal, the wave impedance has significant imaginary components. In this case, the wave impedance is referred to as the "surface impedance",[109] even for cases where the waves are propagating and there is no physical "surface" in sight. We avoid this definition of "surface impedance" as it does not directly apply to our case.

Instead, we use the concept of sheet resistance. The sheet resistance of a thin film is the ratio of the voltage through a film of width W and length L to the current through that film, divided by the number of squares, i.e. L/W. The concept of sheet impedance is similar; if the voltage and current are out of phase the sheet impedance can have an imaginary component. The sheet conductance is defined similarly. While we consider the case of an imaginary component in the supplementary info for our experiments, we find little evidence for it experimentally in our frequency range and so the main text focuses the sheet resistance only.

The purpose of this paper is to show that, when a plane wave is incident on a thin film, the transmission, reflection, and absorption coefficients of that plane wave depend on the ratio of the characteristic impedance of the wave to the sheet resistance of the thin film.

The quantitative calculation of the transmission, reflection, and absorption coefficients is simplified dramatically using a transmission line equivalent circuit model that captures the key electromagnetic wave phenomena but requires only the

use of discreet or disturbed circuit elements, and is described in detail. The model was validated theoretically and experimentally[104].

To date, unpatterned monolayer graphene devices have operated exclusively in the weakly coupled, highly transmissive regime[16–19,101,102,110–116]. Here, by deliberate engineering of the sheet conductance using large-domain graphene films in combination with chemically modified substrates (to decrease interface scattering), as well as chemical and electrical doping, we fabricate monolayer graphene devices with sheet resistance crossing the characteristic impedance of free-space, 377 Ω /□. Achieving this, we show that monolayer graphene can be tuned to behave as a strong absorber over a broadband frequency range, approaching the theoretical impedance at which absorption is maximized[106,117]. In free-space, the maximum absorption is 50%; whereas on a substrate it can be greater than 90% depending on the direction of normal incidence, discussed in detail below. Regardless of the case (free- space or on dielectric), the absorption is much larger than the 2.3% optical value[2], and thus, represents a milestone of coupling electromagnetic waves to an atomically thin nano-material. This is measured over an extremely broad range, from mm-wave to THz frequencies. Strong EM absorption using a single atomic layer exemplifies the fundamental relationship between nanoscale electronics and classical electromagnetism.

This creates the opportunity to adjust the THz conductance into the regime where the majority of the incident light is absorbed (A > R, T). This prospect is indicated schematically within the THz frequency range in Fig. 4.12b, where hypothetical conductance curves for plausible E_F and values are plotted. Fig. 4.12c

presents "device design" charts (calculated for 100 GHz), which show how combinations of E_F and affect the AC conductance; the absorption-dominating regime begins when the sheet resistance ≤ 377 $\Omega/\square$ (set as red on the z-axis color scale). Previous investigations of single-layer graphene-THz absorption fail to surpass the $Z_0 = 377$ Ω threshold[16–19,101,102,110–116] (denoted as circles in Fig. 4.12c), even in the case where E_F was designed to be purposefully large (using heavy chemical doping[16,114], or strong electrical gating[16,17,101,111,112,114]). Instead, as demonstrated in this work and emphasized as an arrow in Fig. 4.12d, by carefully fabricating devices with improved , the graphene conductance can be large (denoted as an 'x' in Fig. 4.12c), and the device sheet resistance can be tuned to be below the free-space impedance threshold. We successfully surpass this threshold with a graphene sheet, and reach near maximum absorption.
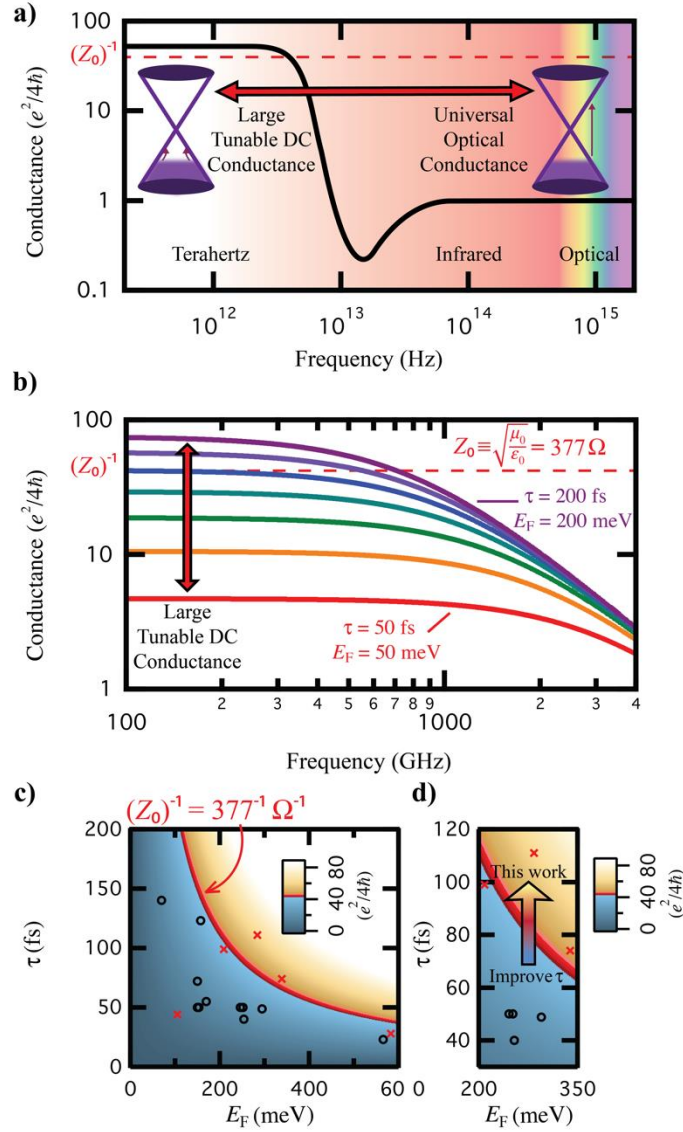
Figure 4.12: a) Qualitative trend of frequency dependent AC conductance for monolayer graphene with normalization to $e^2/4\hbar$. The optical frequency range exhibits a universal value of 1, while in the THz range, the AC conductance can be orders-of-magnitude higher. b) Theoretical trend of THz AC conductance for monolayer graphene plotted with a linear variation of the E_F, and τ. Graphene samples can cross the free-space conductance value, $(Z_0)^{-1}$, within the THz regime. c) Device design plot showing the graphene sheet conductance (at 100 GHz) in units of $(e^2/4\hbar)$ for changes in E_F, and τ. The $(Z_0)^{-1}$ threshold is set as red on the color scale. Previous graphene-THz device parameters are plotted as circles, whereas those from this work are denoted as x's. d) By decreasing the electron scattering in our devices to increase τ, the $(Z_0)^{-1}$ threshold can be crossed into the absorption-dominating regime.

Previously, researchers used bare, unpatterned graphene, and measured the THz resistance to be greater than 377 Ω[16–19,101,102,110–116]. This includes our previous work[19], where the graphene-etalon structures were fabricated using chemical-

vapor-deposited graphene films[4] transferred[7] onto a 90 nm gate oxide layer on high resistivity silicon substrates. To improve τ, so as to increase the conductance of the devices, we synthesized large-domain (mm-sized) graphene films (to minimize graphene grain boundaries)[99], in addition to depositing octadecyltrichlorosilane (ODTS) self-assembled-monolayers (SAM) on the wafer (to decrease scattering)[58] prior to graphene transfer.

CVD grown, monolayer graphene films are transferred onto an ODTS SAM on the SiO_2 substrate depicted in Fig. 4.13. The ODTS SAM is vacuum deposited on the wafer prior graphene transfer. During the transfer step, BI can be introduced on the bottom of the film to intentionally dope the graphene. Scanning electron microscopy (SEM) imaging of the transferred graphene film was performed to determine the surface film quality following transfer, shown in Fig. 4.13b. Although there are small topological variations, such as bumps and wrinkles created during the transfer process, we observe no detrimental defects (such as holes or tears) in the graphene film. As demonstrated in depletion curves shown in Fig. 4.14b-c, graphene films transferred onto ODTS modified substrates exhibit a Dirac-point voltage ~ 22 Vg. This allows greater sensitivity while gating for modulation experiments.

Graphene Device Fabrication Process

a)

1. Wafer Cleaned In Hot Piranha

2. ODTS SAM Deposited On Surface

3. Graphene Transffered Onto ODTS SAM

Optional Bottom Side Doping with BI

4. Electrodes Deposited On Device

Scanning Electron Microscopy

b)

←Au

400 um
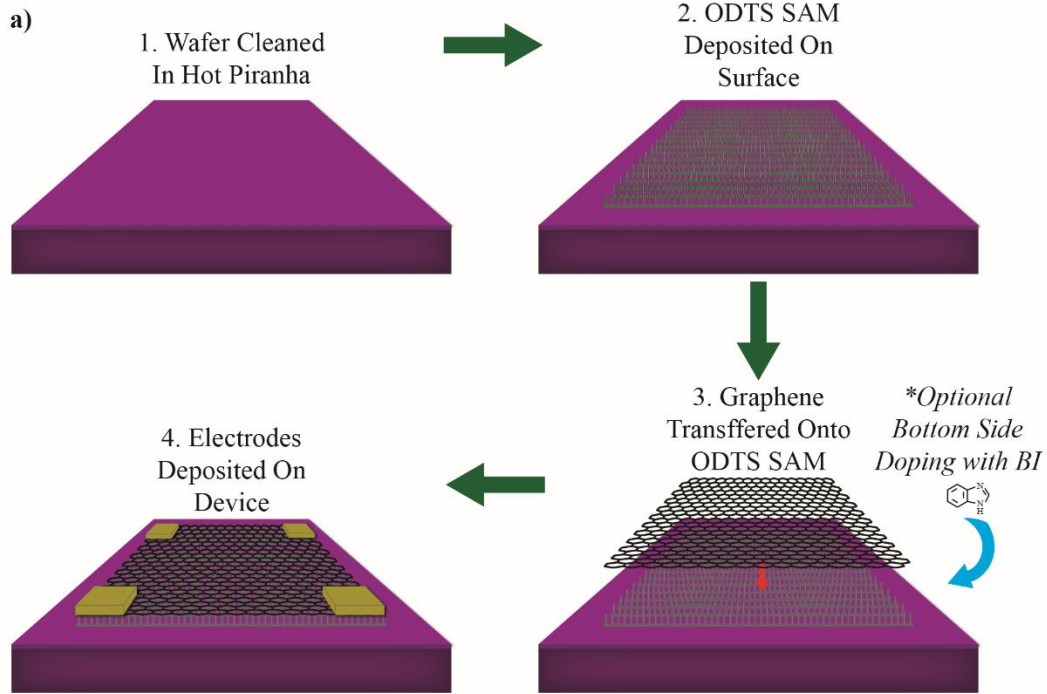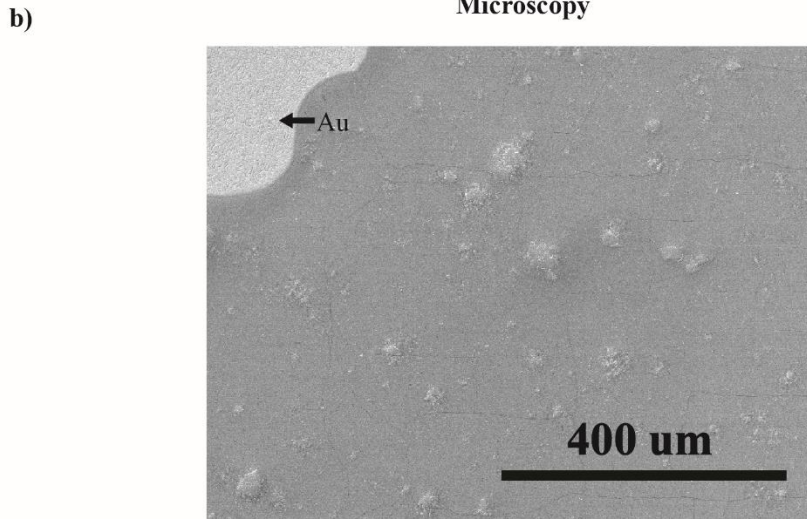
Figure 4.13: a) Diagram of graphene transfer onto ODTS SAM. First a SiO$_2$ on high-resistivity Si substrate is cleaned in hot piranha solution. This step assists in the vacuum deposition of the ODTS SAM on the substrate surface. Graphene is then transferred using typical wet transfer protocol, with optional BI doping. After the graphene film is transferred and cleaned, electrodes are deposited for electrical measurement. b) SEM image of transferred graphene film. A gold electrode is seen in the top left corner, along with topological bumps and wrinkles from the transfer process.

Across the measured frequency range, the SAM does not significantly affect the THz absorption. The resulting air/graphene/substrate structure shown in Fig. 4.13a was used for THz transmission measurements with the THz beam incident on the graphene side first.
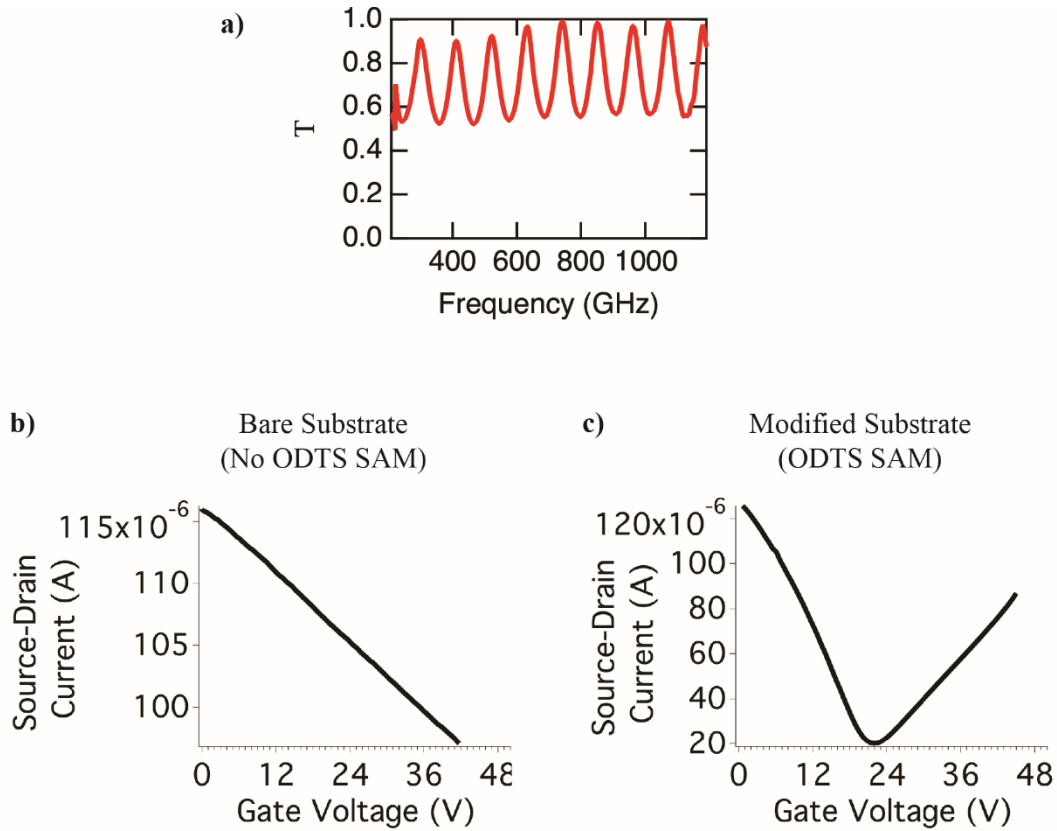
Figure 4.14: a) Transmittance versus frequency of SAM layer on substrate. b) Depletion curve of graphene film on standard substrate without ODTS SAM modification. c) Depletion curve of graphene film on substrate with ODTS SAM modification. The Dirac-point voltage on ODTS SAM modified substrates is ~ 22 Vg, and improves the transconductance.

Fig. 4.14a shows the transmittance versus frequency of a substrate with a SAM modified surface. The THz transmittance (half-wave resonance) nearly reaches unity across the measured frequency range. In the most extreme circumstance, the transmittance is not completely lossless, but is nevertheless over 90%. This value corresponds to a sheet resistance value of ~ 3500 Ω/sq. Because the SAM resistance

is in parallel with the graphene film, the large resistance of the SAM has limited effect when the graphene sheet resistance is low, and results in a difference of less than 15%. The influence of the SAM plays a more significant role when the graphene sheet resistance is comparable (such as when the graphene film is gated to $\sim$ 2000 Ω/sq in Fig. 4.15f). This small absorption contribution from the SAM may potentially explain why the data point (d) deviates from the theory line in Fig. 58c.

When gating the graphene to the charge neutral point (CNP) without the use of a SAM, large voltages (> 50 V) must be applied to the high resistivity silicon layer. Utilization of the SAM layer provides significant improvement of the transconductance of the graphene film, and a smaller operating voltage window, Fig. 51b-c. The depletion curve shown in Fig. 4.15b, shows a CNP at $\sim$ 22 V, and indicates slight p-doping of the graphene film. We performed a series of THz transmission measurements on these devices for a variety of sheet resistance values, shown in Fig. 4.15d-h.
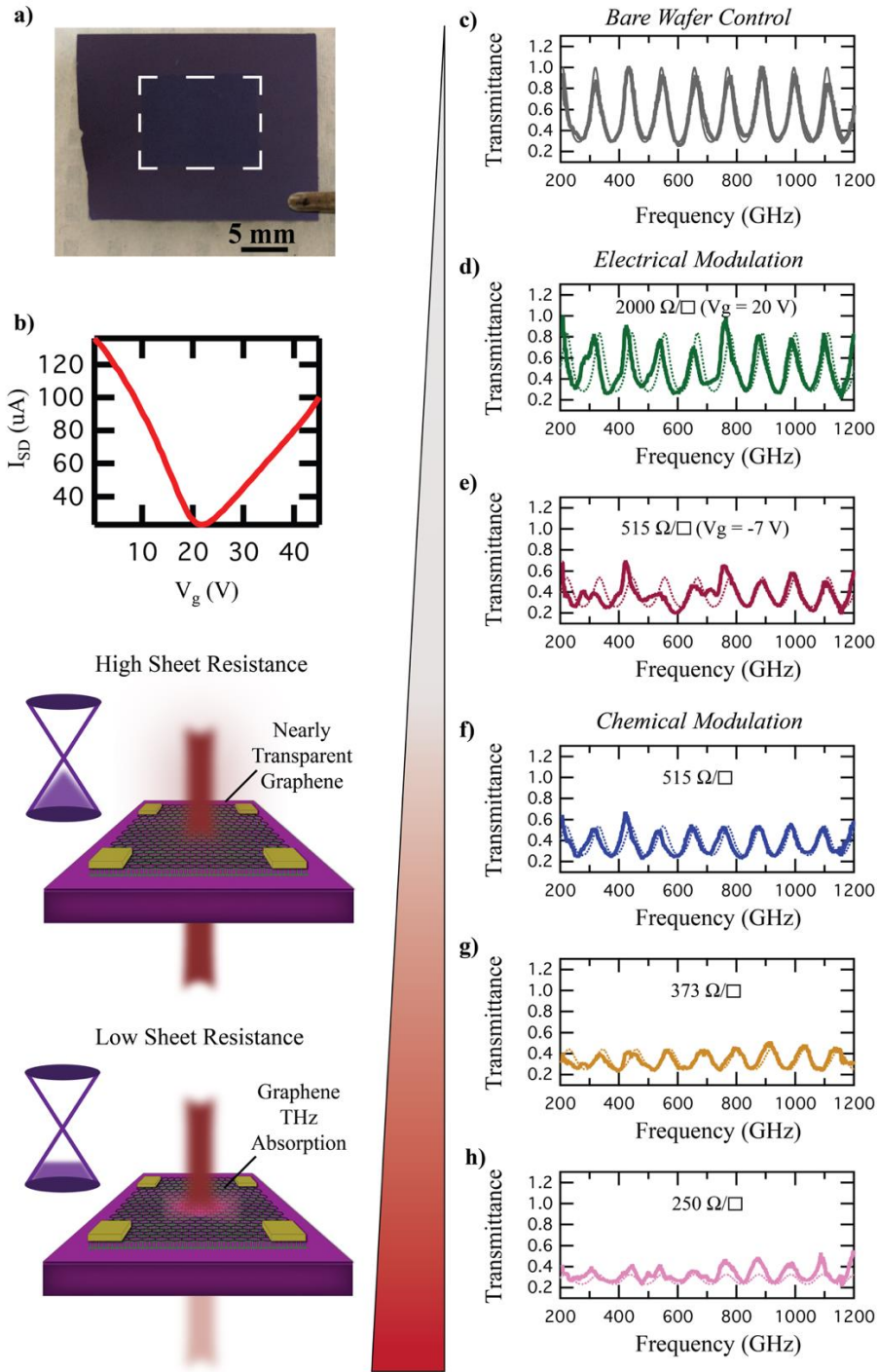
Figure 4.15: a) Optical photograph of graphene transferred onto ODTS modified oxide on high-resistivity silicon substrate. The scale bar is ~ 5mm. b) Source-drain current versus gate voltage for typical graphene on ODTS SAM device. The charge neutral point is ≈ 22 V. c) Transmittance versus frequency data acquired for a control sample (bare high-resistivity silicon substrate with no graphene). d-e) Transmittance versus frequency data for a graphene sample gated at 20 V, and -7 V. f-h) Transmittance versus frequency for 3 devices after chemical doping to modify the zero-bias sheet resistance. The expected transmittance values assuming the DC conductance as the AC contribution (assuming negligible susceptance) are plotted as dotted lines.

In order to de-convolve the etalon effect, the broadband transmission through a bare high-resistivity silicon substrate (without graphene) is first measured as a control. The multiple interference peaks of transmission around $\approx$ 1.0, Fig. 4.15c, confirm the low-loss nature of the bare substrate. Upon the addition of a monolayer sheet of graphene on the ODTS SAM buffer layer (and, when applying a voltage on the silicon substrate near the V_{CNP} ($\approx$ 20 V) as shown in Fig. 4.15d), the graphene film behaves as a nearly transparent film (sheet resistance $\approx$ 2 kΩ/□), as the amplitudes of the transmission peaks approach unity. The theoretical graphene-on-Si etalon transmittance vs frequency curves, calculated for an AC admittance that is purely real (susceptance equal to zero) and equal to the measured DC conductance, are plotted as dotted lines for comparison, and generally agree with the measured values. This is clearly in the transmission-dominating regime, as the presence of the graphene has little effect on the THz transmission through the sample.

We next demonstrate the ability to electrically tune to the absorption-dominating regime. By applying -7 V, the graphene DC sheet resistance is decreased to $\approx$ 515 Ω/□, and we observe considerably decreased maxima in the transmission peaks, Fig. 4.15e. Despite the fact that the gate voltage drop across the graphene film is small compared to the high resistivity silicon substrate, consistent with the I-V curve (Fig. 4.15b), our device still enables significant control of the single-layer graphene sheet resistance, which results in a large transmittance variation of the incident THz radiation. The gate-modified transmittance peak values are plotted together with the IV characteristics in Fig. 4.16a for an additional device. Gate

leakage through the oxide and ODTS SAM ($[10^{-5}]$ A) was observed at voltages beyond this range, and hence, gate voltages were restricted to -7 V to +45 V. Across the broadband frequency range measured, the transmittance variation at the peaks can be used to define a depth of modulation (DoM) (relevant to the use as a spatial-light modulator), defined as $(T_{High}-T_{Low})/T_{High}$. The DoM is substantial, with a maximum value of $\approx 52\%$ at the ~ 330 GHz peak (Fig. 4.16b).

The broadband transmittance was measured for a single device at various gate voltages to test the performance as a THz modulator. The peak transmittance (centered at ~ 694 GHz) versus gate voltage is plotted on the same chart as the device resistance, shown below. On a different device (best), the depth of modulation (using +20 V_g and -7 V_g) versus frequency is displayed, and shows frequency variation of the DoM, with a maximum value of $\sim 52\%$. Variations may arise from inhomogeneous gating using the high resistivity silicon substrate. The use of a high resistivity substrate limits the device switching speed. Experimentally, we measured a modulation frequency of < 2 Hz.
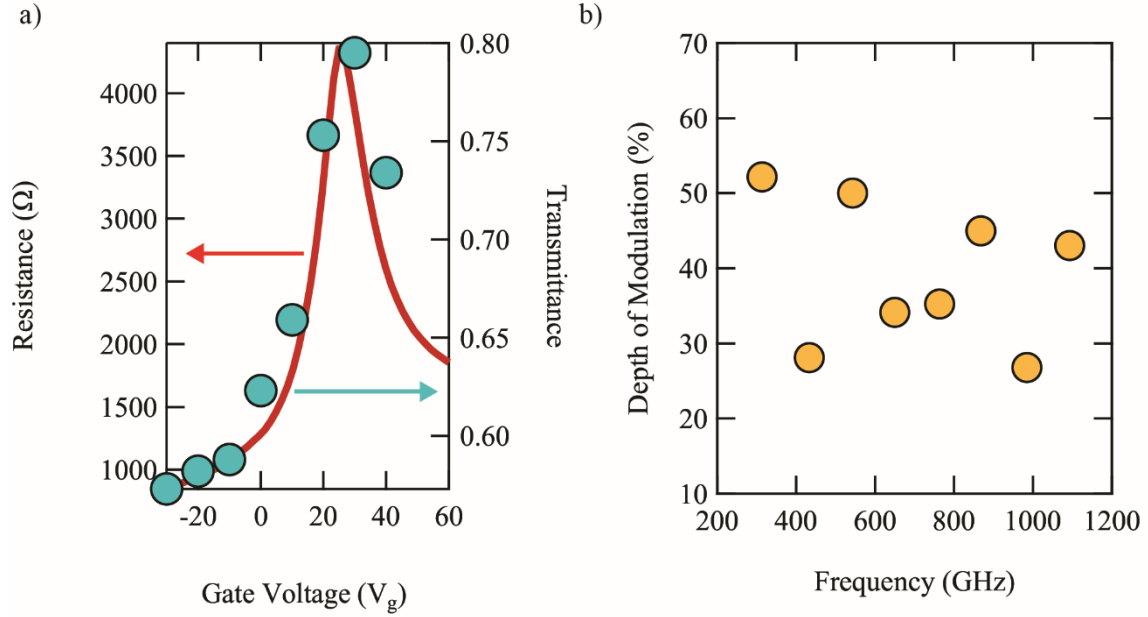
Figure 4.16: a) The resistance versus gate voltage is plotted with the voltage dependent peak transmittance value (located at ~ 694 GHz). b) The depth of modulation of the transmittance peaks for a device under -7 and 20 Vg gate biasing. The maximum value (~ 52%) occurs around ~ 320 GHz, although significant modulation is seen across the broadband frequency range measured.

T_{max} is the maximum transmittance value at a peak of the spectra. Then the transmission variation is given by,

$$\frac{dT_{max}}{T_{max}} = -2Z_0\sigma_g \frac{1}{\varepsilon_s + \sigma_g Z_0 + 1} \frac{d\sigma_g}{\sigma_g}$$

(29)

where Z_0=377 Ω is the impedance of free space, ε_s is the dielectric constant of the Si substrate and σ_g is the conductance of graphene film. Assuming the device is mounted on a silicon substrate ($\varepsilon_s \approx 11.66$), the room temperature values from Banzerus et. al[118], (mobility ~ 145,000 cm²/Vs) approaches 100% depth of modulation with only ~10 V on the gate.

For a simple, unpatterned device geometry, consisting of only one monolayer, this is the largest transmittance variation that has been reported to date for a graphene-based modulator, to the best of our knowledge[19,101,111,114,115]. A 52%

DoM is comparable to other patterned graphene devices such as extraordinary optical transmission (EOT) structures[21] and periodic arrays of graphene nanodisks[119]. Compared to patterned device geometries, which usually create frequency-or-polarization-dependent behavior, our device structure (which does not require any lithography) allows for useful THz modulation over 1 THz of frequency range with polarization independence. This result was independently confirmed in two different labs (Fig. 4.17).
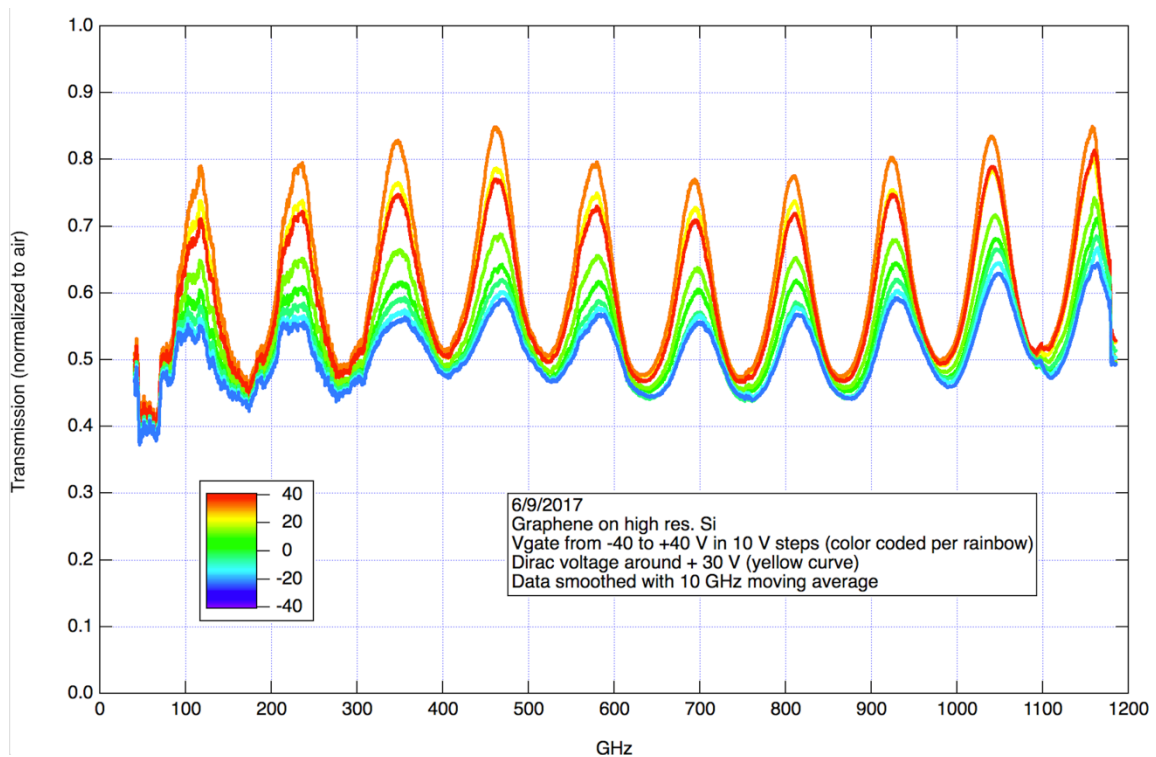
Figure 4.17: Data independently confirming the broadband transmittance amplitude modulating as the graphene sheet resistance is varied (here, by applying a gate voltage on the Si layer) in a different lab using a Toptica Terascan frequency-domain THz spectrometer.

Fig. 4.21a shows the inferred frequency dependent conductance varying from much less than $(Z_0)^{-1}$ (green curve, V_g = +20 V, 10x less than $(Z_0)^{-1}$), to approximately equal to $(Z_0)^{-1}$ (red curve, V_G = -7 V), and clearly demonstrates electrical tuning from the transmission to absorption-dominating regimes. In order

to achieve the necessary sheet conductance values near maximum absorption, and beyond $(Z_0)^{-1}$, we utilized chemical (rather than electrical) tuning. We intentionally dope graphene films to have low sheet resistance in the zero-bias state (to mitigate inconsistencies that may arise from the inhomogeneous gating using a high resistivity substrate, and to ensure no gate leakage occurs) by using benzimidazole (BI) dissolved into the copper etching solution during graphene transfer[84].

We measured the depletion curve to investigate the effects of doping on the electrical properties of the graphene films. Fig. 4.18 shows the depletion curves of samples with and without BI doping on an ODTS substrate. After doping, the Dirac point voltage is subsequently shifted to > 48 Vg, indicative that the graphene film becomes hole doped. We found that with the use of BI doping, we could achieve a (zero gate biased) DC sheet resistance below the impedance of free-space. Even with BI doping, the sheet resistance values would vary from sample to sample. The sheet resistance differences from sample to sample could be explained by spatial variations in τ and E_F after doping.
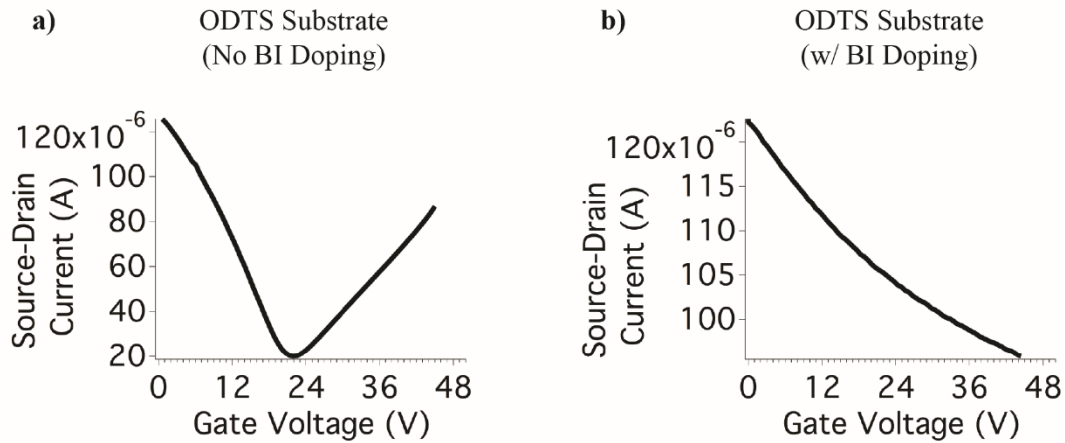
Figure 4.18: Depletion curve data for two samples, with and without BI doping on ODTS substrates. Following doping with BI, the Dirac-point voltage becomes > 48 Vg.

To further investigate the effects of doping graphene, we employed Raman spectroscopy. Raman spectroscopy was performed using a Renishaw Invia Spectrometer with a 532 nm laser. Raman mapping was performed using the Streamline High Resolution (HR) mapping function over a 3 x 3 mm area with 60 um step size. The peak analysis and fitting was performed using the Wire 3.6 Renishaw software package. Mapping images are processed using Igor 6 plotting software.
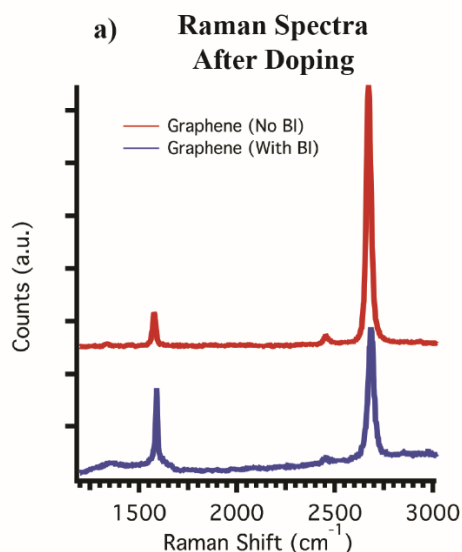
Figure 4.19: Representative Raman spectra for samples with and without BI doping on an ODTS SAM modified substrate. Before doping, the [I]2D/[I]G ratio is much larger than after doping. Also the peak position of the g-peak becomes blue-shifted after doping.

Fig. 4.19 shows representative Raman spectra of graphene samples with and without BI doping during transfer. Notably, after the addition of BI doping, we observe a decrease in the intensity ratio, [I]2D/[I]G. The [I]2D/[I]G ratio is known to decrease when both the scattering and Fermi energy of the graphene film increase in magnitude[43,58,61], and thus provides a convenient parameter to assess the BI doping of graphene films. Fig. 4.20 shows the Raman mapping histograms and images of the [I]2D/[I]G with and without BI doping. We confirm the general trend

(lower average in histrogram) of decreased [I]2D/[I]G ratio, but we also observe spatial variance of the graphene film after doping. This supports our belief that after doping, the graphene sheet resistance is not dominated merely by changes in E_F, but instead, by a combination of both E_F and τ. The extracted AC conductivity parameters (outlined below) further support this hypothesis, since under chemical doping, the lowest sheet resistance devices are not the largest E_F, but instead, a combination of moderate E_F and long τ.
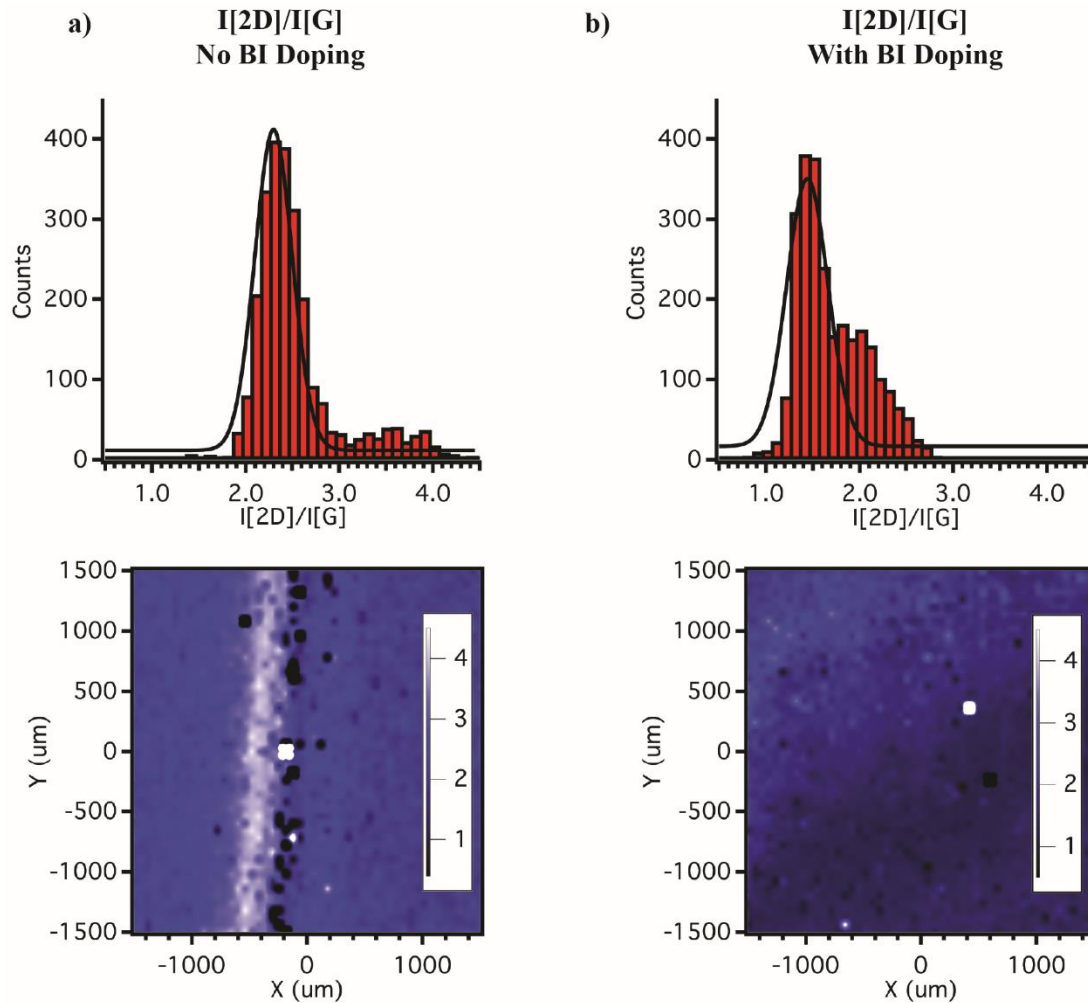
Figure 4.20: Histograms and spatial mapping of [I]2D/[I]G ratio for two samples, with and without BI doping. After doping, the [I]2D/[I]G ratio decreases across the sample.

Fig. 4.15f-h shows the broadband transmittance versus frequency for three graphene films having zero-bias DC sheet resistances of 515, 373, and 250 $\Omega/\square$ respectively. Similar to the electrical modulation, we observe a steady decrease in the THz transmittance peaks. The lowest sheet resistance is clearly less than 377 Ω and the trend of reduced transmission with reduced sheet resistance is observed over the entire measurement band.
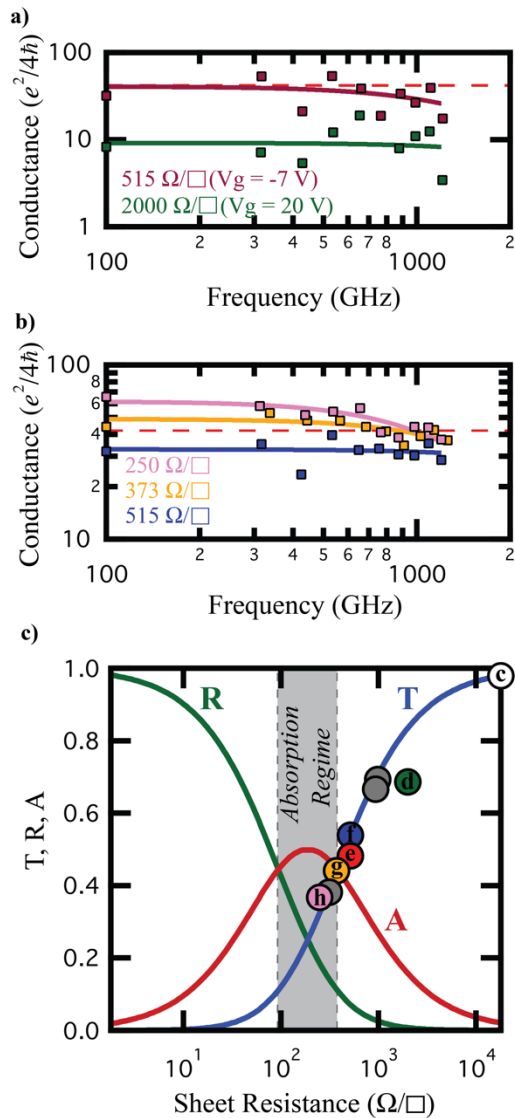
Figure 4.21: a-b) The AC conductance values calculated by fitting the measured transmittance peaks for both electrically and chemically modified devices from Fig. 3 are plotted as squares. Drude model trends estimated from the frequency dependent AC conductance data are plotted as solid lines. **c)** The measured transmittance peak values (at ~ 655 GHz) are plotted as a function of sheet resistance. Colored (labeled) circles represent data from devices shown above, grey circles are from devices measured, but not displayed in Fig. 4.15, and the white circle represents the control sample. The theoretical transmittance, absorbance, and reflectance values calculated from the half-wave resonance case for a device on a substrate are plotted as solid lines. The transmittance value becomes less than the absorbance value at sheet resistance values < 377 $\Omega/\square$ marking the beginning of the absorption regime.

The measured transmission spectra can be used to determine the AC sheet

conductance, using the bare silicon control sample as nearly lossless "calibration"[19]

(although, it is noted that the transmission peaks do not necessarily remain at a fixed frequency when covered by a thin film). For devices covered by a graphene film, each transmittance peak is fitted to yield a AC admittance (real conductance and imaginary susceptance) value; the measured DC conductance and the estimated THz conductance are then fitted according to equations (2) and (3) to estimate E_F and τ for each device.

Device Measured	DC Sheet Resistance	Modulation Type	τ (fs)	E_F (meV)
Fig. 3d	~ 2000 Ω/sq	Electrical (+20 V_g)	44	105
Fig. 3e	~ 515 Ω/sq	Electrical (-7 V_g)	99	209
Fig. 3f	~ 515 Ω/sq	Chemical Doping	28	583
Fig. 3g	~ 373 Ω/sq	Chemical Doping	74	339
Fig. 3h	~ 250 Ω/sq	Chemical Doping	111	284

Table 4.1: Table of DC resistance, and the extracted E_F and τ values for both electrical and chemical modulation of devices measured in the main text.

The calculated peak conductance values are shown in Fig. 4.21a-b, with a dotted red line showing the 377 Ω threshold. The predicted Drude conductance using the estimated E_F and τ is plotted as a solid line, and closely matches the measured DC value (shown on the y-axis). Fig. 4.22 summarizes in a graphical representation our achievement crossing the free-space impedance threshold within the mm-wave and THz frequency ranges, and compares our data to previous measurements in the literature. In this work, the frequency domain measurement is especially broad (spanning the sub-THz regime), and the optical conductance and THz absorption of the graphene film are remarkably large for one atomic layer. Table 1 shows the extracted Drude parameters, E_F and τ, for measured devices. Notably, the values of E_F are moderate, while the values of τ can be large (> 100 fs), and stress the importance of engineering τ, as initially outlined in the device design

plots in Fig. 4.12c-d. These figures clearly demonstrate our ability to tune the sheet resistance of monolayer graphene, either electrically or chemically, from well above to below the characteristic impedance of free-space.

We now discuss the relationship of this work to prior work on graphene in the THz domain. Fig. 4.22 shows the range of conductance versus frequency for other monolayer graphene devices previously measured in the literature. Each trend line is plotted using equations (2) and (3), using data points supplied from each reference. The labeled and colored hashed (solid) regions (lines) indicate frequency domain measurements, whereas the transparent grey regions (lines) are for time-domain systems. The frequency range measured for this paper is one of the broadest (with 500 MHz spectral resolution) investigating graphene-THz coupling, complemented by an extensive range of conductance values, including the achievement of surpassing the free-space impedance threshold.
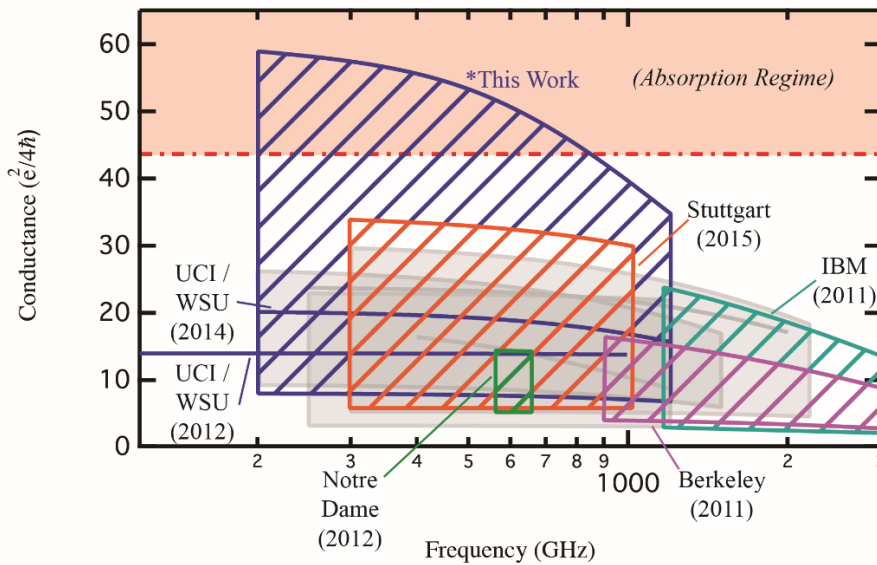
Figure 4.22: Conductance versus frequency range of other graphene devices in the literature. Hashed regions indicate frequency domain systems, while the transparent grey regions show time-domain measurements.

120

The table below shows both the conductance range and the frequency range of the references used in Fig. 4.22. The optical conductance values are those measured and reported from each reference, and τ and E_F are estimated to reflect this value. In reference 8, τ is defined as $\tau = \hbar/\Gamma$, where τ is the scattering time, $\hbar$ is the Planck constant, and Γ is the phenomenological scattering parameter, whereas in our calculations, τ is defined as, $\tau = \hbar/2\Gamma$.

Reference	Frequency Range (GHz)	Measurement Type	Optical Conductance Range ($e^2/4\hbar$)	Estimated to Equal Optical Conductivity	
				τ (fs)	E_F (meV)
Yan et al.	1190 -	Frequency Domain (FTIR)	23.7	*23	560
Horng et al.	900 -	Frequency Domain (FTIR)	1.9 – 16.09	55	170
Rouhi et al.	100 - 1000	Frequency Domain	14.07	50	150
Zhang et al.	200 -1200	Frequency Domain	20.63	72	150
Sensale – Rodriguez et al.	560 - 660	Frequency Domain	3.28 - 14.8	50	153
Ren et al.	100 - 2200	Time Domain	5 - 27.41	50	252
Cervertti et al.	300 - 1000	Frequency Domain	3.94 - 36.18	123	157
Min Woo et al.	250 - 2100	Time Domain	23.87	50	254
Maeng et al.	200 - 1500	Time Domain	5 - 27.09	48.8	295
Buron et al.	250 - 1200	Time Domain	3.2 - 23.02	50	246
Mics et al.	400 - 1200	Time Domain	19.73	140	70

Table 4.2: Table of frequency range, measurement domain, and achieved conductance range for each reference used in Supplemental Fig. 13.

We next focus on our more quantitative demonstration of the relationship between the transmittance and the sheet resistance.

We plot in Fig. 4.21c the predicted transmission (blue line), reflection (green line), and absorption (red line) for a graphene film as a function of sheet resistance for a film mounted on a silicon substrate, at half-wave resonance satisfying the condition $\mathbf{k}L=N\pi$. At half-wave resonance, the free-space and etalon effect give the same predicted T, R, A vs. sheet resistance (Fig. 4.16). We also show the measured transmittance peak (centered around ~ 655 GHz) values (color points are from devices measured in Fig. 4.15, grey points are for devices measured during this

work, but not displayed in Fig. 4.15). The 377 Ω vertical dotted-line indicates the characteristic impedance of free-space threshold, and marks the start of the absorption regime, where the fractional absorbance ($\sim$ 0.44) of the THz radiation by the graphene film becomes greater than the fractional transmittance (and reflectance)[106]. Here, we have realized the crossover from the transmission regime, and have measured correspondingly small transmittance values for devices within the absorption regime. For our best single-layer device of $\approx$ 250 Ω/□, the value of the graphene film absorbance is calculated to be $\approx$ 48.6%: approaching the theoretical limit of 50% (for normal incidence on graphene side first).

Instead of designing the single-layer sheet resistance to cross into the absorption-dominating regime, previous experiments for unpatterned graphene devices boosted low absorbance by the addition of multilayers[120–123], or by suppressing the transmission channel[124] using double-pass/reflection/"Salisbury screen" geometries[110,113]. Other thin film (multilayer) materials have also demonstrated remarkable control of absorption by controlling film thickness, such as niobium nitride (NbN)[125–127] and indium tin oxide (ITO)[104]. Here, our experiments show that exceptionally large, near maximum, absorption can be reached in the thickness limit of one single-layer of graphene.

Impedance matching to the free-space threshold using a double-pass, reflection mode geometry could achieve 100% absorption[122,128], and may further enhance the single-layer reflection DoM[110,129]. Pertaining to designing devices that operate in transmission (such as the work performed here), the suspended film and Woltersdorff equations[106] stand as the ideal situation for broadband absorption.

Using the transmission line model for a film on a substrate, as the substrate index of refraction value approaches $n = 1$, or the substrate thickness approaches, $L = 0$, the amplitudes of the Fabry-Perot fringes decrease, and the widths of the fringes increase (as calculated values converge toward the suspended film/Woltersdorff equations for all frequencies). Although it is shown by calculation[107] that the (quarter-wave resonance) absorption can be greater than 50% if the THz beam is incident on the substrate side first, this geometry does not easily allow for use as a transmission-mode modulator, because changes in the sheet resistance have less effect on the transmittance compared to the geometry employed in our experiments. Nevertheless, it could still be useful as a reflection-mode device, however the major challenge of engineering low sheet resistance values remains, since absorption greater than 80% in this geometry requires sheet resistance values of less than 100 $\Omega/\square$.

We were able to achieve a large transmission DoM by improving the transconductance (allowing the sheet resistance of a single device to span a broad range) of the graphene on ODTS SAM layer. The high quality, large-domain graphene films on SAM used here were confirmed via Raman mapping[43,61] and suggest that substrate modification improves the sheet resistance by improving mobility at high carrier density[58,130] (Fig. 4.23).
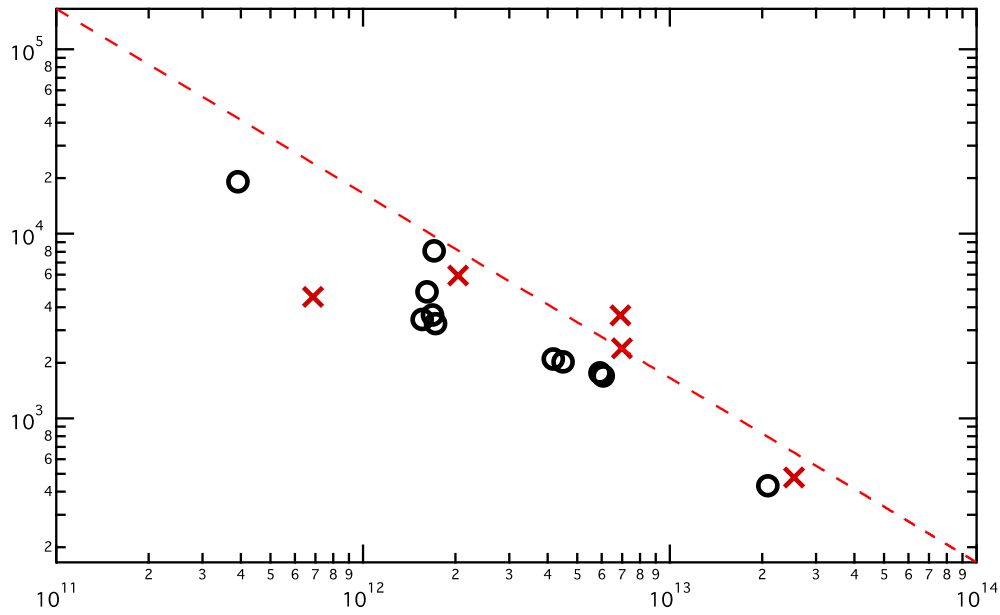
Figure 4.23: The mobility versus carrier density calculated[131] **using the scattering time and optical conductivity values from this work, and those reported in Supplementary Table 2. The dotted line shows the 377 Ω threshold.**

Although other materials can exhibit tunable conductance such as vanadium dioxide (VO_2)[109,132,133], NbN[125–127], ITO[104], metal thin films, or even multilayer graphite, the conductance of monolayer graphene can be easily tuned via external voltages due to the extremely high mobility. For high frequency applications, the mobility of single-layer graphene is superior to bilayer (multilayer) graphene[134], and other semiconducting materials[129,135], but fabrication remains a challenge for large-area devices which precludes electronically tunable devices operating at very low sheet resistance (even in the simple case of EM incidence on the substrate side first). A combination of substrate modification to improve mobility with techniques such as electrolyte gating[121], or device integration[115] could yield electrically controlled devices with high modulation frequency and low operation voltage.

Additional improvements in large-area (mm-scale) graphene synthesis and transfer will foster better control from the transmission-to-absorption regimes (towards the reflection-dominating regime), as recent reports on large-area CVD graphene demonstrate mobility values as large as 350,000 ($cm^2V^{-1}s^{-1}$) with sheet resistance spanning $\sim (e^2/4\hbar$ - $500e^2/4\hbar)$ at DC applying only ~ 5 V_g[118]. Our studies reveal the opportunity for a device based on the tunable electronic properties, without complicated fabrication steps required for other THz modulation schemes such as metamaterials[21,119,136], nanophotonic resonators[137], thin film thickness tuning[104,109,125–127], or materials with switchable metal-to-insulator phase transitions[109,132,133].

We have demonstrated that the control of the large-area graphene DC sheet resistance enables the tuning, either electrically or chemically, from the transmission to absorption-dominating regimes at mm-wave to THz frequencies. This could have wide ranging application in the tunable and controllable manipulation of mm-wave and THz light, including, for example, gate tunable THz modulators, electronically steerable phased array antennas and radar, and tunable variable focus lenses and cones. However, while we have clearly demonstrated a single-layer tuned from the transmission to absorption regimes (the grey shaded region in Fig. 4.21c where A > T, R), we have not pushed well below the inflection point between poor to excellent conductor (the lower bound in Fig. 4.21c where R > T, A). Future work with increased conductivity (e.g. by improved materials synthesis, using other 2D materials other than graphene, etc) may enable complete

tuning from strong transmitter, to strong absorber, to strong reflector, and would enable new technologies to manipulate EM radiation in powerful ways.

The effective thickness of each device is held constant during calculation and fitting using the values listed above. The peak-to peak spacing of each transmittance peak of all devices were analyzed, and the average values are also listed in Table 3. Small deviations in the peak-to-peak spacing are apparent. This variation could be due to the common issue collimating the THz beam, where, when the device is not absolutely parallel leads to a spread in the effective substrate thickness. Nonetheless, the peak-to peak spacing agrees with the different effective thickness from the various device. Furthermore, the instrument used is a fiber-based frequency domain photomixing spectrometer; insertion of a sample into the THz beam may shift the interference fringes on the THz arm, leading to a slight off-balance with respect to the optical arm. Therefore, some irregular frequency points in the measured transmittance may be contributed by "instrument drift". To mitigate the experimental uncertainty from both the instrument drift and beam collimation, post experimental data analysis was employed. Here, we performed fitting to every individual interference pattern around every peak which contains up to hundreds of frequency-transmission points. From the extracted conductance at those individual peaks, we obtain E_F and τ with the Drude model, and compare the calculated DC conductance to the measured DC value, as seen in Fig. 4.21a-b. Here, we find that the two values agree with each other, and supports the reliability of our data.

Device Measured	Fig. 3c	Fig. 3d	Fig. 3e	Fig. 3f	Fig. 3g	Fig. 3h
Thickness	395 μm	395 μm	395 μm	398 μm	382 μm	401 μm
Peak-to-peak Spacing	113.48 ± 1.51 GHz	112.04 ± 1.15 GHz	113.23 ± 3.55 GHz	110.74 ± 1.32 GHz	115.50 ± 2.88 GHz	109.64 ± 4.97 GHz

Table 4.3: Table of the effective thickness used for calculation for each device. Also listed are the peak-to-peak spacing averages of the experimental data for each device.

A Drude-like roll off is expected for frequencies greater than $1/\tau$, as the imaginary contributions become significant, especially when τ is long. During fitting of the measured transmittance peaks, both the real and imaginary contributions were calculated. However, when fitting for τ and E_F only the real contribution is used. Because the Kramers-Koenig relation relates the real and imaginary contributions, a fit on only the real yields valid results[19]. Fig. 4.24 shows the real and imaginary values calculated, and the calculated Drude trend from the (real part) fitted E_F and τ values for the best device of 250 Ω/sq. The predicted line generally agrees the measured conductance trend. Though the error of the imaginary fit is larger than that on the real part, this error can potentially be improved from a direct measurement of the phase. This would improve the fitting of τ, and would provide a more accurate range of the Drude-shaped roll off ($\omega \sim 1/\tau$). For our best device ($\sim$ 250 Ω/sq), the high frequency transmittance peaks start to deviate from the predicted trend (when using the measured DC sheet resistance as the real part, ignoring imaginary contributions), suggesting significant contributions from the imaginary. The frequency dependent amplitude deviation is generally not observed in other devices.
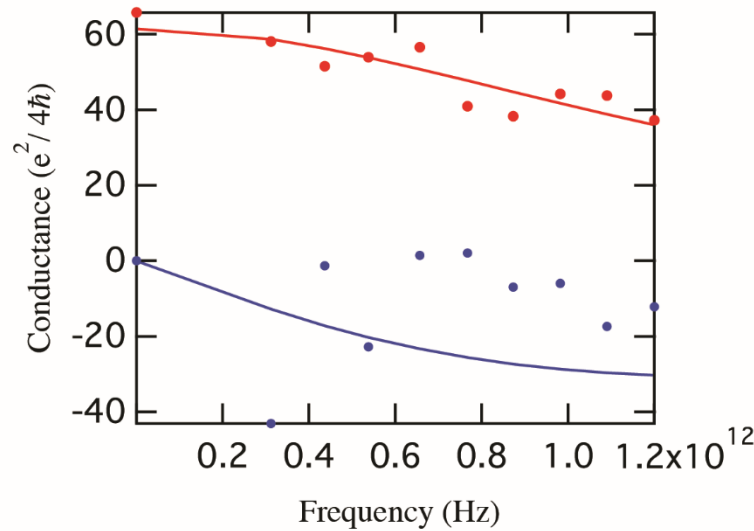
Figure 4.24: The real (red) and imaginary (blue) contributions of the AC admittance calculated by fitting the broadband transmittance data for the best device of 250 Ω/sq. Using the real values, the Drude parameters were calculated, and the Drude prediction is plotted as solid lines.

4.5 Graphene-THz for DNA Detection

The terahertz frequency regime could find new applications in biomolecular detection because of rotational and vibration resonances occurring within the THz band. We performed preliminary experiments to understand how GFETS might be a good candidate platform for biodetection. Specifically, we performed experiments on single stranded DNA and DNA origami. The GFET structure provides a platform for simultaneous electrical reading and THz signal on one device[138].

The GFET structure was operated with the backgate bias of 25 V from a low-noise power supply, and a drain-source constant-voltage bias of 0.1 V from a Keithley 2400 source meter. This backgate bias was chosen because of its proximity to the Dirac-point bias of ~30 V, which was attainable but only with a large degree of fluctuation in the drain-source current. The 25 V backgate bias creates a significant background electron sheet concentration in the graphene, and the V_{DS} is just high

enough to allow accurate measurement of the sheet conductance without excessive drift and 1/f noise. Because the graphene geometry between the S and D electrodes is approximately square (area ≈ 1 cm^2), the absolute DC sheet conductance is $G_{DC} \approx I_{DS}/V_{DS}$. For the specific GFET tested we measured an I_{DS} of 0.2132 mA, or sheet conductance of 2.132 mS. The corresponding background 101-GHz transmittance signal was $X_B = 0.8527$ V where the last digit is significant given the high SNR.

To validate the measurement technique and assess its accuracy, we used the backgate to induce a known-change in graphene DC sheet conductance and compare this with the derived change of the 101-GHz quantity. We applied backgate voltages of 30 V and 20 V to straddle the nominal +25 V and allow for mean-value estimation. The DC current values at the two gated voltages were 0.2017 and 0.2255 mA, respectively, corresponding to $\Delta G_{DC} = 0.0238$ mS. The lock-in signals for the same backgate voltages were 0.8661 and 0.8412 corresponding to a transmittance difference of 0.0292.

The biodetection protocol was to apply 13-mer single-stranded DNA solutions of three different molarities (0.01, 1.0, and 100 nM) sequential at 900-s intervals, starting with the 0.01 nM solution. A drop of each was placed directly on the graphene with a syringe, allowed to settle for 300 s, and then blown dry with an oil-free air gun. The Keithley-2400 DC current was recorded simultaneous with the THz transmitted signal via the output from the lock-in amplifier. The experimental results for DC current are shown in Fig. 4.25a where we see an initial value of 222 µA between ≈ 600 and 900 s, corresponding to a sheet conductance of 2.22 mS. Then a large fall in DC current occurs with the application of all three drops, and a

lesser fall upon blow drying 300 s later. Both effects are most pronounced with the 0.01 nM solution and become progressively weaker with the other two. The 1.0 and 100 nM drops have a significant effect in their aqueous form but little further change occurs upon drying. In all cases, however, at constant bias voltage the DNA decreases the DC sheet conductance of the graphene.
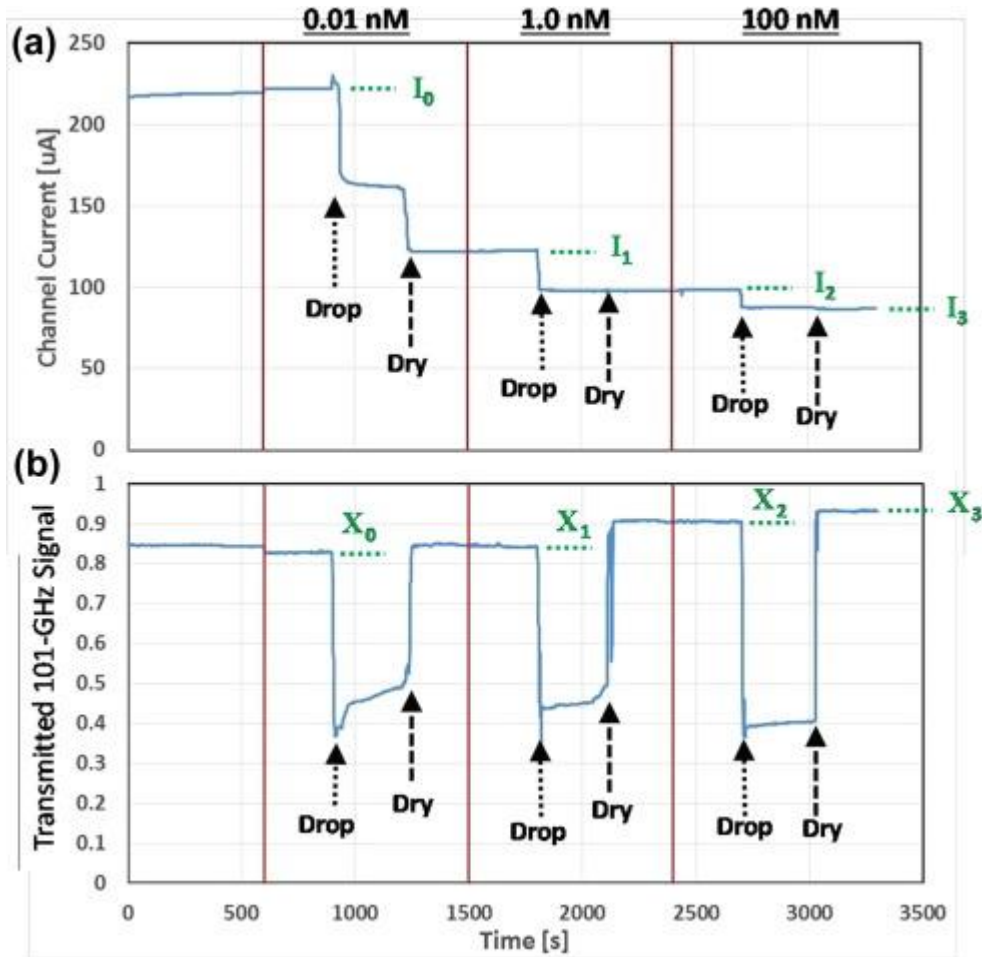
Figure 4.25: The effects of DNA on DC and 101-GHz signals.

Similarly, the transmitted THz signal plotted in Fig. 4.25b shows a large and precipitous decrease upon application of each drop of DNA solution. But unlike the DC current, the THz signal recovers to its previous level and goes slightly higher upon drying. The decrease and recovery can be explained by the strong absorption

coefficient of ~100 cm^{-1} for liquid water at 101-GHz. Although each drop is ~1 mm thick, they don't fill the entire beam footprint so the net attenuation caused by the liquid water is only ~3 dB. The increased post-dry transmission level compared to initial level suggests that the 101-GHz sheet conductance, like the DC conductance, is decreasing with each drop.

To quantify and compare the effects of the DNA on the DC and 101-GHz signals, we define and calculate relative sheet-conductance changes, ΔG_{DC} and ΔG_{RF}. A plot of these quantities vs molarity is displayed in Fig. 4.26 showing a monotonic increase in absolute value but a relatively small change in slope vs molarity, especially for the which changes less than 40% over the entire range. Interestingly, the ΔG_{RF} is always smaller in magnitude, especially for 0.01 nM where it is approximately 5-times lower. The reason for this is not yet understood.
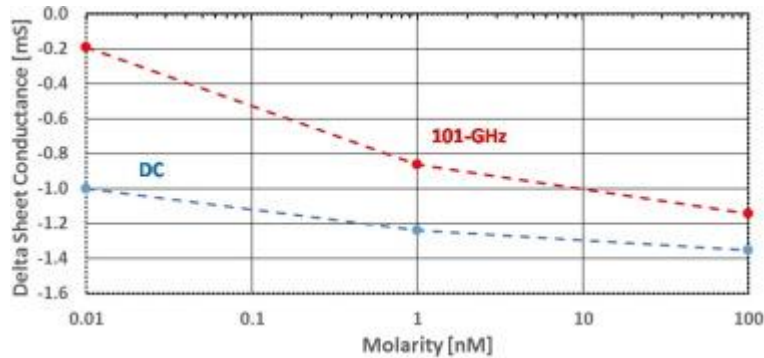
Figure 4.26: The variation of graphene sheet conductance vs molarity at DC and 101 GHz.

Finally, we can obtain a metric for the sensitivity of both methods by calculation of the post-detection signal-to-noise ratio (SNR). For the DC method, the SNR is just $\Delta I_{DC}/I_{rms}=|I_N-I_0|/I_{rms}$, where I_{rms} is the rms fluctuation dominated by a fast (white noise) component from the current source (Keithley 2400), and a slow (drift) component from the graphene. The noise was observed over a 600 s time

span with the graphene kept dry, and yielded $I_{rms} \approx 8.5 \times 10^{-7}$A. Thus, for the 1.0 nM case with $\Delta I_{DC} \approx 0.124$ mA we get an SNR of 145 [43.2 dB power SNR]. And for the 0.01 nM case with $\Delta I_{DC} \approx 0.010$ mA, the DC-SNR is 117 [41 dB]. The DC SNR drops only 2 dB for the two-order lower molarity, which bodes well for detecting even smaller concentrations but the nonlinearity precludes an extrapolation in that direction.

For the 101-GHz method the SNR is $\Delta X_{RF}/X_{rms} = |X_N - X_0|/X_{rms}$ where X_{rms} is the lock-in output noise which was attributable primarily to white-noise from the Schottky rectifier and the low noise amplifier (LNA). Observed over the same 600 s time window, and for the given modulation frequency (1 kHz) and integration time (0.3 ms), we measured $X_{rms} = 1.22$mV. Thus for the 1.0 nM case where $|X_1 - X_0| = 0.079$mV, the SNR = 64.6 [36.2 dB power SNR]. And for the 0.01 nM case where $|X_1 - X_0| = 0.017$mV, the SNR = 14.0 [23 dB]. The 101-GHz SNR drops 13 dB for the two-order lower molarity, more than the DC drop, but still nonlinear. Interestingly, the ~7 dB lower SNR for the 101-GHz signal is very close to the degree of sub-optimal performance. If the operating frequency was 112 instead of 101 GHz, and the DC sheet conductance was 1.0 mS instead of the 2.1 mS displayed by the present device, then the sensitivity factor would be $\approx 2\times$ higher and the post-detection SNR higher than the result reported here. In principle, this lower sheet conductance could be obtained by increasing the backgate voltage, but even 50 V only reduced it to about 1.5 mS and the drain-source current was noticeably unstable at this point. Alternately, one should get ~3 dB improvement in SNR by

starting with a thicker Si substrate (435 μm) for which the first non-zero resonance would occur at 101 instead of 112 GHz.

We also investigated the use of graphene as a platform for sensing using DNA origami. The original goal was to use "tiles" of DNA origami to make self-assembled nanowires, with each tile of origami specifically designed to sense a particular molecule by way of aptamer functionalization. In this approach, highly sensitive multiplexed detection could be performed with graphene as the electrical platform. We first aimed to understand the interaction of the DNA origami tiles with the graphene substrate, as both materials are expected to be influenced by π–π interactions.

CVD graphene was transferred onto mica following the standard wet transfer procedure, utilizing a poly(methyl methacrylate) (PMMA) coated graphene layer followed by rinsing in acetone and annealing[7]. Annealing under low pressure and elevated temperature is necessary to remove most of the PMMA from the surface of graphene but presents the possibility of damaging the mica surface with the loss of intercalated water. However, mica was observed by AFM to maintain its flat surface after annealing at 400℃. The resulting sheets of graphene deposited on mica were well-formed with some contamination and structural defects detected by Raman spectroscopy. Graphene exhibits two main features in Raman spectra for visible irradiation (532 nm) namely the G (~1583 cm^{-1}) and 2D (~2685 cm^{-1}) bands[43]. Although it has been demonstrated that the position of the G band can be a useful indicator of graphene doping[43,61], interpreting variations in the G band position across the graphene surface due to the interaction of DNA is non-trivial. This is due

largely to surface changes, including the possibility of delamination from the substrate, during deposition, and is currently being evaluated as an additional metric for monitoring DNA origami adsorption.

DNA origami solutions were prepared by annealing M13mp18 plasmid with commercially available synthetic oligonucleotide "staple" strands in 1X Tris-acetate-EDTA (TAE) buffer containing 12.5 mM $MgCl_2$ (origami buffer) slowly from 90 to 20 °C over a 13 h period. The freshly formed origami were then purified with centrifuge membrane columns to remove the excess staple strands that are used to promote high yield origami formation from the plasmid starting material. The removal of excess staple strands is required, as short ssDNA molecules will readily coat and passivate the graphene surface, preventing observation of the direct interaction of the origami constructs with the bare graphene surface.

Purified origami (8 μL, 1 nM) was adsorbed onto the graphene/mica surface by drop coating with a 1 minute incubation at room temperature before a brief rinse with 18 MΩ Millipore water (40 μL) and rapid drying with a stream of nitrogen.

AFM imaging revealed the surface to contain regions of thin strips of graphene and tears within larger graphene sheets, which exposed the underlying mica surface, Fig. 4.27 – 4.28. These areas provided a unique opportunity to visualize DNA origami on both graphene and mica in the same image. Samples were observed, using AFM, in three conditions, after initial adsorption, after rinsing, and in solution phase. These three conditions were chosen in order to ensure the washing/ drying process was not significantly affecting the apparent degradation of the origami constructs. The same phenomenon, complete disintegration of the

origami upon adsorption to graphene, was displayed under all three conditions, over numerous replicates, while the structures that adsorbed onto mica displayed well-formed morphologies.

Fig. 4.27 – 4.28 show AFM images taken after depositing purified cross-shaped DNA origami onto graphene-mica substrates. Additional AFM images of different sample preparations are available in the supporting information. The AFM images show "ribbons" of graphene, defects formed during deposition and washing of the sample, laying on top of mica with cross-shaped origami deposited on both materials. The complete loss of origami structural definition on the graphene-mica regions of the sample is in stark contrast to the expansion and partial deformation observed for origami adsorbed on HOPG[139].
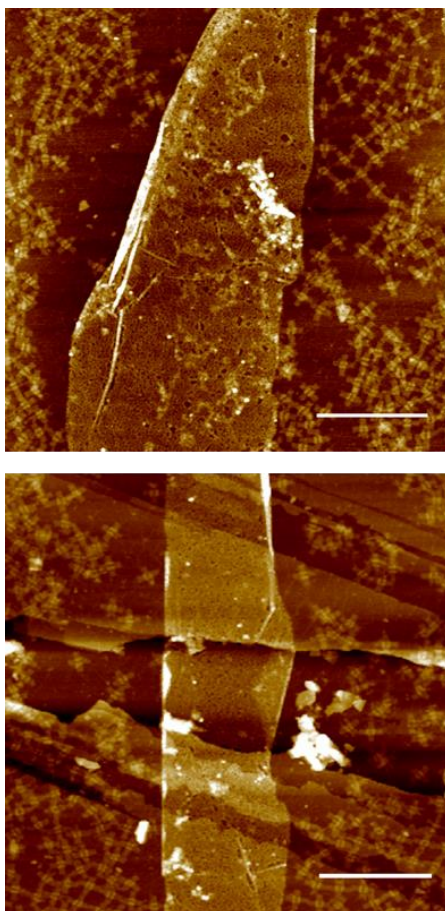
Figure 4.27: AFM images of cross-shaped DNA origami deposited on graphene-mica substrate. Scale bars, 500 nm (lateral), 10 nm (height scale).
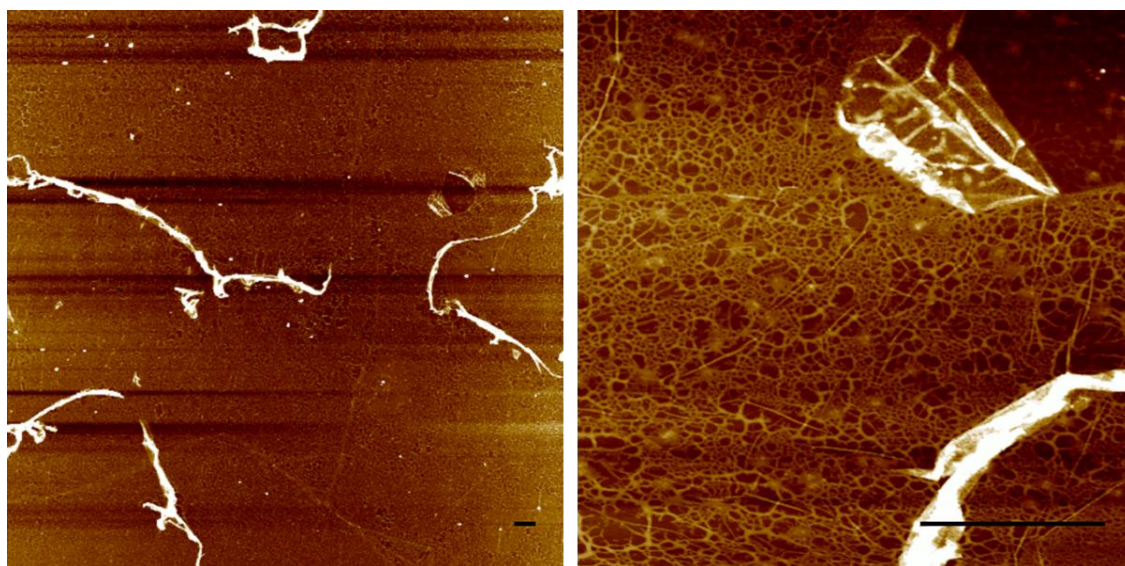
Figure 4.28: AFM height images of a large area (right) of graphene deposited on mica after interaction with cross-shaped DNA origami. A tear is present in the right-hand corner sheet exposing the mica surface where well-formed origami can be seen. (left) Zoom in of the tear seen in the image on the right. Scale bars, 1 µm (AFM lateral), 20 nm (height scale) for both AFM images.

Mica supported graphene dramatically altered the morphology of the adsorbed DNA origami. Only the rough texture of the graphene as compared to the mica surface, visible in the AFM images, serves as evidence of the presence of dis-associated origami based DNA. Furthermore, pristine origami which are visible on the mica revealed by tears in the graphene film are closely juxtaposed with a fibrous network on nearby graphene Fig. 4.29. Phase imaging, which yields qualitative surface composition discrimination between different materials, provides further evidence that the material coating the graphene is DNA. The contrast in the phase image Fig. 4.29b is the same for the origami on mica (dark brown) as for the majority of the graphene. Similar contrast is apparent in the phase image of Fig. 4.30. It may also be noted that material in the holes in the thin DNA film on graphene Fig. 4.29 has mechanical properties similar to mica (dark yellow). The complete loss of morphology of the DNA origami is only distinguishable by contrast with the same material on mica.
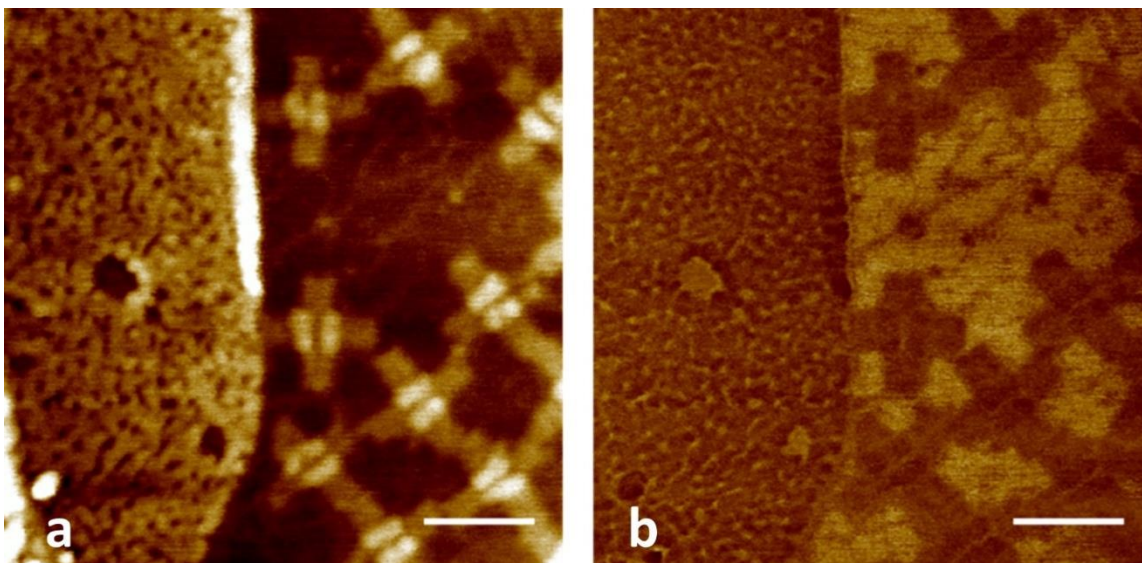
Figure 4.29: AFM height (a) and phase (b) image of DNA origami deposited on graphene-mica substrate. Scale bars, 100 nm (AFM lateral); 6 nm (height scale); 30 mV (phase).
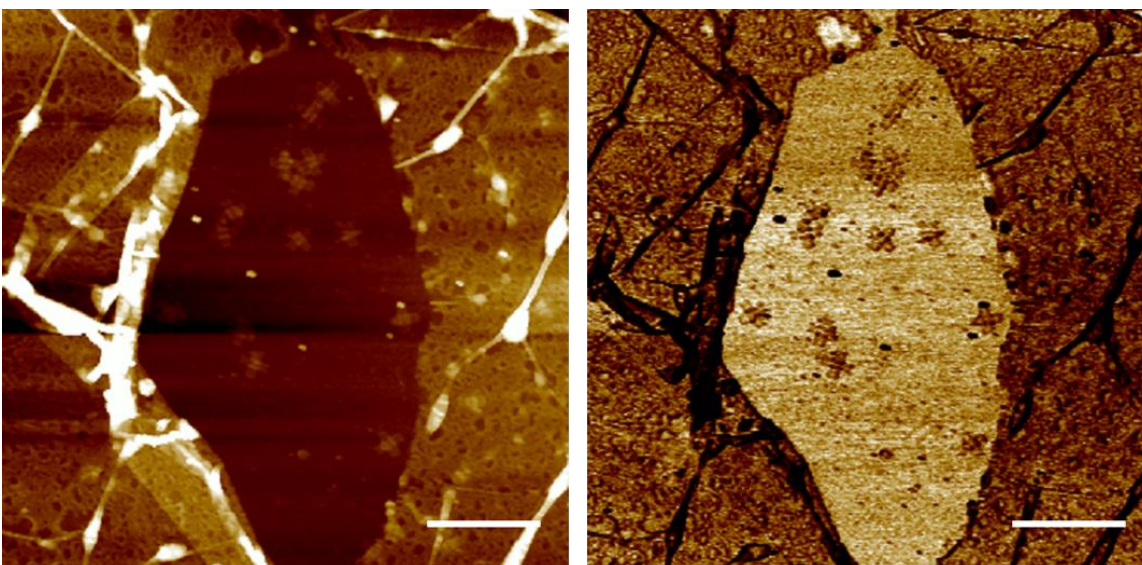
Figure 4.30: AFM height (left) and phase (right) images of a tear in a graphene sheet exposing the mica surface. Cross-shaped origami are present unperturbed on the mica only. Scale bars, 400 nm (AFM lateral), 15 nm (height scale); 30 mV (phase).

AFM height analysis has previously been used to probe DNA structure on mica for lattice arrangement, supercoiling, and to distinguish ssDNA from dsDNA[140-142]. Sample preparation and microscope conditions are critical for establishing reproducible and reliable AFM comparisons between experiments[143]. The present

approach, scanning over two different surfaces simultaneously under identical temperatures, tip conditions, humidity, etc, overcomes many of these limitations. Here, the height of DNA "origami" can be measured when adsorbed on graphene with respect to the height measured when the intact structures are presented on mica. The relative difference in height, measured by the difference in local minima and maxima of DNA on graphene or mica respectively, is shown in Fig. 4.31.
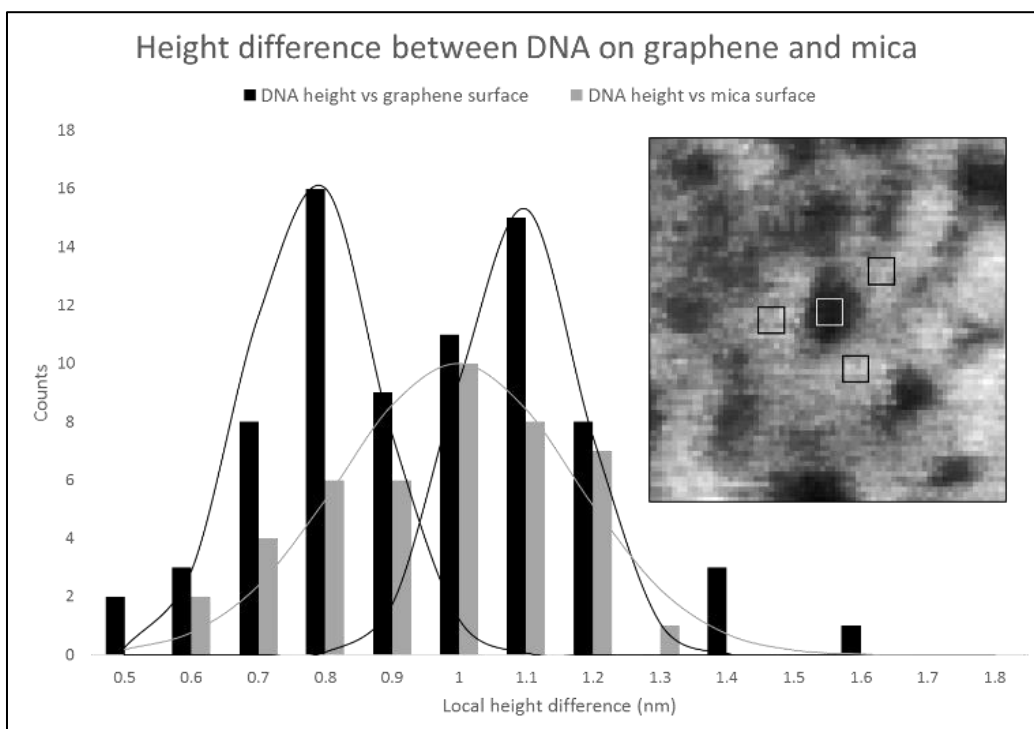
Figure 4.31: Histogram of height differences, between local minima and maxima, of cross-shaped DNA origami adsorbed onto graphene compared to a single duplex sheet of cross-shaped DNA origami adsorbed onto mica. Inset, representation of the method employed for determining relative height of DNA on graphene by calculating the difference between the average pixel intensities of a local minimum (a hole, white box) and the average of three local maxima (DNA surface coating, black boxes).

The histogram in Fig. 4.31 shows that DNA origami adsorbs under two normally distributed modes on graphene but only one mode for a single layer of cross-shaped DNA origami on mica. Two separate height modes suggest that DNA origami partially melts into ssDNA upon adsorption on graphene. The difference in

height average between melted origami on graphene, the lower mode, and duplex DNA on mica (0.2 nm) is in agreement with reported differences for ssDNA vs dsDNA on mica (0.3 nm)[142] It is important to note that only the single duplex region of the cross-shaped DNA origami, "the arms", were measured on mica in order to probe the relative height of one sheet of duplex DNA. The parallel raised rods at the center of the cross-shape are the result of two DNA duplexes stacked vertically on top of one another.

Chapter 5 - Conclusion and Future Work

We synthesized high quality CVD graphene by increasing the domain size to use in a variety of devices. In addition to increasing the domain-size of polycrystalline monolayer graphene films, we optimized CVD growth conditions to develop a fast growth of individual graphene domains using a two-step growth protocol which allows the nucleation density to remain low while promoting edge-growth.

Following CVD synthesis, we optimized graphene devices by implementing a variety of techniques during graphene transfer. In order to decrease substrate doping, and to increase the device mobility and on/off ratio, wafers were modified with SAMs. Because of the hydrophobic surface following SAM functionalization, the SAM modified wafers proved to be useful in removing bubbles from the graphene surface during transfer in solution. Bubble removal was demonstrated to further increase the device on/off ratio and mobility, especially over large-areas. In order to produce low sheet resistance devices, chemical doping was employed during transfer and enabled the fabrication of large-area graphene devices with sheet resistance less than the impedance of free-space.

Improved graphene devices (high mobility, low sheet resistance) were used for graphene-THz applications. Using transmission line theory, we show that at half-wave resonance, the sheet resistance dependent transmittance for a graphene-silicon-etalon matches that of a suspended sheet with a critical threshold of 377 ohms/sq where the absorptance dominates. Using the high-quality CVD graphene with a variety of transfer techniques, we demonstrate a graphene-THz device that is

impedance matched to the absorption dominating regime, and the largest depth of modulation for single-layer across broadband frequencies.

Graphene was used as a platform to investigate the detection of DNA. We simultaneously measured the change of conductance of a graphene film and the change in transmittance at 101 GHz when DNA was added. The signal-to-noise for changes induced by the DNA on THz transmittance was greater than that of the conductance change. DNA origami was also deposited on the graphene surface and was investigated by AFM. The interaction of the DNA origami with the graphene surface was strong enough that the DNA origami completely dissociated and could not be distinguished as the designed "tile" shape, which was confirmed on a bare mica surface.

The experiments started during this dissertation lays the foundation to developing new graphene-THz devices. A single-crystal graphene-THz device has yet to be demonstrated, and using the combined techniques, could realize a high mobility device capable of voltage switching from the transmission to absorption regime, toward the reflection regime. Furthermore, transfer using HBN films could further increase the graphene device mobility, especially by employing the large-area bubble removal method to produce flat HBN transfers. The transfer technique could be used to provide an insulating layer on top, and be used for top gating, increasing the modulation frequency.

In addition to simple top gating, gating using interdigitated electrodes or ring resonators could provide strong gating, and open the possibility of phase modulation. Furthermore, graphene devices could be patterned into arrays to study

THz beam shifting. Similar studies could be performed on patterned graphene films such as grids, and these devices could be placed on flexible polymers such as PDMS for mechanically actuated THz lenses.

Large-area graphene films with high mobility also could be used for new biosensing applications. These films could be patterned specifically toward plasmonics devices which would be useful for DNA detection, or graphene encapsulated by HBN could be used for scanning microwave microscopy with the capacitive sensing of species such as mitochondria.

The large-area devices developed in this dissertation merely demonstrates that large-area applications with high quality, single crystal graphene are possible, but surely, these concepts could be applied to fabricating improved nano/microscale devices and arrays.   By spanning nanometer to centimeter device scales, a plethora of new and powerful microwave to optical frequency devices could be realized.

References

(1)   Novoselov, K. S.; Geim, A. K.; Morozov, S. V; Jiang, D.; Zhang, Y.; Dubonos, S. V; Grigorieva, I. V; Firsov, A. A. Electric Field Effect in Atomically Thin Carbon Films. *Science* **2004**, *306* (5696), 666–669.

(2)   Nair, R. R.; Blake, P.; Grigorenko, A. N.; Novoselov, K. S.; Booth, T. J.; Stauber, T.; Peres, N. M. R.; Geim, A. K. Fine Structure Constant Defines Visual Transparency of Graphene. *Science* **2008**, *320* (5881), 1308.

(3)   Lee, C.; Wei, X.; Kysar, J. W.; Hone, J. Measurement of the Elastic Properties and Intrinsic Strength of Monolayer Graphene. *Science* **2008**, *321* (5887), 385–388.

(4)   Li, X.; Cai, W.; An, J.; Kim, S.; Nah, J.; Yang, D.; Piner, R.; Velamakanni, A.; Jung, I.; Tutuc, E.; Banerjee, S. K.; Colombo, L.; Ruoff, R. S. Large-Area Synthesis of High-Quality and Uniform Graphene Films on Copper Foils. *Science* **2009**, *324* (5932), 1312–1314.

(5)   Bae, S.; Kim, H.; Lee, Y.; Xu, X.; Park, J. S.; Zheng, Y.; Balakrishnan, J.; Lei, T.; Kim, H. R.; Song, Y. I. Roll-to-Roll Production of 30-Inch Graphene Films for Transparent Electrodes. *Nat. Nanotechnol.* **2010**.

(6)   Hao, Y.; Bharathi, M. S.; Wang, L.; Liu, Y.; Chen, H.; Nie, S.; Wang, X.; Chou, H.; Tan, C.; Fallahazad, B.; Ramanarayan, H.; Magnuson, C. W.; Tutuc, E.; Yakobson, B. I.; McCarty, K. F.; Zhang, Y. W.; Kim, P.; Hone, J.; Colombo, L.; Ruoff, R. S. The Role of Surface Oxygen in the Growth of Large Single-Crystal Graphene on Copper. *Science* **2013**, *342* (6159), 720–723.

(7)   Suk, J. W.; Kitt, A.; Magnuson, C. W.; Hao, Y.; Ahmed, S.; An, J.; Swan, A. K.; Goldberg, B. B.; Ruoff, R. S. Transfer of CVD-Grown Monolayer Graphene onto Arbitrary Substrates. *ACS Nano* **2011**, *5* (9), 6916–6924.

(8)   Goerbig, M. O. Electronic Properties of Graphene in a Strong Magnetic Field. *Rev. Mod. Phys.* **2011**, *83* (4), 1–56.

(9)   Neto, A. H. C.; Guinea, F.; Peres, N. M. R.; Novoselov, K. S.; Geim, A. K. The Electronic Properties of Graphene. *Rev. Mod. Phys.* **2007**, *81* (March).

(10) Novoselov, K. S.; Jiang, Z.; Zhang, Y.; Morozov, S. V.; Stormer, H. L.; Zeitler, U.; Maan, J. C.; Boebinger, G. S.; Kim, P.; Geim, A. K. Room-Temperature Quantum Hall Effect in Graphene. *Science* **2007**, *315* (5817), 1379.

(11) Otsuji, T. Frontiers of Graphene and Carbon Nanotubes. **2015**, 105–122.

(12) Falkovsky, L. a.; Varlamov, a. a. Space-Time Dispersion of Graphene Conductivity. *Eur. Phys. J. B* **2007**, *56* (4), 281–284.

(13) Falkovsky, L. A. Optical Properties of Graphene and IV–VI Semiconductors. *Physics-Uspekhi* **2008**, *51*, 887.

(14) Nair, R. R.; Blake, P.; Grigorenko, A. N.; Novoselov, K. S.; Booth, T. J.; Stauber, T.; Peres, N. M. R.; Geim, A. K. Fine Structure Constant Defines Visual Transparency of Graphene. *Science* **2008**, *320* (5881), 1308.

(15) Gusynin, V. P.; Sharapov, S. G.; Carbotte, J. P. On the Universal Ac Optical Background in Graphene. *New J. Phys.* **2009**, *11* (9), 95013.

(16) Yan, H.; Xia, F.; Zhu, W.; Freitag, M.; Dimitrakopoulos, C.; Bol, A. A.; Tulevski, G.; Avouris, P. Infrared Spectroscopy of Wafer-Scale Graphene. *ACS Nano* **2011**, *5* (12), 9854–9860.

(17) Horng, J.; Chen, C.-F.; Geng, B.; Girit, C.; Zhang, Y.; Hao, Z.; Bechtel, H. a.; Martin, M.; Zettl, A.; Crommie, M. F.; Shen, Y. R.; Wang, F. Drude Conductivity of Dirac Fermions in Graphene. *Phys. Rev. B* **2011**, *83* (16), 165113.

(18)   Rouhi, N.; Capdevila, S.; Jain, D.; Zand, K.; Wang, Y. Y.; Brown, E. R.; Jofre, L.; Burke, P. J. Terahertz Graphene Optics. *Nano Res.* **2012**, *5* (10), 667–678.

(19)   Zhang, W.; Pham, P. H. Q.; Brown, E. R.; Burke, P. J. AC Conductivity Parameters of Graphene Derived from THz Etalon Transmittance. *Nanoscale* **2014**, *6* (22), 13895–13899.

(20)   van der Zande, A. M.; Barton, R. A.; Alden, J. S.; Ruiz-Vargas, C. S.; Whitney, W. S.; Pham, P. H. Q.; Park, J.; Parpia, J. M.; Craighead, H. G.; McEuen, P. L. Large-Scale Arrays of Single-Layer Graphene Resonators. *Nano Lett.* **2010**, *10* (12), 4869.

(21)   Gao, W.; Shu, J.; Reichel, K.; Nickel, D. V; He, X.; Shi, G.; Vajtai, R.; Ajayan, P. M.; Kono, J.; Mittleman, D. M.; Xu, Q. High-Contrast Terahertz Wave Modulation by Gated Graphene Enhanced by Extraordinary Transmission through Ring Apertures. *Nano Lett.* **2014**, *14* (3), 1242–1248.

(22)   Hao, Y.; Bharathi, M. S.; Wang, L.; Liu, Y.; Chen, H.; Nie, S.; Wang, X.; Chou, H.; Tan, C.; Fallahazad, B.; Ramanarayan, H.; Magnuson, C. W.; Tutuc, E.; Yakobson, B. I.; McCarty, K. F.; Zhang, Y. W.; Kim, P.; Hone, J.; Colombo, L.; Ruoff, R. S. The Role of Surface Oxygen in the Growth of Large Single-Crystal Graphene on Copper. *Science* **2013**, *342* (6159), 720–723.

(23)   Zhou, H.; Yu, W. J.; Liu, L.; Cheng, R.; Chen, Y.; Huang, X.; Liu, Y.; Wang, Y.; Huang, Y.; Duan, X. Chemical Vapour Deposition Growth of Large Single Crystals of Monolayer and Bilayer Graphene. *Nat. Commun.* **2013**, *4*.

(24)   Li, J.; Wang, X.-Y.; Liu, X.; Jin, Z.; Wang, D.; Wan, L. Facile Growth of Centimeter-Sized Single-Crystal Graphene on Copper Foil at Atmospheric Pressure. *J. Mater. Chem. C* **2015**, *3* (15), 3530–3535.

(25) Robertson, A. W.; Warner, J. H. Hexagonal Single Crystal Domains of Few-Layer Graphene on Copper Foils. *Nano Lett.* **2011**, *11* (3), 1182–1189.

(26) Li, X.; Magnuson, C. W.; Venugopal, A.; An, J.; Suk, J. W.; Han, B.; Borysiak, M.; Cai, W.; Velamakanni, A.; Zhu, Y.; Fu, L.; Vogel, E. M.; Voelkl, E.; Colombo, L.; Ruoff, R. S. Graphene Films with Large Domain Size by a Two-Step Chemical Vapor Deposition Process. *Nano Lett.* **2010**, *10* (11), 4328–4334.

(27) Lee, Y.; Bae, S.; Jang, H.; Jang, S.; Zhu, S.-E.; Sim, S. H.; Song, Y. Il; Hong, B. H.; Ahn, J.-H. Wafer-Scale Synthesis and Transfer of Graphene Films. *Nano Lett.* **2010**, *10* (2), 490–493.

(28) Paul, R. K.; Badhulika, S.; Niyogi, S.; Haddon, R. C.; Boddu, V. M.; Costales-Nieves, C.; Bozhilov, K. N.; Mulchandani, A. The Production of Oxygenated Polycrystalline Graphene by One-Step Ethanol-Chemical Vapor Deposition. *Carbon* **2011**.

(29) Li, X.; Zhu, Y.; Cai, W.; Borysiak, M.; Han, B.; Chen, D.; Piner, R. D.; Colombo, L.; Ruoff, R. S. Transfer of Large-Area Graphene Films for High-Performance Transparent Conductive Electrodes. *Nano Lett.* **2009**, *9* (12), 4359–4363.

(30) Martins, L. G. P.; Song, Y.; Zeng, T.; Dresselhaus, M. S.; Kong, J.; Araujo, P. T. Direct Transfer of Graphene onto Fl Exible Substrates. **2013**.

(31) Kim, S. J.; Choi, T.; Lee, B.; Lee, S.; Choi, K.; Park, J. B.; Yoo, J. M.; Choi, Y. S.; Ryu, J.; Kim, P.; Hone, J.; Hong, B. H. Ultra-Clean Patterned Transfer of Single-Layer Graphene by Recyclable Pressure Sensitive Adhesive Films. *Nano Lett.* **2015**, 150406130050009.

(32) Caldwell, J. D.; Anderson, T. J.; Culbertson, J. C.; Jernigan, G. G.; Hobart, K. D.; Kub, F. J.; Tadjer, M. J.; Tedesco, J. L.; Hite, J. K.; Mastro, M. a.; Myers-Ward, R. L.; Eddy, C. R.; Campbell, P. M.; Gaskill, D. K. Technique for the Dry Transfer of Epitaxial Graphene

onto Arbitrary Substrates. *ACS Nano* **2010**, *4* (2), 1108–1114.

(33) Wang, Y. Y.; Burke, P. J. A Large-Area and Contamination-Free Graphene Transistor for Liquid-Gated Sensing Applications. *Appl. Phys. Lett.* **2013**, *103* (5), 52103.

(34) Han, Y.; Zhang, L.; Zhang, X.; Ruan, K.; Cui, L.; Wang, Y.; Liao, L.; Wang, Z.; Jie, J. Clean Surface Transfer of Graphene Films via an Effective Sandwich Method for Organic Light-Emitting Diode Applications. *J. Mater. Chem. C* **2014**, *2* (1), 201–207.

(35) Su, C.-Y.; Fu, D.; Lu, A.-Y.; Liu, K.-K.; Xu, Y.; Juang, Z.-Y.; Li, L.-J. Transfer Printing of Graphene Strip from the Graphene Grown on Copper Wires. *Nanotechnology* **2011**, *22* (18), 185309.

(36) Lin, Y. C.; Jin, C.; Lee, J. C.; Jen, S. F.; Suenaga, K.; Chiu, P. W. Clean Transfer of Graphene for Isolation and Suspension. *ACS Nano* **2011**, *5* (3), 2362–2368.

(37) Lin, Y.-C.; Lu, C.-C.; Yeh, C.-H.; Jin, C.; Suenaga, K.; Chiu, P.-W. Graphene Annealing: How Clean Can It Be? *Nano Lett.* **2012**, *12* (1), 414–419.

(38) Regan, W.; Alem, N.; Alemán, B.; Geng, B.; Girit, C.; Maserati, L.; Wang, F.; Crommie, M.; Zettl, a. A Direct Transfer of Layer-Area Graphene. *Appl. Phys. Lett.* **2010**, *96* (11), 113102.

(39) Gao, L.; Ni, G.-X.; Liu, Y.; Liu, B.; Castro Neto, A. H.; Loh, K. P. Face-to-Face Transfer of Wafer-Scale Graphene Films. *Nature* **2014**, *505* (7482), 190–194.

(40) Banszerus, L.; Schmitz, M.; Engels, S.; Dauber, J.; Oellers, M.; Haupt, F.; Watanabe, K.; Taniguchi, T.; Beschoten, B.; Stampfer, C. Ultrahigh-Mobility Graphene Devices from Chemical Vapor Deposition on Reusable Copper. *Sci. Adv.* **2015**, *1* (6), 1–6.

(41) Cherian, C. T.; Giustiniano, F.; Martin-Fernandez, I.; Andersen, H.; Balakrishnan, J.; Özyilmaz, B. "Bubble-Free" Electrochemical Delamination of CVD Graphene Films.

Small **2015**, *11* (2), 189–194.

(42) Brown, E. R.; Zhang, W. D.; Neff, D.; Green, N. S.; Norton, M. L.; Pham, P. H. Q.; Burke, P. J. Detection of DNA by Graphene-on-Silicon FET Structures Simultaneously at DC and 101 GHz. In *European Microwave Week 2015: "Freedom Through Microwaves", EuMW 2015 - Conference Proceedings; 2015 45th European Microwave Conference Proceedings, EuMC*; 2015; pp 929–932.

(43) Ferrari, A. C.; Meyer, J. C.; Scardaci, V.; Casiraghi, C.; Lazzeri, M.; Mauri, F.; Piscanec, S.; Jiang, D.; Novoselov, K. S.; Roth, S.; Geim, A. K. Raman Spectrum of Graphene and Graphene Layers. *Phys. Rev. Lett.* **2006**, *97* (18), 187401.

(44) Chan, J.; Venugopal, A.; Pirkle, A.; McDonnell, S.; Hinojos, D.; Magnuson, C. W.; Ruoff, R. S.; Colombo, L.; Wallace, R. M.; Vogel, E. Reducing Extrinsic Performance Limiting Factors in Graphene Grown by Chemical Vapor Deposition. *ACS Nano* **2012**.

(45) Chen, S.; Ji, H.; Chou, H.; Li, Q.; Li, H.; Suk, J. W.; Piner, R.; Liao, L.; Cai, W.; Ruoff, R. S. Millimeter-Size Single-Crystal Graphene by Suppressing Evaporative Loss of Cu during Low Pressure Chemical Vapor Deposition. *Adv. Mater.* **2013**, *25* (14), 2062–2065.

(46) Gan, L.; Luo, Z. Turning off Hydrogen to Realize Seeded Growth of Subcentimeter Single-Crystal Graphene Grains on Copper. *ACS Nano* **2013**, *7* (10), 9480–9488.

(47) Li, X.; Magnuson, C. W.; Venugopal, A.; Tromp, R. M.; Hannon, J. B.; Vogel, E. M.; Colombo, L.; Ruoff, R. S. Large-Area Graphene Single Crystals Grown by Low-Pressure Chemical Vapor Deposition of Methane on Copper. *J. Am. Chem. Soc.* **2011**, *133* (9), 2816–2819.

(48) Yu, Q.; Jauregui, L. A.; Wu, W.; Colby, R.; Tian, J.; Su, Z.; Cao, H.; Liu, Z.; Pandey, D.; Wei,

D.; Chung, T. F.; Peng, P.; Guisinger, N. P.; Stach, E. A.; Bao, J.; Pei, S. S.; Chen, Y. P. Control and Characterization of Individual Grains and Grain Boundaries in Graphene Grown by Chemical Vapour Deposition. *Nat. Mater.* **2011**, *10* (6), 443–449.

(49) Huang, P. Y.; Ruiz-Vargas, C. S.; van der Zande, A. M.; Whitney, W. S.; Levendorf, M. P.; Kevek, J. W.; Garg, S.; Alden, J. S.; Hustedt, C. J.; Zhu, Y.; Park, J.; McEuen, P. L.; Muller, D. A. Grains and Grain Boundaries in Single-Layer Graphene Atomic Patchwork Quilts. *Nature* **2011**, *469* (7330), 389–392.

(50) Yan, Z.; Lin, J.; Peng, Z.; Sun, Z.; Zhu, Y.; Li, L.; Xiang, C.; Samuel, E. L.; Kittrell, C.; Tour, J. M. Toward the Synthesis of Wafer-Scale Single-Crystal Graphene on Copper Foils. *ACS Nano* **2012**, *6* (10), 9110–9117.

(51) Chen, X.; Zhao, P.; Xiang, R.; Kim, S.; Cha, J.; Chiashi, S.; Maruyama, S. Chemical Vapor Deposition Growth of 5 Mm Hexagonal Single-Crystal Graphene from Ethanol. *Carbon* **2015**, *94*, 810–815.

(52) Kim, H.; Mattevi, C.; Calvo, M. R.; Oberg, J. C.; Artiglia, L.; Agnoli, S.; Hirjibehedin, C. F.; Chhowalla, M.; Saiz, E. Activation Energy Paths for Graphene Nucleation and Growth on Cu. *ACS Nano* **2012**, *6* (4), 3614–3623.

(53) Hao, Y.; Wang, L.; Liu, Y.; Chen, H.; Wang, X.; Tan, C.; Nie, S.; Suk, J. W.; Jiang, T.; Liang, T.; Xiao, J.; Ye, W.; Dean, C. R.; Yakobson, B. I.; Mccarty, K. F.; Kim, P.; Hone, J.; Colombo, L.; Ruoff, R. S. Oxygen-Activated Growth and Bandgap Tunability of Large Single-Crystal Bilayer Graphene. *Nat. Nanotechnol.* **2016**, *11*, 426–231.

(54) Li, X.; Cai, W.; Colombo, L.; Ruoff, R. S. Evolution of Graphene Growth on Ni and Cu by Carbon Isotope Labeling. *Nano Lett.* **2009**, *9* (12), 4268–4272.

(55) Wang, H.; Wang, G.; Bao, P.; Yang, S.; Zhu, W.; Xie, X.; Zhang, W. J. Controllable

Synthesis of Submillimeter Single-Crystal Monolayer Graphene Domains on Copper Foils by Suppressing Nucleation. *J. Am. Chem. Soc.* **2012**, *134* (8), 3627–3630.

(56)   Reina, A.; Son, H.; Jiao, L.; Fan, B.; Dresselhaus, M. S.; Liu, Z.; Kong, J. Transferring and Identification of Single- and Few-Layer Graphene on Arbitrary Substrates Transferring and Identification of Single- and Few-Layer Graphene on Arbitrary Substrates. *J. Phys. Chem. C* **2008**, *112*, 17741–17744.

(57)   Meyer, J. C.; Geim, A. K.; Katsnelson, M. I.; Novoselov, K. S.; Booth, T. J.; Roth, S. The Structure of Suspended Graphene Sheets. *Nature* **2007**, *446* (7131), 60–63.

(58)   Lee, W. H.; Park, J.; Kim, Y.; Kim, K. S.; Hong, B. H.; Cho, K. Control of Graphene Field-Effect Transistors by Interfacial Hydrophobic Self-Assembled Monolayers. *Adv. Mater.* **2011**, *23* (30), 3460–3464.

(59)   Pirkle, A.; Chan, J.; Venugopal, A.; Hinojos, D.; Magnuson, C. W.; McDonnell, S.; Colombo, L.; Vogel, E. M.; Ruoff, R. S.; Wallace, R. M. The Effect of Chemical Residues on the Physical and Electrical Properties of Chemical Vapor Deposited Graphene Transferred to SiO2. *Appl. Phys. Lett.* **2011**, *99* (12), 2–5.

(60)   Cancado, L. G.; Jorio, A.; Ferreira, E. H. M.; Stavale, F.; Achete, C. A.; Capaz, R. B.; Moutinho, M. V. O.; Lombardo, A.; Kulmala, T. S.; Ferrari, A. C. Quantifying Defects in Graphene via Raman Spectroscopy at Different Excitation Energies. *Nano Lett.* **2011**, *11* (8), 3190–3196.

(61)   Das, A.; Pisana, S.; Chakraborty, B.; Piscanec, S.; Saha, S. K.; Waghmare, U. V.; Novoselov, K. S.; Krishnamurthy, H. R.; Geim, A. K.; Ferrari, A. C.; Sood, A. K. Monitoring Dopants by Raman Scattering in an Electrochemically Top-Gated Graphene Transistor. *Nat. Nanotechnol.* **2008**, *3* (4), 210–215.

(62) Duong, D. L.; Han, G. H.; Lee, S. M.; Gunes, F.; Kim, E. S.; Kim, S. T.; Kim, H.; Ta, Q. H.; So, K. P.; Yoon, S. J.; Chae, S. H. S. J.; Jo, Y. W.; Park, M. H.; Chae, S. H. S. J.; Lim, S. C.; Choi, J. Y.; Lee, Y. H. Probing Graphene Grain Boundaries with Optical Microscopy. *Nature* **2012**, *490* (7419), 235–239.

(63) Li, Q.; Chou, H.; Zhong, J. H.; Liu, J. Y.; Dolocan, A.; Zhang, J.; Zhou, Y.; Ruoff, R. S.; Chen, S.; Cai, W. Growth of Adlayer Graphene on Cu Studied by Carbon Isotope Labeling. *Nano Lett.* **2013**, *13* (2), 486–490.

(64) Zhang, W.; Wu, P.; Li, Z.; Yang, J. First-Principles Thermodynamics of Graphene Growth on Cu Surfaces. *J. Phys. Chem. C* **2011**, *115* (36), 17782–17787.

(65) Bhaviripudi, S.; Jia, X.; Dresselhaus, M. S.; Kong, J. Role of Kinetic Factors in Chemical Vapor Deposition Synthesis of Uniform Large Area Graphene Using Copper Catalyst. *Nano Lett.* **2010**, *10* (10), 4128–4133.

(66) Loginova, E.; Bartelt, N. C.; Feibelman, P. J.; McCarty, K. F. Evidence for Graphene Growth by C Cluster Attachment. *New J. Phys.* **2008**, *10*.

(67) Zhao, Z.; Shan, Z.; Zhang, C.; Li, Q.; Tian, B.; Huang, Z.; Lin, W.; Chen, X.; Ji, H.; Zhang, W.; Cai, W. Study on the Diffusion Mechanism of Graphene Grown on Copper Pockets. *Small* **2015**, *11* (12), 1418–1422.

(68) Losurdo, M.; Giangregorio, M. M.; Capezzuto, P.; Bruno, G. Graphene CVD Growth on Copper and Nickel: Role of Hydrogen in Kinetics and Structure. *Phys. Chem. Chem. Phys.* **2011**, *13* (46), 20836.

(69) Zhang, X.; Wang, L.; Xin, J. H.; Yakobson, B. I.; Ding, F. Role of Hydrogen in Graphene Chemical Vapor Deposition Growth on a Copper Surface. *J. Am. Chem. Soc.* **2014**, *136* (8), 3040–3047.

(70)   Riikonen, S.; Krasheninnikov, A. V.; Halonen, L.; Nieminen, R. M. The Role of Stable and Mobile Carbon Adspecies in Copper-Promoted Graphene Growth. *J. Phys. Chem. C* **2012**, *116* (9), 5802–5809.

(71)   Gao, J.; Yip, J.; Zhao, J.; Yakobson, B. I.; Ding, F. Graphene Nucleation on Transition Metal Surface: Structure Transformation and Role of the Metal Step Edge. *J. Am. Chem. Soc.* **2011**, *133* (13), 5009–5015.

(72)   Artyukhov, V. I.; Liu, Y.; Yakobson, B. I. Equilibrium at the Edge and Atomistic Mechanisms of Graphene Growth. *Proc. Natl. Acad. Sci.* **2012**, *109*, 15136–15140.

(73)   Yuan, Q.; Yakobson, B. I.; Ding, F. Edge-Catalyst Wetting and Orientation Control of Graphene Growth by Chemical Vapor Deposition Growth. *J. Phys. Chem. Lett.* **2014**, *5* (18), 3093–3099.

(74)   Artyukhov, V. I.; Hao, Y.; Ruoff, R. S.; Yakobson, B. I. Breaking of Symmetry in Graphene Growth on Metal Substrates. *Phys. Rev. Lett.* **2015**, *114* (11), 1–6.

(75)   Gao, L.; Ren, W.; Xu, H.; Jin, L.; Wang, Z.; Ma, T.; Ma, L.-P.; Zhang, Z.; Fu, Q.; Peng, L.-M.; Bao, X.; Cheng, H.-M. Repeated Growth and Bubbling Transfer of Graphene with Millimetre-Size Single-Crystal Grains Using Platinum. *Nat. Commun.* **2012**, *3*, 699.

(76)   Loginova, E.; Bartelt, N. C.; Feibelmarr, P. J.; McCarty, K. F. Factors Influencing Graphene Growth on Metal Surfaces. *New J. Phys.* **2009**, *11*.

(77)   Kwon, S. Y.; Ciobanu, C. V.; Petrova, V.; Shenoy, V. B.; Bareño, J.; Gambin, V.; Petrov, I.; Kodambaka, S. Growth of Semiconducting Graphene on Palladium. *Nano Lett.* **2009**, *9* (12), 3985–3990.

(78)   Kim, K. S. K. S.; Zhao, Y.; Jang, H.; Lee, S. Y.; Kim, J. M.; Ahn, J.; Kim, P.; Choi, J.-Y.; Hong, B. H. Large-Scale Pattern Growth of Graphene Films for Stretchable Transparent

Electrodes. *Nature* **2009**, *457* (7230), 706–710.

(79) Iwasaki, T.; Park, H. J.; Konuma, M.; Lee, D. S.; Smet, J. H.; Starke, U. Long-Range Ordered Single-Crystal Graphene on High-Quality Heteroepitaxial Ni Thin Films Grown on MgO(111). *Nano Lett.* **2011**, *11* (1), 79–84.

(80) Pan, Y.; Zhang, H.; Shi, D.; Sun, J.; Du, S.; Liu, F.; Gao, H. J. Highly Ordered, Millimeter-Scale, Continuous, Single-Crystalline Graphene Monolayer Formed on Ru (0001). *Adv. Mater.* **2009**, *21* (27), 2777–2780.

(81) Liang, X.; Sperling, B. A.; Calizo, I.; Cheng, G.; Hacker, C. A.; Zhang, Q.; Obeng, Y.; Yan, K.; Peng, H.; Li, Q.; Zhu, X.; Yuan, H.; Walker, A. R. H.; Liu, Z.; Peng, L.; Richter, C. A. Toward Clean and Crackless Transfer of Graphene. **2011**, No. 11, 9144–9153.

(82) Yan, Z.; Sun, Z.; Lu, W.; Yao, J.; Zhu, Y.; Tour, J. M. Controlled Modulation of Electronic Properties of Graphene by Self-Assembled Monolayers on SiO2 Substrates. *ACS Nano* **2011**, *5* (2), 1535–1540.

(83) Wang, Q. H.; Jin, Z.; Kim, K. K.; Hilmer, A. J.; Paulus, G. L. C.; Shih, C.-J.; Ham, M.-H.; Sanchez-Yamagishi, J. D.; Watanabe, K.; Taniguchi, T.; Kong, J.; Jarillo-Herrero, P.; Strano, M. S. Understanding and Controlling the Substrate Effect on Graphene Electron-Transfer Chemistry via Reactivity Imprint Lithography. *Nat. Chem.* **2012**, *4* (9), 724–732.

(84) Kim, S. J.; Ryu, J.; Son, S.; Yoo, J. M.; Park, J. B.; Won, D.; Lee, E. K.; Cho, S. P.; Bae, S.; Cho, S.; Hong, B. H. Simultaneous Etching and Doping by Cu-Stabilizing Agent for High-Performance Graphene-Based Transparent Electrodes. *Chem. Mater.* **2014**, *26* (7), 2332–2336.

(85) Mattevi, C.; Kim, H.; Chhowalla, M. A Review of Chemical Vapour Deposition of

Graphene on Copper. *J. Mater. Chem.* **2011**, *21* (10), 3324.

(86) Liang, T.; Luan, C.; Chen, H.; Xu, M. Exploring Oxygen in Graphene Chemical Vapor Deposition Synthesis. *Nanoscale* **2017**, *9* (11), 3719–3735.

(87) Liu, K. K.; Zhang, W.; Lee, Y. H.; Lin, Y. C.; Chang, M. T.; Su, C. Y.; Chang, C. S.; Li, H.; Shi, Y.; Zhang, H.; Lai, C. S.; Li, L. J. Growth of Large-Area and Highly Crystalline MoS2thin Layers on Insulating Substrates. *Nano Lett.* **2012**, *12* (3), 1538–1544.

(88) Zhan, Y.; Liu, Z.; Najmaei, S.; Ajayan, P. M.; Lou, J. Large-Area Vapor-Phase Growth and Characterization of MoS2 Atomic Layers on a SiO 2 Substrate. *Small* **2012**, *8* (7), 966–971.

(89) Song, L.; Ci, L.; Lu, H.; Sorokin, P. B.; Jin, C.; Ni, J.; Kvashnin, A. G.; Kvashnin, D. G.; Lou, J.; Yakobson, B. I.; Ajayan, P. M. Large Scale Growth and Characterization of Atomic Hexagonal Boron Nitride Layers. *Nano Lett.* **2010**, *10* (8), 3209–3215.

(90) Chen, Y.; Gong, X. L.; Gai, J. G. Progress and Challenges in Transfer of Large-Area Graphene Films. *Adv. Sci.* **2016**, *3* (8), 1–15.

(91) Chen, M.; Haddon, R. C.; Yan, R.; Bekyarova, E. Advances in Transferring Chemical Vapour Deposition Graphene: A Review. *Mater. Horizons* **2017**, *4* (6), 1054–1063.

(92) Wang, Y.; Zheng, Y.; Xu, X.; Dubuisson, E.; Bao, Q.; Lu, J.; Loh, K. P.; Al, W. E. T. Electrochemical Delamination of CVD- Grown Graphene Film : Toward the Recyclable Use of Copper Catalyst. **2011**, No. 12, 9927–9933.

(93) Hallam, T.; Berner, N. C.; Yim, C.; Duesberg, G. S. Strain, Bubbles, Dirt, and Folds: A Study of Graphene Polymer-Assisted Transfer. *Adv. Mater. Interfaces* **2014**, *1* (6), 1–7.

(94) Pizzocchero, F.; Jessen, B. S.; Whelan, P. R.; Kostesha, N.; Lee, S.; Buron, J. D.;

Petrushina, I.; Larsen, M. B.; Greenwood, P.; Cha, W. J.; Teo, K.; Jepsen, P. U.; Hone, J.; Bøggild, P.; Booth, T. J. Non-Destructive Electrochemical Graphene Transfer from Reusable Thin-Film Catalysts. *Carbon* **2015**, *85*, 397–405.

(95)   Attard, P. Bridging Bubbles between Hydrophobic Surfaces. *Langmuir* **1996**, *12* (6), 1693–1695.

(96)   Rafiee, J.; Mi, X.; Gullapalli, H.; Thomas, A. V. A. V. A.; Yavari, F.; Shi, Y.; Ajayan, P. M.; Koratkar, N. A. Wetting Transparency of Graphene. *Nat. Mater.* **2012**, *11* (March), 217–222.

(97)   Kang, J.; Hwang, S.; Kim, J. H.; Kim, M. H.; Ryu, J.; Seo, S. J. Transfer of Large-Area Graphene Films onto Rigid Substrates by Hot Pressing. **2012**, No. 6, 5360–5365.

(98)   Kim, S. J.; Choi, T.; Lee, B.; Lee, S.; Choi, K.; Park, J. B.; Yoo, J. M.; Choi, Y. S.; Ryu, J.; Kim, P.; Hone, J.; Hong, B. H. Ultraclean Patterned Transfer of Single-Layer Graphene by Recyclable Pressure Sensitive Adhesive Films. *Nano Lett.* **2015**, *15* (5), 3236–3240.

(99)   Pham, P. H. Q.; Zhou, W.; Quach, N. V.; Li, J.; Zheng, J.-G.; Burke, P. J. Controlling Nucleation Density While Simultaneously Promoting Edge Growth Using Oxygen-Assisted Fast Synthesis of Isolated Large-Domain Graphene. *Chem. Mater.* **2016**, *28* (18), 6511–6519.

(100) Schwierz, F. Graphene Transistors. *Nat. Nanotechnol.* **2010**, *5* (7), 487–496.

(101) Sensale-Rodriguez, B.; Yan, R.; Kelly, M. M.; Fang, T.; Tahy, K.; Hwang, W. S.; Jena, D.; Liu, L.; Xing, H. G. Broadband Graphene Terahertz Modulators Enabled by Intraband Transitions. *Nat. Commun.* **2012**, *3*, 780.

(102) Buron, J. D.; Pizzocchero, F.; Jepsen, P. U.; Petersen, D. H.; Caridad, J. M.; Jessen, B. S.; Booth, T. J.; Bøggild, P. Graphene Mobility Mapping. *Sci. Rep.* **2015**, *5*, 12305.

(103) Pham, P. H. Q.; Zhang, W.; Quach, N. V.; Li, J.; Zhou, W.; Scarmardo, D.; Brown, E. R.; Burke, P. J. Broadband Impedance Match to Two-Dimensional Materials in the Terahertz Domain. *Nat. Commun.* **2017**, *8* (1), 2233.

(104) Brown, E. R.; Zhang, W. D.; Chen, H.; Mearini, G. T. THz Behavior of Indium-Tin-Oxide Films on P-Si Substrates. *Appl. Phys. Lett.* **2015**, *107* (9), 91102.

(105) Pozar, D. M. *Microwave Engineering*, 3rd ed.; J. Wiley: Hoboken, NJ, 2005.

(106) Woltersdorff, W. Uber Die Optischen Konstanten Dunner Metallschichten Im Langwelligen Ultrarot. *Zeitschrift fur Phys.* **1934**, *91* (3–4), 230–252.

(107) Zanotto, S.; Bianco, F.; Miseikis, V.; Convertino, D.; Coletti, C.; Tredicucci, A. Coherent Absorption of Light by Graphene and Other Optically Conducting Surfaces in Realistic on-Substrate Configurations. *APL Photonics* **2017**, *2* (1), 16101.

(108) Demers, J. R.; Ronald T. Logan, J.; Bergeron, N. J.; Brown, E. R. A Coherent Frequency-Domain THz Spectrometer with a Signal-to-Noise Ratio of 60 dB at 1 THz; SPIE, 2008; Vol. 6949, p 694909.

(109) Dressel, M.; Gruner, G. *Electrodynamics of Solids: Optical Properties of Electrons in Matter*; Cambridge university press, 2002.

(110) Sensale-Rodriguez, B.; Yan, R.; Rafique, S.; Zhu, M.; Li, W.; Liang, X.; Gundlach, D.; Protasenko, V.; Kelly, M. M.; Jena, D.; Liu, L.; Xing, H. G. Extraordinary Control of Terahertz Beam Reflectance in Graphene Electro-Absorption Modulators. *Nano Lett.* **2012**, *21* (2), 936–941.

(111) Ren, L.; Zhang, Q.; Yao, J.; Sun, Z.; Kaneko, R.; Yan, Z.; Nanot, S.; Jin, Z.; Kawayama, I.; Tonouchi, M.; Tour, J. M.; Kono, J. Terahertz and Infrared Spectroscopy of Gated Large-Area Graphene. *Nano Lett.* **2012**, *12* (7), 3711–3715.

(112) Cervetti, C.; Heintze, E.; Gorshunov, B.; Zhukova, E.; Lobanov, S.; Hoyer, A.; Burghard, M.; Kern, K.; Dressel, M.; Bogani, L. Sub-Terahertz Frequency-Domain Spectroscopy Reveals Single-Grain Mobility and Scatter Influence of Large-Area Graphene. *Adv. Mater.* **2015**, *27* (16), 2635–2641.

(113) Min Woo, J.; Kim, M.-S.; Woong Kim, H.; Jang, J.-H. Graphene Based Salisbury Screen for Terahertz Absorber. *Appl. Phys. Lett.* **2014**, *104* (8), 81106.

(114) Maeng, I.; Lim, S.; Chae, S. J.; Lee, Y. H.; Choi, H.; Son, J.-H. Gate-Controlled Nonlinear Conductivity of Dirac Fermion in Graphene Field-Effect Transistors Measured by Terahertz Time-Domain Spectroscopy. *Nano Lett.* **2012**, *12* (2), 551–555.

(115) Liang, G.; Hu, X.; Yu, X.; Shen, Y.; Li, L. H.; Davies, A. G.; Linfield, E. H.; Liang, H. K.; Zhang, Y.; Yu, S. F.; Wang, Q. J. Integrated Terahertz Graphene Modulator with 100% Modulation Depth. *ACS Photonics* **2015**, *2* (11), 1559–1566.

(116) Mics, Z.; Tielrooij, K.-J.; Parvez, K.; Jensen, S. a.; Ivanov, I.; Feng, X.; Müllen, K.; Bonn, M.; Turchinovich, D. Thermodynamic Picture of Ultrafast Charge Transport in Graphene. *Nat. Commun.* **2015**, *6* (May), 7655.

(117) Sten, J. C. E.; Koivisto, P. K. Optimum Transparent Absorbers of Electromagnetic Waves. *IEEE Trans. Electromagn. Compat.* **2008**, *50* (4), 1011–1014.

(118) Banszerus, L.; Schmitz, M.; Engels, S.; Dauber, J.; Oellers, M.; Haupt, F.; Watanabe, K.; Taniguchi, T.; Beschoten, B.; Stampfer, C. Ultrahigh-Mobility Graphene Devices from Chemical Vapor Deposition on Reusable Copper. *Sci. Adv.* **2015**, *1* (6), e1500222.

(119) Fang, Z.; Wang, Y.; Schlather, A. E.; Liu, Z.; Ajayan, P. M.; Garcia De Abajo, F. J.; Nordlander, P.; Zhu, X.; Halas, N. J. Active Tunable Absorption Enhancement with Graphene Nanodisk Arrays. *Nano Lett.* **2014**, *14* (1), 299–304.

(120) Batrakov, K.; Kuzhir, P.; Maksimenko, S.; Volynets, N.; Voronovich, S.; Paddubskaya, A.; Valusis, G.; Kaplas, T.; Svirko, Y.; Lambin, P. Enhanced Microwave-to-Terahertz Absorption in Graphene. *Appl. Phys. Lett.* **2016**, *108* (12), 123101.

(121) Balci, O.; Polat, E. O.; Kakenov, N.; Kocabas, C. Graphene-Enabled Electrically Switchable Radar-Absorbing Surfaces. *Nat. Commun.* **2015**, *6*, 6628.

(122) Wu, B.; Tuncer, H. M.; Naeem, M.; Yang, B.; Cole, M. T.; Milne, W. I.; Hao, Y. Experimental Demonstration of a Transparent Graphene Millimetre Wave Absorber with 28% Fractional Bandwidth at 140 GHz. *Sci. Rep.* **2014**, *4*, 4130.

(123) Grande, M.; Bianco, G. V.; Vincenti, M. A.; de Ceglia, D.; Capezzuto, P.; Scalora, M.; D'Orazio, A.; Bruno, G. Optically Transparent Microwave Polarizer Based On Quasi-Metallic Graphene. *Sci. Rep.* **2015**, *5*, 17083.

(124) Thongrattanasiri, S.; Koppens, F. H. L.; Garcia De Abajo, F. J. Complete Optical Absorption in Periodically Patterned Graphene. *Phys. Rev. Lett.* **2012**, *108* (4), 47401.

(125) Gorshunov, B. P.; Fedorov, I. V.; Kozlov, G. V.; Volkov, A. A.; Semenov, A. D. Dynamic Conductivity and the Coherence Peak in the Submillimeter Spectra of Superconducting NbN Films. *Solid State Commun.* **1993**, *87* (1), 17–21.

(126) Gorshunov, B. P.; Kozlov, G. V.; Volkov, A. A.; Lebedev, S. P.; Fedorov, I. V.; Prokhorov, A. M.; Makhov, V. I.; Schutzman, J.; Renk, K. F. Measurement of Electrodynamic Parameters of Superconducting Films in the Far-Infrared and Submillimeter Frequency Ranges. *Int. J. Infrared Millimeter Waves* **1993**, *14* (3), 683–702.

(127) Pronin, A. V.; Dressel, M.; Pimenov, A.; Loidl, A.; Roshchin, I. V.; Greene, L. H. Direct Observation of the Superconducting Energy Gap Developing in the Conductivity Spectra of Niobium. *Phys. Rev. B* **1998**, *57* (22), 14416–14421.

(128) Sensale-Rodriguez, B.; Yan, R.; Rafique, S.; Mingda Zhu; Kelly, M.; Protasenko, V.; Jena, D.; Liu, L.; Xing, H. G. Exceptional Tunability of THz Reflectance in Graphene Structures. *Int. Conf. Infrared, Millimeter, Terahertz Waves, IRMMW-THz* **2012**, 1–3.

(129) Sensale-Rodriguez, B.; Fang, T.; Yan, R.; Kelly, M. M.; Jena, D.; Liu, L.; Xing, H. Unique Prospects for Graphene-Based Terahertz Modulators. *Appl. Phys. Lett.* **2011**, *99* (11), 113104.

(130) Rakheja, S.; Kumar, V.; Naeemi, A. Evaluation of the Potential Performance of Graphene Nanoribbons as on-Chip Interconnects. *Proc. IEEE* **2013**, *101* (7), 1740–1765.

(131) Tan, Y. W.; Zhang, Y.; Bolotin, K.; Zhao, Y.; Adam, S.; Hwang, E. H.; Das Sarma, S.; Stormer, H. L.; Kim, P. Measurement of Scattering Rate and Minimum Conductivity in Graphene. *Phys. Rev. Lett.* **2007**, *99* (24), 246803.

(132) Verleur, H. W.; Barker, A. S.; Berglund, C. N. Optical Properties of VO2 between 0.25 and 5 eV. *Rev. Mod. Phys.* **1968**, *172* (3), 788.

(133) Liu, M.; Hwang, H. Y.; Tao, H.; Strikwerda, A. C.; Fan, K.; Keiser, G. R.; Sternbach, A. J.; West, K. G.; Kittiwatanakul, S.; Lu, J.; Wolf, S. a; Omenetto, F. G.; Zhang, X.; Nelson, K. a; Averitt, R. D. Terahertz-Field-Induced Insulator-to-Metal Transition in Vanadium Dioxide Metamaterial. *Nature* **2012**, *487* (7407), 345–348.

(134) Dean, C. R.; Young, a F.; Meric, I.; Lee, C.; Wang, L.; Sorgenfrei, S.; Watanabe, K.; Taniguchi, T.; Kim, P.; Shepard, K. L.; Hone, J. Boron Nitride Substrates for High-Quality Graphene Electronics. *Nat. Nanotechnol.* **2010**, *5* (10), 722–726.

(135) Wang, L.; Meric, I.; Huang, P. Y.; Gao, Q.; Gao, Y.; Tran, H.; Taniguchi, T.; Watanabe, K.; Campos, I. M.; Muller, D. A.; Guo, J.; Kim, P.; Hone, J.; Shepard, K. .; Dean, C. R. One-

Dimensional Electrical Contact to a Two-Dimensional Material. *Science* **2013**, No. November, 614–617.

(136) Rahm, M.; Li, J. S.; Padilla, W. J. THz Wave Modulators: A Brief Review on Different Modulation Techniques. *J. Infrared, Millimeter, Terahertz Waves* **2013**, *34* (1), 1–27.

(137) Majumdar, A.; Kim, J.; Vuckovic, J.; Wang, F. Graphene for Tunable Nanophotonic Resonators. *IEEE J. Sel. Top. Quantum Electron.* **2014**, *20* (1), 68–71.

(138) Brown, E. R. E. R.; Zhang, W.-D. W.; Viveros, L.; Neff, D.; Green, N. S. N. S.; Norton, M. L. M. L.; Pham, P. H. Q. P. H. Q.; Burke, P. J. P. J. Sensing of DNA by Graphene-on-Silicon FET Structures at DC and 101GHz. *Sens. Bio-Sensing Res.* **2015**, *5* (May), 19–23.

(139) Rahman, M.; Neff, D.; Green, N.; Norton, M. DNA Origami Reorganizes upon Interaction with Graphite: Implications for High-Resolution DNA Directed Protein Patterning. *Nanomaterials* **2016**, *6* (12), 196.

(140) Mudalige, T. K.; Sherman, W. B. Atomic Force Microscopy of Arrays of Asymmetrical DNA Motifs. *Soft Matter* **2012**, *8* (11), 3094.

(141) Lyubchenko, Y. L.; Shlyakhtenko, L. S. Visualization of Supercoiled DNA with Atomic Force Microscopy in Situ. *Proc. Natl. Acad. Sci. U. S. A.* **1997**, *94* (2), 496–501.

(142) Berg, F.; Wilken, J.; Helm, C. a.; Block, S. AFM-Based Quantification of Conformational Changes in DNA Caused by Reactive Oxygen Species. *J. Phys. Chem. B* **2015**, *119* (1), 25–32.

(143) Lyubchenko, Y. L. Preparation of DNA and Nucleoprotein Samples for AFM Imaging. *Micron* **2011**, *42* (2), 196–206.

Appendix A – Recipes and Protocols

CVD Graphene

- Cut out a ~ 6 x 6 cm copper foil (Alfa Aesar 13382)
- Prepare electropolish solution as detailed below
  - *Solution: 60mL H2O: 20 mL H3PO4:20 mL Ethanol: 4 mL IPA: 0.4 g UREA*
- Place the copper foil grains going vertical into the solution parallel to a gold glass slide
- Connect ground to the plate and source to the foil
- Apply 5V for 2 mins
- Remove foil from solution
- Clean with water spray
- Clean gold plate with water (to remove the copper precipitates from the slide)
- Dip in water bath ~5 times then ~5 more times in ethanol
- Blow dry with air
- Set on hot plate for 30 secs on 200℃ (*omit for polycrystalline growth)
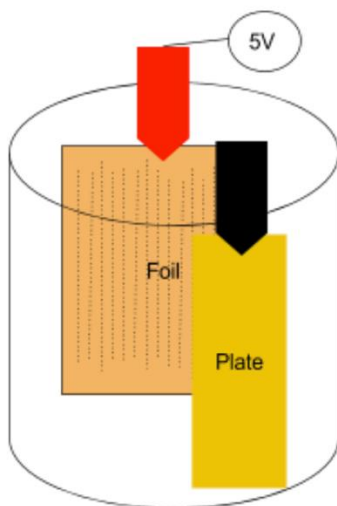
- Fold copper foil into Pia Pocket (*omit for polycrystalline growth)
- Run CVD Recipe
  - *Standard Anneal Recipe* - 20171205_ANNEAL_50PureH2 Annealing_5_Slow_360-385(400)_1hour_5mTorr.rcp
  - *Standard Polycrystalline Film Recipe* - 20170510_GrapheneSeedFill_70-00810-1040-005_1.rcp
  - *Standard Single-Crystal Recipe* - 20160921_O2-6_GrapheneGrain_Ar_01_150-8_2.0_4-1044-005_5.5_45-33perH2_ArHeat.rcp

PMMA Spinning to Cover Graphene for Transfer

- Prepare PMMA
  - *PMMA recipes:*
    - *A3 30 mg /ml PMMA/Anisole => Add 30 mg PMMA (996,000 MW Sigma Aldrich) to 10 mL anisole (long metal syringe) a brown dropper bottle. Stir overnight.*

- - A6 60 mg /ml PMMA/Anisole => Add 60 mg PMMA (996,000 MW Sigma Aldrich) to 10 mL anisole
- Tape sides of foil with graphene facing up on a glass slide
- Using double sided tape, tape glass slide with the graphene-copper foil on spinner with a post-it in the middle for ease of removal *(see image)*
- Use a glass pipet to drop just enough PMMA to cover foil surface area
- Spin PMMA on graphene surface at 10V for 30 secs
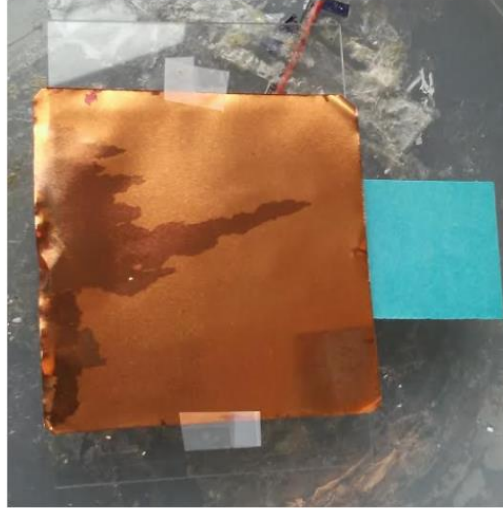
Wet Transfer – Copper Etch
- Allow PMMA to cure overnight
- After curing, flip sample over so that PMMA/graphene/copper is on the bottom.
- Tape corners of copper foil to glass slide for O_2 plasma cleaning (100W for 2 mins)
- Prepare ~5% ammonium per-sulfate solution (usually for 4 dishes, 240ml H_2O: 12g ammonium persulfate).
- Stir until dissolved
- Cut PMMA/graphene/copper to 1.5cmx1.5cm squares
- Place sample with PMMA on top (will usually take around 3 hours to fully etch)
- After etch, transfer floating PMMA/graphene stack into numerous DI water baths.

Wet Transfer – Electro-delamination
- Prepare delamination solution
  - *Solution: NaOH- 0.2M, from 1 N- 90 mL and 360 mL*
- After spinning, bake PMMA at 90℃ for 30 mins
- After curing, flip sample over so that PMMA/graphene/copper is on the bottom.
- Tape corners of copper foil to glass slide for O_2 plasma cleaning (100W for 2 mins)
- Place in oven at 60℃ for over 24 hrs
- After baking at 60℃, cut PMMA/graphene/copper to 2x1.5 cm squares
- Score about 2-3mm on the PMMA side along longer side (so the PMMA/graphene can disconnect from the tweezer)
- Using a flat headed tweezer, place sample with PMMA facing towards the carbon rod
- Fill a small crystallizing dish very close to the top with the NaOH solution

- Connect the ground to the tweezer and the source to the carbon rod *(see image)*
- Make sure the carbon rod is in the solution and the graphene/copper is over the solution
- Apply voltage ranging from 2.5-3 V while watching for bubbles as the graphene/copper foil is lowered into the solution
- The PMMA/graphene should lift off from the copper foil
- After delamination, transfer floating PMMA/graphene stack to DI water bath.
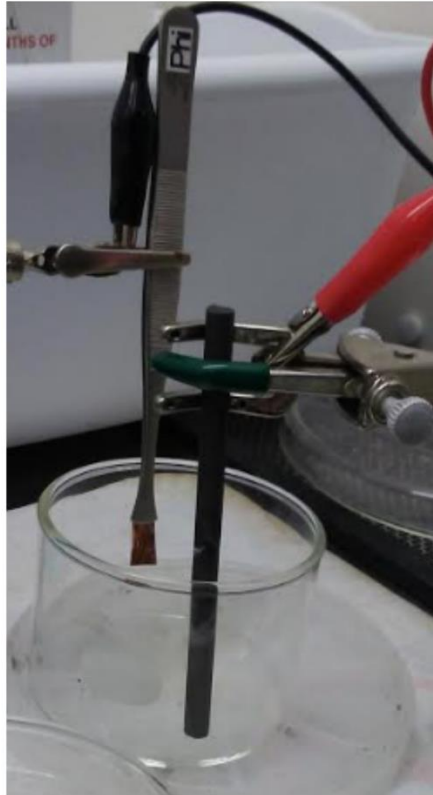
RCA Cleaning
- Removes metal and organic particles from the graphene surface
- RCA$_2$: acidic 20 H$_2$O :1 HCl :1 H$_2$O$_2$ typically 220 mL H$_2$O: 11mL HCl: 11 mL H$_2$O$_2$
- RCA$_1$: basic 20 H$_2$O :1 NH$_4$OH :1 H$_2$O$_2$ typically 220 mL H$_2$O: 11 mL NH$_4$OH: 11 mL H$_2$O$_2$
- Performed in the sequence of RCA$_2$ (30 mins), deionized water bath (short while), RCA$_1$ (30 mins), deionized water bath

Basic Wafer Clean
- After breaking into about 2.5x2.5 cm square, acetone bath (swish bowl to make a small vortex, to remove dust on surface)
- Repeat in IPA bath
- Blow dry with air

Wafer Piranha Clean

- Measure 60 ml sulfuric acid in 100 ml graduated cylinder. Remember acid gloves
- Pour the acid into a large crystallizing dish
- To the acid, slowly add 20 ml H2O2 in a 50 ml graduated cylinder such that for no bubbles form, but steam is let off
- Heat on hot plate at 120ºC for 1 hr (gradual increase in temperature)
- Let cool
- Water bath all samples
- Spray water several times while changing grip on sides to ensure no acid residue
- Blow dry with air
- Up to 12 wafers can be clean at a time

ODTS SAM in Solution
- Clean needle with toluene (the 2 small beakers) about 2-3ml
- Using steel needle syringe, add 10uL OTS (about 32 drops) to 10 mL of toluene (1ml toluene :1uL OTS) Let functionalize for an hour.
- After 1 hour, place wafers into acetone bath and IPA wash
- Dry with N_2
- Up to 8 wafers can be functionalized

Vapor Deposition ODTS
- Measure around 50ul of ODTS into a glass jar with a lid while working in the glove box
- Cover the jar
- Transfer from glove box to a smaller vacuum chamber/desiccator
- Remove the blue stand and place wafer on top
- Take off cap of OTS jar quickly leaving jar inside the chamber
- Quickly place stand with wafer inside desiccator over uncapped OTS jar *(see image)*
- Cap chamber/desiccator
- Evacuate chamber and close vacuum seal. Leave overnight
- Up to 12 wafers can be functionalized